UNIVERSITY OF CALGARY

A Hydrological Characterization of a Proglacial Moraine

by

Gregory Langston

A THESIS

SUBMITTED TO THE FACULTY OF GRADUATE STUDIES

IN PARTIAL FULFILMENT OF THE REQUIREMENTS FOR THE

DEGREE OF MASTER OF SCIENCE

DEPARTMENT OF GEOSCIENCE

CALGARY, ALBERTA

NOVEMBER, 2009

UNIVERSITY OF
CALGARY

Abstract

Groundwater storage and transport processes were investigated in a proglacial moraine in the Canadian Rockies. Geophysical surveys showed that buried-ice and bedrock topography likely control groundwater routing and storage. Hydrograph analysis supported this finding and illustrated how hydrological response differs among moraine regions containing massive ice, degrading permafrost and unfrozen material. Based on these results, a new conceptual model suggests that the dominant groundwater flow system occurs at the moraine-bedrock interface. This flow system was further examined using solute and heat tracer experiments. Groundwater flow was dominated by melt events, while a response threshold existed for rainfall. Rainfall amounts less than the threshold resulted in negligible increases of groundwater flow, whereas amounts above the threshold resulted in large increases. Finally, moraine hydraulic conductivity was estimated using groundwater fluxes calculated from the tracer experiments. These finding make a significant contribution to the understanding of groundwater storage and flow in alpine watersheds.

Acknowledgements

First and foremost I would like to thank my supervisor Dr. Masaki Hayashi. I am grateful for your mentoring, guidance and support. Thank you for the skills and knowledge you have taught me, for trusting me with this project and giving me the freedom to make mistakes. I hope that I have learned from your careful, rigorous approach to science - thank you for making me a better scientist.

I would also like to thank Dr. Laurence Bentley. Although not officially a co-supervisor, he has acted in that role, providing a level guidance and support far beyond that which can be reasonably asked of a committee member. Thank you for the countless hours you have spent with me in the field and interpreting geophysical images. Thanks also for your enthusiasm, which has been both inspirational and motivational.

Funding for this work was provided by: NSERC, the Alberta Ingenuity Fund, and the IP3 Network (CFCAS). Thanks to Parks Canada and Lake O'Hara Lodge for logistical support.

Geophysical equipment is not light, nor did I know anything about it when I started this project. Thus, this thesis was greatly aided by many people who contributed their time and effort helping me collect data. For their help I would like to thank, in no particular order: Ian Anderson, Jane Simmons, Raymond Wong, Chris Donnelly, Josh Ouellet, Simon Martin, Ann Hislop, Nathan Green, Mehran Gharibi, Farzin Malekani, Sarah Forte, Erin Kruschell, and Aurelia Murgia. To those that I have forgotten, my sincere apologies, thanks for your help! Thanks also to Adam Pidlisecky for sharing your forward modelling expertise.

Special thanks are deserved by a core Lake O'Hara research team (again in no particular order). Thanks to Danika Muir for positive encouragement and for making my desk look clean, to Jackie Randell for technical and moral support and for carrying more than your share, to Alastair McClymont for help in the field, with data processing, and for your Matlab wizardry, to Jaime Hood for breaking trail both literally and figuratively and for answering an endless barrage of mountain questions, and to Jim Roy for help in the field, discussions and advice about science and life, and delicious Indian food. Thank you all for your support, advice and friendship.

Thanks also to my parents who introduced me to and encouraged me to explore the wonders of the natural world. Finally, thanks to Anna Hargreaves for all that you do.

Table of Contents

List of Tables

List of Figures and Illustrations

Chapter One: Introduction

1.1 Background

Worldwide, mountain watersheds represent an important and reliable source of fresh water. In fact, between 32 and 60% of global stream discharge is sourced from mountain watersheds [*Bandyopadhyay et al.*, 1997; *Viviroli et al.*, 2007]. With the exception of mountainous regions near the equator, mountain watersheds are dominated by snow and ice-melt processes. Thus, both the quantity and timing of discharge from these watersheds will likely be affected by changes in local glacier storage, precipitation and snow-cover patterns that are predicted by current climate change scenarios [*IPCC*, 2007]. Less snowfall and earlier snow melt will shift peak discharge away from summer and autumn when demands are highest [*Barnett et al.*, 2005; *Milner et al.*, 2009; *Rood et al.*, 2008; *Tague and Grant*, 2009]. Further, it remains unclear whether sufficient water-storage capacity exists in these regions to buffer such changes, or whether much of the winter runoff will be immediately lost to the oceans [*Barnett et al.*, 2005]. The development of accurate, physically-based watershed models will be required to improve our understanding of both mountain watershed hydrology and how predicted climate changes will affect these watersheds, which in turn is critical for effectively managing the water resources within mountain basins. Currently a lack of process understanding and observation networks limit the development of such models [*Bales et al.*, 2006].

Recent studies have shown that, in addition to snow and ice-melt, groundwater can contribute significantly to both streamflow [*Campbell et al.*, 1995; *Clow et al.*, 2003; *Liu et al.*, 2004] and lake water balance [*Hood et al.*, 2006; *Roy and Hayashi*, 2008] in alpine areas. Groundwater processes also play an important role in controlling both the

timing of watershed discharge and the magnitude of summer streamflow loss associated with diminishing snowpacks [*Tague and Grant*, 2009]. Furthermore, groundwater-stream interactions influence both the hydrochemical and thermal regimes of alpine streams, which in turn, have important ecological implications for benthic and stream organisms [*Bales et al.*, 2006; *Brown et al.*, 2006; *Milner et al.*, 2009]. Thus, understanding groundwater processes is critical to the development of physically-based watershed models, and to understanding the magnitude and timing of watershed discharge and the aquatic ecology of alpine environments.

Coarse deposits, such as talus slopes [*Clow et al.*, 2003; *Liu et al.*, 2004], moraines [*Roy and Hayashi*, 2008; 2009] and rock glaciers [*Brenning*, 2005; *Croce and Milana*, 2002] have been shown to play an important role in both storing and transmitting groundwater. However the hydrological processes occurring within these features remain poorly understood, making them difficult to incorporate into watershed models. Consequently, detailed studies of the hydrological processes within these features are essential to improving our understanding of alpine hydrology.

1.2 Objectives

Although moraines are ubiquitous to the glaciated watersheds of the Canadian Rockies, the hydrological processes occurring within these moraines have yet to be rigorously examined. This knowledge gap motivated this thesis, which aimed to improve the current understanding of alpine hydrology by characterizing and parameterizing the hydrological processes occurring within a proglacial moraine. Specifically, the two primary objectives of this thesis were: 1) to develop a physically-based conceptual model

of groundwater flow and storage for the Opabin moraine, a partially ice-cored, proglacial moraine in the Canadian Rocky Mountains, and 2) to characterize groundwater flow through this moraine, by determining the hydraulic conductivity of the moraine's primary groundwater flow path.

1.3 Thesis Organization

This thesis consists of three chapters in addition to this introduction (Chapter 1). Chapters 2 and 3 are written in the format of scientific journal papers, and characterize the hydrology of a proglacial moraine. Detailed introductions, specific to the content of the individual papers, are included at the beginning of each chapter. Chapter 4 provides a discussion and synthesis of the findings of Chapters 2 and 3. A brief description of each chapter is provided below.

In Chapter 2, I present data from extensive geophysical surveys using multiple geophysical methods and simple hydrograph analyses, to determine the possible controls on groundwater routing and storage within the Opabin moraine. Multiple geophysical surveys were used to characterize the internal structure of the moraine and provide some indication of the spatial distribution of structures such as buried-ice and permafrost. Measurements of water-level response at different locations on the moraine are then compared to show how the presence or absence of these structures controls local hydrographic response. Finally, based on the interpretation of the geophysical and hydrological data, I present a conceptual model of groundwater flow, infiltration, and storage within the moraine. Two appendices (A & B) provide supporting analyses for Chapter 2, while a third appendix (C) provides a preliminary estimate of the volume of

buried ice and its hydrological significance. The three appendices are included at the end of the thesis.

In Chapter 3, I characterized groundwater flow through the moraine by examining the groundwater – surface water interactions of a tarn located on the moraine. Two independent experiments were performed to determine the complete water balance for the tarn. The first experiment was a full-tarn chloride dilution experiment. Chloride concentration in the tarn was increased by a one-time addition of sodium chloride. The groundwater components of the tarn water balance were then calculated from the rate of chloride-concentration decay. The second experiment involved detailed energy-balance measurements for the tarn, which allowed groundwater components of the water balance to be calculated from the advection term of the energy balance equation. Hydraulic conductivity for the moraine's primary groundwater flow path was then estimated using a numerical simulation of the tarn to determine an optimal value of hydraulic conductivity, such that the modelled groundwater flows into and out of the tarn approximated the values calculated from mass and energy balance experiments.

Finally, in Chapter 4, I summarize and synthesize the findings and conclusions of Chapters 2 and 3 in the context of future alpine hydrology studies. Specifically, I discuss implications of this work to future efforts in modelling alpine watershed hydrology. I also discuss the implications the geophysical results for the current understanding of ice-cored moraine geomorphology, and highlight the need for a better understanding of what controls buried ice and permafrost distribution within moraines. This discussion is contextualized by the need to characterize these features, and the extent of ice-core and

permafrost within them, if they are to be included explicitly in future physically-based hydrological models.

Chapter Two: A Hydro-geophysical Study of an Alpine Proglacial Moraine

2.1 Introduction

Mountain watersheds have been referred to as the world's water towers [*Viviroli et al.*, 2007], contributing 32 to 60% of global stream discharge [*Bandyopadhyay et al.*, 1997; *Meybeck et al.*, 2001] and up to 90% of stream discharge for some arid regions [*Viviroli et al.*, 2007]. With the exception of some equatorial ranges, stream discharge from mountain watersheds is largely dominated by snow and ice-melt. One recent estimate suggests that roughly one sixth of the world's population relies on glacial and seasonal-snowpack melt to meet its water demands [*Barnett et al.*, 2005]. This is the case for much of western Canada, where alpine watersheds are the headwaters of many major river systems. Consequently, the hydrological significance of mountain watersheds has received increasing attention as their role in providing a reliable supply of fresh water has become increasingly apparent [*Viviroli et al.*, 2003].

The hydrological response of snow- and ice-melt dominated watersheds is predicted to change significantly with anticipated climate warming. Rising global temperatures will likely shift the timing of peak water-flow periods to earlier in the season, away from the summer and fall periods of peak demand [*Barnett et al.*, 2005; *IPCC*, 2007; *Rood et al.*, 2008]. Accurately predicting the effects of climate change on water resources is critical for developing informed water and ecosystem management strategies, but will require physically-based hydrological models to quantify how mountain watersheds will respond to a changing climate. To date, the development of such models for snow- and ice-melt dominated environments has been impeded by a lack

of monitoring networks and inadequate understanding of the processes involved [*Bales et al.*, 2006]. This is especially true in alpine watersheds, where groundwater is known to be an important component of the watershed water balance, but the processes controlling groundwater flow and storage remain poorly understood. Since groundwater has been shown to strongly influence both the timing [*Tague and Grant*, 2009] and magnitude of watershed discharge [*Campbell et al.*, 1995; *Clow et al.*, 2003; *Hood et al.*, 2006; *Liu et al.*, 2004; *Roy and Hayashi*, 2008], physically-based watershed models will need to explicitly consider groundwater processes . However, to do this groundwater processes within the diverse landforms that characterize alpine watersheds (e.g. glaciers vs. moraines vs. alpine meadows) must first be understood.

Periglacial and proglacial landforms may play an important role in the hydrology of alpine watersheds. Although the importance of ice glaciers in alpine hydrology is well appreciated [*Hock et al.*, 2008], comparatively little work has been conducted on periglacial landforms and deposits such as rock glaciers, moraines (ice cored and not) and talus slopes. One recent study of rock glaciers in the Alps showed that although melting internal ice contributed little to average yearly watershed discharge, the presence of rock glaciers resulted in strong diurnal fluctuations and sharp flood peaks in the watershed's hydrographic response due to enhanced near-surface runoff [*Krainer and Mostler*, 2002]. Studies of Andean rock glaciers indicate that they store significantly more water than those in the Alps, and that rock glaciers are important water reservoirs especially in times of drought [*Brenning*, 2005; *Croce and Milana*, 2002; *Schrott*, 1996]. Croce and Milana [2002] suggest that as much as 13% of total water discharged from watershed in the Andes can be attributed to rock glaciers.

In addition to rock glaciers, talus slopes and moraines can play important hydrological roles in alpine watersheds. For example, a watershed in the Colorado Rockies received up to 75% of stormflow and winter baseflow from groundwater discharged from talus slopes [*Clow et al.*, 2003]. Similarly, Roy and Hayashi [*Roy and Hayashi*, 2009] show that stream discharge for a watershed in the Canadian Rockies is dominated groundwater discharge from a moraine. For the same moraine, Roy and Hayashi [2008] also showed that changes in water storage of an alpine lake in the Canadian Rockies were primarily controlled by groundwater exchanged between the lake and the moraine. Furthermore, groundwater and storage within both talus slopes and moraines has also been shown to play an important role in the hydrochemistry of alpine streams [*Brown et al.*, 2006; *Campbell et al.*, 1995; *Liu et al.*, 2004].

Although it is clear that proglacial landforms play an important role in storing and transmitting groundwater, their internal hydrologic processes and pathways remain poorly understood. Several hydro-geochemical studies of groundwater discharge from terminal springs of rock glaciers, terminal moraines and talus slopes have suggested multiple source waters and flow paths [*Brown et al.*, 2006; *Johnson*, 1981; *Roy and Hayashi*, 2009; *Tenthorey*, 1992; *Williams et al.*, 2006]. Whereas distinct source waters are commonly inferred by their chemical signature [*Roy and Hayashi*, 2009; *Williams et al.*, 2006], flow paths are categorized by their hydrological response times. For example, Krainer and Mostler [2002] suggest a two-component (quick and base flow) flow system for three rock glaciers in the Alps based on discharge and electrical conductivity measurements. They note that quick flow is more dominant during spring and early summer and attribute this to snow melt. In contrast, base flow is more dominant later in

the season and thought to be the result of internal ice melt [*Krainer and Mostler*, 2002]. Williams et al. [2006] presented a conceptual model based on detailed water chemistry and hydrograph separation analysis of a three-component flow system characterized by snow melt, soil water, and base flow (attributed to internal ice melt) for a rock glacier in Colorado. The relative importance of the components varied throughout the season as both snow and the rock glacier's active layer melted. Similarly Roy and Hayashi [2009] hypothesized a three-component flow system based on the water chemistry of a series of groundwater springs flowing from a moraine terminus in the Canadian Rockies. In this case the components are suggested to be from 1) a groundwater dominated lake abutting the moraine, 2) deep groundwater from melting buried ice, and 3) shallow groundwater, likely resulting from snow-melt or precipitation flowing along shallow impermeable boundaries (buried ice and bedrock). Despite compelling evidence for multiple water sources provided by geochemical studies, the physical structure controlling the flow paths remains poorly understood.

Geophysical surveys represent one possible method to elucidate the physical controls on coarse deposit hydrology. Geophysical studies have been used extensively to examine the structure and extent of mountain permafrost in relation to slope stability [see *Hauck and Kneisel*, 2008]. Although a number of studies of the internal structure of rock glaciers studies suggest a wet debris layer below the permafrost [e.g. *Croce and Milana*, 2002; *Hausmann et al.*, 2007; *Musil et al.*, 2006], geophysical surveys have yet to be specifically targeted at investigating the complex hydrological processes suggested by geochemical studies in these or other periglacial landforms.

Ice-cored proglacial moraines are common periglacial landforms in western Canada, and represent significant geologic features within many alpine watersheds [*Østrem and Arnold*, 1970]. Recent studies in the Opabin watershed of the Lake O'Hara Research Basin (LORB) in British Columbia, Canada, have indicated the importance of a proglacial moraine in storing and transferring groundwater [*Roy and Hayashi*, 2008; 2009]. This moraine is hypothesized to be ice-cored based on its geomorphological characteristics (Osborne pers. com.) and visible ice in some areas. As noted above, water chemistry of a series of groundwater springs flowing from the moraine terminus indicates multiple source waters and flow paths [*Roy and Hayashi*, 2009]. Although ice-cored moraines and rock glaciers share many similarities [*Barsch*, 1971], there are significant differences with respect to the extent and dynamics of ice (i.e. ice-cored moraines are stagnant ice whereas rock glaciers are dynamic; *Østrem*, 1971). These differences may have implications for the hydrological processes within these landforms. For example, frictional and deformational heating within active (dynamic) rock glaciers can result in melt water production [*Jansen and Hergarten*, 2006], which is unlikely in stagnant ice-cored moraines. Thus, differences in dynamics and internal structure make it difficult to interpret the hydrological pathways within ice-cored moraines based on geophysical surveys of rock glaciers. Consequently hydrogeophysical studies of the internal structure of moraines and ice-core moraines are required to examine the physical controls on flow pathways occurring within these features.

This chapter presents the results of a detailed geophysical study over the proglacial moraine in the Opabin watershed. Electrical resistivity imaging (ERI), seismic refraction, ground-penetrating radar (GPR), and bottom temperatures of the winter

snowpack (BTS) are used to investigate hydrologically significant features such as ice-core, degrading permafrost, structure and thickness of moraine material, and bedrock topography. The results of the geophysical surveys are used to generate a conceptual model of water flow and storage consistent with the geochemical results presented by Roy and Hayashi [2009]. Hydrograph data from a number of surface-water features connected to the moraine are used as evidence to support the conceptual model. This report is the first hydrogeophysical study in the Canadian Rockies, and the first of a proglacial moraine.

2.2 Site Description

The Opabin Plateau is a small (~ 5 km^2) alpine sub-watershed of the Lake O'Hara Research Basin located in Yoho National Park, British Columbia, Canada. The Opabin watershed is approximately 2220 m.a.s.l. and is dominated by moraine and talus material (60%), exposed bedrock (25%), and alpine meadow (15%). Bedrock is primarily composed of thickly bedded quartzite and quartzose sandstone, separated by thin layers of siltstone, sandstone and grey shale of the Cambrian Gog Group. Highly fractured bedrock has been observed at some locations close to the moraine, indicating that bedrock underlying the moraine may also be fractured. Carbonate rocks of the Mt. Whyte, Cathedral, Stephen and Eldon Formations are present in the moraine and talus material [*Lickorish and Simony*, 1995; *Price et al.*, 1980]. A small glacier (the Opabin glacier) is located at the southern end of the watershed, separated from the rest of the watershed by the large moraine complex (Figure 2-1).

The moraine complex is the result of multiple glacial advancements, and shows signs of being ice-cored. Geomorphologic indications that the moraine is ice-cored include steep terminal slopes [*Østrem and Arnold*, 1970] and regions of topographic highs and lows that suggest deflation due to ice-core melt. In addition, shallow buried ice is visible at some locations. In some locations an upper moraine, likely dating from the Little Ice Age (~700 years before present (ybp)), can be clearly seen overriding a lower moraine that was likely deposited during the Younger Dryas period (~12 000 ybp) indicating that the moraine complex is the result of multiple glacial advances [see, *Roy and Hayashi*, 2009]. A series of ridges run approximately north to south separating topographic lows. The grain size of the moraine surface material ranges from coarse sands (ca. 0 φ units) to large boulders (ca. -8 φ units).

The moraine represents a hydrologically important landform within the watershed. No surface-water channels exist on the moraine, and the origin of the main outlet stream for the Opabin watershed is a network of springs that discharge year-round from the terminus of the moraine's western portion. Therefore, all snow melt occurring on or south of the moraine and all glacier melt must pass through the moraine to reach the outflow of the watershed. Three surface-water ponds exist on the main part of the moraine, two of which (East Tarn and South Tarn; Figure 2-1) are ephemeral. The eastern terminus of the moraine abuts Opabin Lake, one of two small lakes in the Opabin Watershed. The water level of Opabin Lake is dominated by groundwater flow and is thought to act as a flow-through lake [*Roy and Hayashi*, 2008]. It remains unclear how the surface waters are hydrologically connected, but water-chemistry data suggest that the East Tarn and Opabin Lake share similar source waters and represent a single, distinct

end member for water discharged from the springs at the moraine terminus. The West Tarn has dramatically different water chemistry and does not appear to be an end member of the outlet springs. The remaining two end members are hypothesized to be deep and shallow groundwater flow [*Roy and Hayashi*, 2009].

2.3 Methods

2.3.1 Electrical Resistivity Imaging

Electrical resistivity imaging (ERI) involves injecting a direct current into the subsurface through two electrodes and measuring the resulting induced voltage between two other electrodes. Measurements are made using many different electrode locations and separation distances, and a profile of the subsurface resistivity distribution is then constructed with an inversion program. ERI has proven useful in both hydrology research and in studies of permafrost-related environments, due to the high contrasts in resistivity between saturated and unsaturated regions and the extremely high resistivity of ice (Table 2-1). Although mountainous terrain creates many difficulties in applying ERI (e.g., high contact resistance between the electrodes and the ground, large topographic variations, and extreme resistivity values), ERI has proven effective in delineating areas of mountain permafrost [*Evin et al.*, 1997; *Hauck and Vonder Muhll*, 2003; *Hauck et al.*, 2003; *Hauck and Kneisel*, 2008; *Ikeda*, 2006; *Kneisel*, 2004; 2006; *Maurer and Hauck*, 2007; *Sass*, 2006; *Vonder Muhll et al.*, 2002].

Four ERI lines (Figure 2-1) were completed over the moraine to image features such as high resistivity ice-cores and low resistivity groundwater channels, and to give an overall sense of the internal structure of the moraine. Line 1 was partially located on a

region of known buried ice in order to provide a reference resistivity for buried ice and to test the ability of ERI to distinguish between buried ice and moraine material. The remaining ERI surveys were conducted perpendicular to the hypothesized groundwater flow direction in order to image potential groundwater flow pathways. Surveys were conducted using cables with a total of 48 electrode take-outs and an Iris Syscal Pro system. To obtain relatively long profiles, survey lines were extended by "rolling" two six-electrode cables an appropriate number of times. Electrode spacing was 5 m for ERI line 1, 8 m for ERI lines 2 and 3, and 4 m for ERI line 4. All surveys were conducted using a Wenner array, which maximizes the signal to noise ratio and provides a good compromise between efficiency and vertical resolution [*Hauck and Kneisel*, 2008]. Water-soaked sponges were used to improve the contact resistance between electrodes and the ground surface [*Hauck et al.*, 2003]. For the rare locations where planting electrodes was not possible (e.g. on large boulders), aluminum foil and medical imaging gel (Signa Gel, Parker Laboratories Inc.) were used to create electrical contact. The electrical contact for these electrodes was generally poor.

Each datum point used to generate the apparent resistivity distribution is an average of three repeated measurements. Data with a standard deviation of ≥ 0.3 % were removed from the data set, as were data points that did not vary smoothly within the dataset. Electrode locations were surveyed using either a differential GPS or Total Station. All electrodes were projected to a best-fit straight line so that the data could be used in a 2-D inversion algorithm. Two-dimensional resistivity models were generated using the inversion code RES2DINV [*Loke and Barker*, 1996]. As sharp geologic boundaries were anticipated, data were inverted using a robust data and model inversion

constraint (L1-Norm) and a damping factor of 0.3. Inversion model cell-width was set to half the electrode spacing. Depth of investigation (DOI) tests were conducted for each survey to evaluate the reliability of the inverse model (Appendix A) [*Marescot et al.*, 2003; *Oldenburg and Li*, 1999]. These tests involved performing two inversions of the same data using different values of the initial reference resistivity (starting model). Where the resulting inverse models are similar (residual values < 0.1), the model resistivity values are considered well constrained by the data. Conversely, where the inverse models differ significantly (residuals > 0.1) resistivity values must be interpreted with more caution [*Marescot et al.*, 2003].

2.3.2 Seismic Refraction

Seismic refraction surveys can reduce the non-uniqueness of resistivity interpretations, because they can clearly distinguish between ice and air, which have similar resistivity values [*Hauck and Vonder Muhll*, 2003]. Seismic p-waves travel through the subsurface, and refract or bend as velocity generally increases with depth. The degree to which seismic ray-paths bend depends on the primary-wave (p-wave) velocity through the geologic media. Analysis of the first-arrival times at each receiver enables delineation and characterization of these geologic layers and structures. This method has been successfully applied in many mountain permafrost studies despite complex terrain and difficulties ensuring contact between geophones and the ground [*Hauck and Vonder Muhll*, 2003; *Hauck et al.*, 2004; *Hausmann et al.*, 2007; *Ikeda*, 2006; *Sass*, 2006].

Two seismic refraction surveys were conducted along portions of ERI lines 1 and 2. Data were recorded using a Geometrics 24-channel Geode system. The seismic

source was an 8 kg sledge hammer and high-density plastic strike plate. Multiple blows were summed or stacked until an acceptable signal-to-noise (S/N) ratio was obtained. Geophones were fitted with a plastic plate and coupled to a flat region of the ground surface using a small rock to hold the geophone in place and prevent movement due to wind. Geophones were spaced 2 m apart along the survey line, and shot points were located every 25 m for line 1 and every 10 m for line 2. The longest shot offsets were 50 m for line 1 and 40 m for line 2. Receiver and shot locations were surveyed using either a differential GPS or Total Station, and were projected to a best-fit straight line for analysis.

The software package Reflex-Win (Sandmeier Software) was used to pick the first arrival times from individual shot records. Estimated pick uncertainties varied depending on the S/N ratio of each seismic trace. The highest quality picks were assigned an uncertainty of 4 ms, whereas the poorest quality picks were assigned uncertainties of 12 ms. First arrival times were then inverted to produce refraction tomograms using an inversion code based on a finite difference eikonal solver [*Lanz et al.*, 1998; *Musil et al.*, 2002]. The inversion stopping point was determined using reduced chi-squared values, which compare travel time residuals calculated from the model to the estimated pick uncertainties. Chi-squared values close to 1 represent an appropriate stopping point, whereas values <1 suggest overfitting of the data [e.g. *Clark et al.*, 2008]. Both velocity models converged after four iterations. Plots of first break picks compared with modelled first arrival times and ray path plots were used to check the consistency of the model and the data.

2.3.3 Ground Penetrating Radar

Ground penetrating radar (GPR) is an electromagnetic technique used to map structures in the subsurface based on boundaries between materials with different dielectric properties. GPR has proven valuable in several mountain permafrost studies [*Hausmann et al.*, 2007; *Maurer and Hauck*, 2007; *Sass*, 2006; *Vonder Muhll et al.*, 2001; *Vonder Muhll et al.*, 2002]. GPR data was collected using a Pulse Ekko system (Sensors & Software Inc.). Three 50 MHz GPR profiles were run with 2 m antenna separation and a 0.25 m measurement interval along portions of ERI lines 1, 2, and 3 that showed interesting resistivity structures (e.g. potential permafrost features, massive ice and moraine material transitions etc., Figure 2-1). The result was 2D-sections of the subsurface called radargrams created from detailed records of travel times for reflected radar signals. Low-frequency inductive electromagnetic noise was removed from each data set using a dewow filter [*Reynolds*, 1997]. After correcting first-arrival times to zero offset, each trace was gained by dividing the original trace by a smoothed version of its amplitude envelope [e.g.*Gross et al.*, 2004]. Finally, a bandpass filter was applied to remove the remaining high- and low-frequency noise.

To determine the velocity of the GPR signal through the subsurface, common mid-point surveys (e.g. varying the antenna separation while maintaining a fixed mid-point) were conducted for each 2D profile. Signal velocities were determined based on the time move-out of reflections [e.g. *Yilmaz*, 2001]. The average velocity of the GPR signal through the subsurface was 0.13 +/- 0.02 m/ns. Topographic static corrections to first arrivals were applied to each trace by converting time to distance depth using the average subsurface velocity.

2.3.4 Bottom Temperatures of Winter Snow Cover (BTS)

The temperature at the interface between a sufficiently deep snow pack (>1m) and the ground can be used to establish the presence of permafrost in mountainous environments [*Bonnaventure and Lewkowicz*, 2008; *Hauck et al.*, 2004; *Hoelzle et al.*, 1999; *Ikeda*, 2006; *Lewkowicz and Ednie*, 2004; *Vonder Muhll et al.*, 2002]. Temperatures below -3 ^{o}C generally indicate permafrost, whereas temperatures above -2 ^{o}C suggest permafrost-free areas or areas of deep-seated inactive permafrost [*Hoelzle et al.*, 1999]. Five miniature temperature sensors (Hobo Water Temp Pro v2, by Onset) which were installed in fall 2007 as part of a larger temperature sensor array to delineate regions of buried ice and permafrost within the moraine, coincided with locations along survey lines 1 and 2 (Figure 2-1). Temperatures were recorded every 30 min starting on January 1, 2008 and averaged over the 4-month period between January and April. Average moraine snow depth determined from an April snow survey was 1.79 m (Hood, pers comm.). Average temperatures measured by sensors located along the geophysical survey lines were used as an indication of permafrost presence or absence.

2.3.5 Hydrograph Analysis

Hydrographs from surface water features can provide useful information regarding the hydrological response of flow systems to precipitation and snow and/or glacier melt events and can provide clues about the underlying geology. Water level data for the East Tarn, Opabin Lake, West Tarn, and South Tarn were collected every 10 min using pressure transducers (In Situ mini troll and level troll). The cross-correlation between the

East Tarn and Opabin Lake hydrographs was examined using the software package PAST [Hammer, 2006]. Air temperature and precipitation data were recorded by a thermistor (height ca. 2 m) and tipping bucket rain gauge respectively, located at a meteorological station ca. 500 m northwest of Opabin Lake. Snow cover on the moraine remains until late June and early July, whereas snow cover on the glacier and the high peaks of the cirque forming the south-east boundary of the moraine remains until August. Graphical comparison of the hydrographs with the meteorological data was used to asses the response of each water body to melt and precipitation events. Periodic oscillations in the hydrograph data were analyzed using the fast Fourier transform (FFT) algorithm included in the Matlab (The Mathworks Inc.) software package. The 24-h period of oscillation is interpreted to be the result of diurnal fluctuations in water level due to snow, glacier and/or buried ice melt. The phase angle from the FFT analysis corresponding to the 24 h period of oscillation is used to determine the response time for each system (water body) to the diurnal signal. The hydrographic response of the surface water features is used to interpret the influence of local geology (e.g. massive ice, permafrost, no ice) as interpreted from the geophysical data, on both regional and local flow systems.

2.4 Results and Interpretation

2.4.1 Electrical Resistivity Imaging

When plotted together, all four of the ERI surveys showed a similar and consistent internal structure (Figure 2-2). A relatively low-resistivity layer (ca. 2000 Ωm) exists ca. 0 - 5 m below the ground surface (b.g.s.). A second layer occurs at ca. 5 - 17 m b.g.s. with resistivities of 8000 to 40000 Ω-m. Finally, a third layer with resistivites of <5000

Ω-m begins around 17 m.b.g.s. The thickness of the third layer is undeterminable due to poor resolution at this depth of the model. Highly resistive regions (>1 million Ωm) at the southern portion of ERI 1 and western end of ERI 2 are interpreted to be buried massive ice (MI in Figures 2-2, see Table 2-1). Massive ice has also been observed at the surface of the debris-covered ridge extending north from the Opabin glacier (ERI 1, Figure 2-1), providing confidence in this interpretation.

The sharp contrast in resistivity between regions of massive ice (MI in Figure 2-3, >1 million Ωm) and no ice (< 20 000 Ωm, see Table 2-1) allows the extent of ice-core to be clearly delineated in ERI 1 (Figure 2-3). The region of low-resistivity at shallow depths in the northern section of the image is interpreted as wet, but unsaturated sediments, which are termed wet moraine material (WMM). Structures beneath the surface of the massive ice cannot be imaged because high ice-resistivity prevents current from flowing to any significant depth. Similarly, massive ice may limit current flow to deeper regions immediately north of the ridge. The DOI test for ERI line 1 indicated that resistivity values immediately north of the ice ridge at depths below ca. 8 m are not well constrained by the data (residuals > 0.1; Appendix A). Consequently, only the large trends in resistivity (e.g. transitions from high to low values) that are consistent with the other ERI surveys are interpreted.

Aside from the western end of ERI line 2, where high-resistivity massive ice also masked deeper structures, most of the inverted model reveals important information about the potential mechanisms of groundwater flow and storage (Figure 2-4). Regions of the model between ca. 5 and 15 m.b.g.s and with resistivity values between 20 000 and 100 000 Ωm are interpreted to be discontinuous bodies of permafrost (see Table 2-1).

Lower resistivity values (~ 2000 to 4000 Ωm) in the top 5 m of the image are interpreted as wet moraine material and/or moraine material with finer sediment within the pore spaces which would result in less void space and thus lower resistivities (WMM; Figure 2-4). Although it is unclear why fine sediments would accumulate in this top layer they were visually apparent at the surface on some areas of the moraine. It is possible that permafrost acts as a barrier to the transport of fine sediments, restricting them to the pore spaces in the upper layer. A small region of low resistivity (<1000 Ωm, PW in Figure 2-4) is likely a region of perched sediments, either saturated or with a higher water content than the rest of the upper layer. Late-summer snow was observed in this region and likely acted as a source of melt water for these areas. A similar low-resistivity region borders the massive ice. Although melt-water regions might be expected bordering the massive ice, the low-resistivity values in this area are poorly constrained (residuals ≥ 0.2) according to the DOI tests (Appendix A) and may therefore represent an artifact of the inversion process.

ERI line 3 shows many of the same features as ERI line 2 (Figure 2-5). As in ERI line 2, the resistive layer imaged by ERI line 3 (interpreted as permafrost) is located between ca. 5 and 15 m.b.g.s. (PF; Figure 2-5). Resistivity values in this region appear higher in this line than in ERI line 2, and are interpreted to be more substantial permafrost. The region of highest resistivity (PF; interpreted as the region of most substantial permafrost) occurs below an area of low resistivity (PW) in Figure 2-5, suggesting that permafrost is supporting perched groundwater at this location. In this case, the permafrost may be acting as a barrier to water flow and thus play a role in groundwater routing. Immediately east of the permafrost (x ≈ 360 to 390 m), resistivity

values decrease to <8000 Ωm, indicating a region without permafrost. Note that this is consistent with ERI line 1, which intersects ERI line 3 at this location. Further east on ERI line 3 (x ≈ 390 to 540 m) resistivity increases to between 12000 and 18000 Ωm. The composition of this region remains ambiguous as the resistivity values are generally lower than those interpreted to be permafrost. However, the physical proximity to identified permafrost and the relatively high resistivity values suggests that this region could contain degrading (melting) interstitial ice. The low-resistivity region occurring in the depression at x ≈ 550 m may indicate preferential ground water flow pathways, or regions of preferential infiltration (INF; Figure 2-5). Note that in both ERI lines 2 and 3 the resistive layer interpreted as permafrost becomes more continuous towards the western edge of the moraine (Figures 2-4 and 2-5).

ERI line 4 was conducted up-slope of the East Tarn which is a surface expression of the local water table (Figures 2-1 and 2-2). Thus, due to the proximity of this survey to the East Tarn, the top of the low-resistivity region seen in the model at ca. 10-15 m.b.g.s. is believed to represent the groundwater table in this region of the moraine (GW in Figure 2-6). Resistivity values in the region between ca. 5 and 10 m.b.g.s. are mostly < 20 000 Ωm, suggesting that there is no permafrost in this region.

The consistency among the resistivity images is especially evident at the line intersections (Figure 2-2) and provides confidence in the accuracy of the individual lines. The DOI tests indicate that for all ERI lines the low-resistivity values in the deepest part of the models are not well constrained (residual values > 0.1; Appendix A). Although these resistivity values are poorly constrained, they are consistently lower than those of the overlaying layer, regardless of the starting model used in the DOI tests. This suggests

that the ubiquitous resistivity boundary, marked by the transition from high to lower resistivity in the lower part of the models, represents a real transition, not an inversion artifact.

2.4.2 Seismic Refraction

The inverted p-wave tomograms show variable velocities, which are used to interpret different geological structure. High p-wave velocities are expected for buried ice, permafrost and bedrock. Conversely, p-wave velocities through unconsolidated moraine material are expected to be relatively low (Table 2-1). A representative shot gather showing the individual traces, first break picks, and the corresponding modelled first arrivals is shown in Figure 2-7. The inverted tomogram for seismic refraction line 1 shows a relatively high velocity in the ridge extending north from the Opabin glacier (MI; Figure 2-8). P-wave velocities in this region range from 2500 to 4000 m/s, which is consistent with published values for massive ice [*Hauck and Kneisel*, 2008]. P-wave velocities appear to decrease from high values (ca. 3500 m/s) to lower values (ca. 2000 to 2500 m/s) at a near constant elevation of 2275 m.a.s.l. This transition is interpreted to be the base of the massive ice; however limited ray coverage in this region of the model reduces confidence in the actual location of the boundary (Figure 2-8B).

To the north of the high-velocity ridge, a fast layer with p-wave velocities between 3500 and 5000 m/s starts at ca. 2260 m.a.s.l. (~ 18 m.b.g.s.; Figures 2-8). Resistivity data from this region indicate that this lower layer has a relatively low resistivity (Figure 2-3). Consequently, the lower layer does not appear to be massive ice and, as will be discussed later, this transition is interpreted to be the top of bedrock

(represented by the dashed line, Figure 2-8A). A topographic depression in the top of the interpreted bedrock layer, just north of where the ice-cored ridge joins the moraine, may be the result of glacial erosion, but the plotted ray-paths suggests that this area is not well constrained (Figure 2-8A). P-wave velocities above the bedrock layer range from ca. 500 to 1500 m/s, consistent with published values for moraine debris [*Hauck and Kneisel*, 2008]. This upper layer is interpreted to be unconsolidated moraine material and ranges in thickness from ca. 30 to 16 m and decreases in thickness to the north (MM; Figure 2-8). With the exception of the ice-cored ridge, p-wave velocities within the moraine are too low to indicate permafrost above the interpreted bedrock layer. Note that the lack of permafrost immediately north of the ridge is consistent with the interpretation of ERI line 1 and ERI line 3.

Seismic line 2 also shows high p-wave velocities (3500 to > 4000 m/s) at approximately18 m.b.g.s., which are again interpreted as the top of bedrock (Figure 2-9A). A depression in the top of this layer at the western end of the image may represent a depression in the bedrock or fractured and/or more weathered bedrock which would also show lower p-wave velocities (BRD; Figure 2-9A). This region of the model is well sampled by the ray-path coverage, suggesting that the feature is real. As with seismic line 1, p-wave velocities above the bedrock layer provide no indication of permafrost (MM; Figure 2-9A and B). This is in contrast to ERI line 2, which shows resistivities in the range possible for permafrost (Figure 2-4).

Figure 2-10 shows a 3-D perspective of the seismic inversion tomograms for lines 1 and 2. Where the profiles intersect, the interpreted depth to bedrock occurs at a consistent depth. The matching structure at the intersections demonstrates the

consistency between the profiles and provides confidence in the interpretation of the material boundaries.

2.4.3 Ground Penetrating Radar

GPR line 1 shows a strong reflection from beneath the ridge extending north from the Opabin Glacier (BMI; Figure 2-11). Superimposing ERI line 1 onto this GPR profile shows that this reflection is either the bottom of the massive ice or a basal layer within the ice representing the boundary between two distinct glacier advances. The corresponding overlay of seismic line 1 on GPR line 1 shows that the reflection interpreted as the bottom of the ice is ca. 10 m above the decrease in the p-wave velocity also interpreted as the bottom of the ice (Figure 12-2). Plotted ray-paths shown in Figure 2-9B indicate that the p-wave velocity transition interpreted as the bottom of the ice is poorly constrained. Thus, the GPR reflection is interpreted to be the bottom of the ice and suggest that the discrepancy between the GPR and seismic images results from model smoothing in the seismic inversion algorithm (Figure 2-12). A second reflection at a depth of ca.18 m.b.g.s., between x = 280 and x = 300 m, appears to correspond to the top of the bedrock interpreted from the seismic refraction tomogram (BR; Figure 2-12).

GPR line 2 also shows a reflection at ca. 18 m.b.g.s. When overlain onto the ERI line 2, this reflection coincides with the lower boundary of the resistive layer (BR in Figure 2-13). As with GPR line 1, this reflection is interpreted to be the top of the bedrock layer. Although the resistivity image is poorly resolved at this depth, both the base of the high-resistivity layer and the GPR reflection coincide with the base of the

low-velocity moraine material interpreted from the corresponding seismic velocity tomogram (BR in Figures 2-13 and 2-14).

GPR line 3 shows more structure in the subsurface than the other GPR lines. As with GPR lines 1 and 2, a reflection interpreted as bedrock occurs at ca. 18 m.b.g.s, which coincides with the lower boundary of the high resistivity layer from ERI line 3 (BR in Figure 2-15). Another reflection can be seen at the top of the image, which dips from near the surface to a depth of ca. 4 m.b.g.s. at ca. x = 340 m (TPF in Figure 2-15). This reflection coincides with the top of the high resistivity layer in ERI line 3, and is interpreted to be the top of a degrading permafrost layer. The maximum depth of this reflection corresponds to a low-resistivity (< 500 Ωm) area that is interpreted as perched water. An attenuated region of the GPR profile provides further evidence for the presence of shallow water (AT in Figure 2-15), which may be actively melting the permafrost layer below. At the eastern end of the image (x ≈ 525 m) the upper reflection appears to split in two: one reflector dips to ca. 3 m depth and the other dips towards the bedrock reflection. The first shallow dip coincides with a small low-resistivity region interpreted to be saturated or partially-saturated sediments (WMM in Figure 2-15), thus the reflection may represent the bottom of the saturated sediments. However, attenuation of the GPR signal is not as strong as it was below the low-resistivity region to the west, indicating that this area may have lower water content than the region interpreted as perched saturated sediments to the west. The reflection that dips towards the bedrock reflector is interpreted as the pinching-out of the structure causing the relatively high resistivity values (x = 490 to 525 m). Although resistivity values in this region are low for permafrost, the GPR reflection outlines a continuous structure suggesting that this region

may be composed of degrading permafrost. The region where the permafrost pinches out (INF in Figure 2-15) may represent an area of preferential infiltration. Furthermore the character of the bedrock reflection changes from variable and undulating to flat with a constant elevation of approximately 2268 m.a.s.l. between x ≈ 510 and 550 m. This change corresponds with a region of low resistivity and is therefore interpreted to represent the water table (WT in Figure 2-15).

2.4.4 Bottom Temperatures of Winter Snow Cover (BTS)

The average temperature at the snowpack-moraine interface ranged from -3.8 to -0.5 ^{o}C (Figure 2-16). The temperature at the base of the deep (>1m) snow pack on the ice-cored ridge was -2.9 ^{o}C, thus all temperature readings <-2.9 ^{o}C under deep snowpacks are interpreted to indicate massive ice or permafrost. As the ridge contains massive ice, it is possible that temperatures slightly warmer than -2.9 ^{o}C may represent permafrost at greater depths. Based on the interpretations of the resistivity and seismic data, the low-temperature areas are consistent with regions of massive ice. Similarly, temperatures at locations along seismic line 2 and the corresponding section of ERI line 2 do not support the presence of permafrost as indicated by the seismic data. Temperatures near the western end of the ERI line 2 do suggest the presence of permafrost, and support the hypothesis of degrading permafrost in this region. However, it remains unclear from the resistivity data alone which regions are underlain by permafrost.

2.4.5 Hydrograph Analysis

Hydrographs recorded for the East Tarn, Opabin Lake, South Tarn and the West Tarn provide useful information regarding the hydrogeology of the moraine. Comparing these hydrographs with air temperature and precipitation from July 5 to September 4 shows dramatic differences in the hydrological response of each water body to late-season snow melt and/or glacier melt and rain events (Figure 2-17). For example, periods of high average daily air temperatures, which are interpreted as periods of high melt, resulted in large water-level increases for the East Tarn and Opabin Lake, whereas water level in the South Tarn declined steadily during the same periods (e.g. July 20 to 23, Figure, 2-17D). Conversely, the South Tarn water level showed large, rapid increases following precipitation events, whereas the water- level response of the East Tarn and Opabin Lake to precipitation events was frequently undetectable or indistinguishable from the melt response preceding these events. Comparatively, the West Tarn hydrograph is characterized by relatively small diurnal fluctuations with no obvious long-term trend in water level. These different responses provide further evidence of multiple flow systems within the moraine and are likely related to the underlying moraine structure. A more detailed examination of the hydrologic response of individual water bodies is presented below.

Water-level responses for the East Tarn and Opabin Lake show a high degree of cross-correlation ($r = 0.89$, where 1 represents a perfect correlation). Roy and Hayashi [2009] showed that Opabin Lake water level was also highly correlated with the discharge from the groundwater spring system at the terminus of the moraine ($r = 0.98$ to 0.96). Discharge response from the springs lagged the Opabin Lake water-level response

by ca. 0.5 to 1 day [*Roy and Hayashi*, 2009]. Chemical and stable isotopic composition of the East Tarn and Opabin Lake are very similar; throughout July-September both water bodies were characterized by moderately high alkalinity (40-50 mg/L expressed as HCO_3^-), low sulphate (<10 mg/L), and $\delta^{18}O$ values remaining in a narrow range between -20 and -19 ‰ (James Roy, unpublished data). Roy and Hayashi [2009] also showed that Opabin Lake represents one end member for water discharged from the springs at the moraine terminus, and suggested that this end member contributes 50 to 90% of the flow out of the springs with the highest contributions being in July and August. Consequently, the East Tarn, Opabin Lake, and the groundwater springs are interpreted to be hydrologically connected. Since the groundwater springs represent the only known source of discharge from the moraine, I suggest that the groundwater flow system connecting the East Tarn, Opabin Lake and the groundwater springs represents the dominant groundwater flow system through the moraine.

A graphical comparison of East Tarn and Opabin Lake water depth and water-level change (Δh) with air temperature and cumulative precipitation from July 16 to 26 is shown in Figure 2-18 as this period clearly show the response of these water bodies to periods of high temperature. Large water-level increases for the East Tarn and Opabin Lake from July 21 to 23 appear to be in response to a period of high air temperature, where air temperature represents the combined effects of net radiation and sensible heat (Figure 2-18). Conversely, a precipitation event (ca. 7 mm) on July 23 had very little effect on water-level response. This indicates that groundwater flow in this region of the moraine was largely sourced from snow and/or ice melt during this period. Peak air temperature occurred at ca. 1600 h, whereas peak water-level change occurred at ca. 0200

h for the East Tarn and ca. 0400 h for Opabin Lake. Thus, there was a time lag of 10 and 12 h for the melt-water pulse to travel to the East Tarn and Opabin Lake respectively, suggesting that melt water is likely sourced from up-gradient of the East Tarn. Geophysical results indicate that the region of moraine surrounding the East Tarn and terminating at Opabin Lake does not contain massive ice or degrading permafrost. Consequently, the lag times between melt events and water-level increases is hypothesized to represent the time required for groundwater to travel from Hungabee Cirque and/or the Opabin Glacier through the unfrozen moraine material that composes the dominant groundwater flow path through the moraine.

The West Tarn hydrograph shows small diurnal fluctuations around a relatively constant water level. Thinly buried massive ice can be visually identified surrounding the tarn. Thus, the West Tarn is hypothesized to be representative of a water body perched on massive ice. A comparison of the West Tarn water depth and water-level change with air temperature and cumulative precipitation for August 3 to 11 is shown in Figure 2-19 as this period clearly shows the West Tarns response to both temperature and precipitation. Note that peaks in water-level change actually precede peak air temperature by ca. 1 h. This is likely due to the delay between peak net radiation and peak air temperature, but may also be the result of shading of the buried ice around the tarn as the sun moves behind the high peaks to the west in the afternoon. The sharp increase and decrease in water-level change due to the beginning and end of rain events occurring on August 9 and 10 indicate that the West Tarn water level responds almost instantaneously to the precipitation events. This suggests that water contributions to the tarn are sourced from the tarn's immediate vicinity (i.e. the tarn has a relatively small

contributing area) and that the storage capacity of the moraine surrounding the tarn is minimal. Since the storage capacity of the tarn's contributing area is minimal, the ratio of rainfall to water-level rise provides a rough approximation of the size of the tarn's contributing area. Thus, for the August 9 and 10 rain events the ratios of rainfall (ca. 14 for August 9 and 18 mm for August 10) to water-level rise (17 cm for August 9 and 25 cm for August 10) suggest that the tarns contributing area is ca. 12.5 and 14 times the tarn surface area. Thus, based on its relatively small contributing area and rapid water-level response, the West Tarn is interpreted to represents a local flow system dominated by shallow groundwater flow over an impermeable boundary.

The South Tarn hydrograph is characterized by steady declines in water level during periods of high temperatures and sharp increases in water level associated with large precipitation events. Examination of the water-level recession curves resulting from the August 9, 22 and 29 peak water levels indicates a change in the rate of water-level decline as water depth reaches a value of ca. 0.55 m (Figure 2-17D). Water level declined at ca. 5 cm d^{-1} when water depth was > 0.55 m, but at only ca. 1 cm d^{-1} when water depth was below the 0.55 m threshold. Roy and Hayashi [2008] estimated August evaporation from nearby Opabin and Hungabee Lakes to be 0.2 cmd^{-1}, while evaporation measured by a floating evaporation pan in the East tarn ranged from 0.02 to 0.4 cm d^{-1} between August 4 and 8 (Chapter 3). Thus, it is unlikely that the observed water-level declines can be explained by evaporation alone. However, the rates of South Tarn water-level decline are considerably lower than those observed for the East Tarn, which sometimes exceeded 20 cm d^{-1}. Thus, the South Tarn water-level response appears intermediate to the groundwater flow system represented by the East Tarn, which shows

large decreases in water level, and a perched water body such as the West Tarn, which shows only small water level fluctuations.

The change in the rate of water-level decline may be indicative of a fill-and-spill flow system. The term "fill-and-spill" is used to describe groundwater flow systems controlled by microtopography in the bedrock surface. As water fills subsurface bedrock depressions, it spills over, connecting with other saturated depressions. This increases the connectivity of saturated sediments, resulting in increased subsurface flow rates [*Spence and Woo*, 2003; *Tromp-van Meerveld and McDonnell*, 2006]. Thus, the change in the rate of water-level decline occurring at the consistent water depth of 0.55 m suggests the presence of an overflow point at this depth. Whereas overflow points have been described in the context of subsurface bedrock ridges, the overflow point for the South Tarn could be controlled by permafrost topography or fractures that allow water to drain more quickly.

Declining South Tarn water levels observed during periods of high temperatures are perplexing given the proximity of the pond to the Opabin Glacier (Figure 2-1). Despite the proximity and lack of obvious physical barrier to glacier-melt runoff, it is clear from the hydrograph that the South Tarn is hydrologically disconnected from the glacier. The geophysical survey results from ca. 125 m north of the pond suggest that this region of the moraine is underlain by degrading permafrost. Thus, one hypothesis to explain the hydrological disconnect between the glacier and the South Tarn is that a permafrost-free region between them, allowing water to infiltrate to a deeper groundwater flow system and thus bypass the tarn.

While the South Tarn showed a counter-intuitive response to periods of high temperature, it also showed an informative response to rain events. The South Tarn water depth and water-level change are compared to air temperature and cumulative precipitation for August 24 to September 4 in Figure 2-20 as this period clearly shows the South Tarn's response to precipitation events. Steady precipitation amounting to ca. 30 mm occurred between August 27 and 30, resulting in a total water-level increase of 25 cm. However, the change in water level was relatively small for the majority of the rain event, and increased sharply only during the last 5 mm of rain (Figure 2-20). This dramatic spike in water level suggests that there is a precipitation threshold, such that precipitation amounts less than the threshold result in relatively small water-level increases, while precipitation amounts above the threshold result in large, instantaneous increases in water level. Although the cause of this particular threshold remains unclear, such thresholds are also indicative of fill-and-spill systems [*Tromp-van Meerveld and McDonnell*, 2006]. Thus, it is likely that the threshold is related to the amount of precipitation required to fill depressions in the subsurface permafrost or bedrock thereby increase the connectivity of saturate sediments surrounding resulting in groundwater flow to the tarn. Note that a similar, less dramatic threshold phenomenon was also observed in the East Tarn and Opabin Lake water-level data for the same period. Interestingly, whereas Roy and Hayashi (2009) show that the threshold rainfall amount required to cause a discharge response from the groundwater springs is 5 mm, the threshold for the South Tarn, East Tarn and Opabin Lake appears closer to 25 mm for the period described above.

A more quantitative analysis of the water-level response to melt events resulting from the diurnal peaks in temperature and net radiation was conducted by applying the fast Fourier transform (FFT) to each hydrograph and to time-series data of temperature and net radiation. For each hydrograph showing a strong diurnal signal (West Tarn and East Tarn), the phase angle corresponding to the 24 h time period was compared to response times of the net radiation and temperature signals in Table 2. The phase angle corresponding with the diurnal signal present in the net radiation and temperature time series indicates peak net radiation occurred at 13.9 h after midnight (13:54), whereas peak temperature occurred 16.7 hours after midnight (16:42). Thus, peak daily temperature lags peak daily net radiation by 2 h 48 min. Therefore, the lag times between water-level increase and air temperature noted above can be increased by ca. 3 h to determine the lag between net radiation and water-level increase.

Based on the FFT analysis, daily peak water level of the West Tarn lagged the net radiation peak by only 30 min, illustrating the rapid response time of the local flow system to melt. Daily peak water levels for the East Tarn and Opabin Lake lag peak net radiation by 19 h 24 min and 22 h 30 min respectively. This confirms the longer response time of these water bodies, suggesting that the melt-water pulse must travel a considerable distance from its source to the water bodies. The time lag between peak water level for the South Tarn and peak temperature and net radiation could not be determined using the FFT analysis due to the lack of a strong diurnal signal in the water level data.

Contributing areas for the East Tarn, South Tarn and West Tarn were visually estimated from a high resolution digital elevation model, using 2 m elevation contours.

These estimates indicate that the contributing area for the East tarn is likely much larger than that of the South and West Tarns (Figure 2-21). The differences in contributing areas provides supporting evidence that longer flow paths exist for precipitation and melt water contributions to the East Tarn than for either the South Tarn or the East Tarn. Note that while the hydrograph clearly shows that the South Tarn is unaffected by glacier melt, elevation contours suggest that a portion of the glacier should contribute melt-water to the South Tarn (Figure 2-21). Also note that, whereas elevation indicates that melt-water and precipitation from a portion of the north-east facing cliffs should contribute to the West Tarn, this results in a contributing area much larger than expected based on the rapid water level response, and the ratio of rainfall to water level rise. One hypothesis to explain this discrepancy is that melt-water and precipitation preferentially infiltrates at the buried ice-talus boundary, thus bypassing the tarn. The disconnect between the South Tarn and the glacier and the discrepancy between the estimates of contributing area for West Tarn illustrate the complexity of the different flow systems related to permafrost and buried ice.

2.5 Synthesis and Hydrological Interpretation

A conceptual model of water flow through the moraine based on the geophysical and hydrographic results is presented in Figure 2-22. This model attempts to incorporate the hydrologically significant structures and processes interpreted from the geophysical, hydrologic, geomorphologic and visual evidence collected. The moraine contains areas of massive ice (MI in Figures 2-2, 2-8 and 2-16), degrading permafrost (PF in Figures 2-4, 2-5, 2-15 and 2-16), and large regions of no permafrost (MM in Figures 2-8, 2-9, 2-15

and 2-16). As indicated by the conceptual model, it is likely that massive ice plays a significant role in routing snowmelt and rain water by acting as an impermeable layer, causing shallow, relatively fast groundwater flow (e.g. hydrograph response of West Tarn). Massive ice may also direct deeper groundwater flow by acting as a confining layer in some regions (not depicted in the model). Massive ice and permafrost in the ridges and uplands of the moraine likely focus infiltrating water and shallow groundwater flow from topographic highs into depressions. If massive ice or permafrost exists in these depressions, water will accumulate, resulting in saturating the sediments and or surface water features (West Tarn, and PW in Figures 2-4, 2-5 and 2-16). If these ponds and sediments overlay more permeable degrading permafrost, they likely drain at a relatively slow rate (e.g. South Tarn). However, if the ponds and saturated sediments are underlain by massive ice these feature likely remain perched throughout the season (e.g. West Tarn). Perched water may represent a significant source of heat advection, causing melting of the ice/permafrost below it [*Driscoll*, 1980]. This could create regions of focused infiltration to the deeper groundwater flow system below the ice (INF in Figures 2-5, 2-15 and 2-17). In regions where massive ice is adjacent to surface-water streams or ponds (e.g. the tarn in Figures 2-22), runoff from the massive ice may result in a fast response in surface water level (as seen in the West Tarn hydrograph). Deeper groundwater flow that encounters massive ice will be forced over, under or around the ice.

This study illustrates the importance of using multiple geophysical survey methods to increase confidence in the location and interpretation of structural boundaries. Temperatures at the moraine-snowpack interface and seismic data suggest that large areas

in the central moraine region do not contain massive ice or permafrost (Figure 2-16; MM in Figure 2-22). However, parts of the ERI images from the same area indicate a semi-continuous layer with relatively high resistivity values of 20 000 Ωm. Therefore, resistivity values of ≤ 20 000 Ωm cannot be interpreted as permafrost without further supporting evidence. While, the internal structure of these resistive regions remains unclear, one hypothesis is that some form of degrading permafrost does exist in this region, but that it has degraded sufficiently that it no longer exhibits the velocity and temperature signature of more competent permafrost.

Several studies of rock glacier morphology and hydrology have suggested a layer of sediments between the ice and the bedrock [*Hausmann et al.*, 2007; *Krainer and Mostler*, 2002; *Williams et al.*, 2006]. Whereas bedrock resistivity is expected to be ca. 40 000 Ωm based on measurements elsewhere in the watershed, the resistivity data indicate a low-resistivity layer of ca. 4 000 Ωm, coincident with regions of bedrock interpreted from the seismic data (GW in Figure 2-6; BR in Figures 2-8A, 2-9B, 2-12, 2-13, 2-14, 2-15 and 2-17). Consequently a low-resistivity layer of saturated sediments and or saturated fractured bedrock is hypothesized to mask the high resistivity of the underlying competent bedrock. To investigate this possibility I conducted tests using a forward modelling resistivity algorithm [open source code FW_2_5D; *Pidlisecky and Knight*, 2008]. Tests results that support this hypothesis are presented in Appendix B. This hypothesis is also supported by previous modelling which has shown that a thin saturated layer overlying highly resistive permafrost will mask the resistivity of the permafrost layer [*Hilbich et al.*, 2009].

The saturated layer overlaying the competent bedrock likely represents the deep groundwater flow system hypothesized by Roy and Hayashi [2009] that accounts for a significant component of groundwater flow. Because of the longer flow paths within the deep saturated layer, surface water-level response to this deep groundwater flow system is likely slower than the response to shallow groundwater flow over impermeable boundaries (e.g. massive ice and permafrost). Longer response times for East Tarn and Opabin Lake (i.e. deep groundwater flow systems) vs. West tarn (i.e. shallow groundwater flow system) confirm the differing response times of these flow systems. Flow velocities may also differ significantly between the deep groundwater flow path and the near surface flow.

Although the lithology of the saturated layer is a dominant control on the rate of groundwater flow, bedrock topography likely controls the flow paths. The seismic and GPR data indicate an irregular bedrock surface, which may be the result of scouring by glacial advances. Depressions in the bedrock, such as those seen in seismic line 1 (parallel to the region groundwater flow direction), may result in a "fill and spill" type flow system adding complexity to the internal storage mechanisms of the moraine. Evidence for a "fill and spill" system is also noted in the South Tarn, East Tarn and Opabin Lake hydrographs. Bedrock depressions such as those seen in seismic line 2 (BRD, perpendicular to regional flow) suggest channelized flow confined to these depression at sufficiently low water-table elevations and a more integrated flow system when the water table rises above the ridge of bedrock separating the depressions.

2.6 Conclusions

The hydrology of the Opabin moraine is complex, consisting of multiple groundwater sources and flow systems. In this thesis, flow systems were characterized based on the water-level responses of four water bodies connected to the moraine. Flow systems ranged from a localized system dominated by shallow subsurface flow derived from rainfall and snow and ice melt (e.g. West Tarn), to a more integrated flow system dominated by deeper groundwater sourced primarily from snow and ice melt (e.g. East Tarn and Opabin Lake). A threshold response to rainfall events was observed in the hydrograph data of three water bodies (South Tarn, East Tarn and Opabin Lake), suggesting that the flow systems associated with these features can be characterized as "fill and spill' systems.

This complex hydrology is the result of the moraine's internal structure, which contains impermeable (ice and bedrock), semi-permeable (degrading permafrost), and highly permeable (course blocky material) materials. A conceptual model of groundwater flow through the moraine, which was based on hydrograph data and the internal structure of the moraine interpreted from geophysical surveys, suggested that: 1) the majority of groundwater flow through the moraine flows through a saturated layer at the moraine-bedrock interface; 2) massive ice and permafrost likely play key roles in controlling shallow groundwater flow and focusing infiltration to the deeper flow system; and 3) bedrock topography may result in groundwater reservoirs and tipping points creating a "fill and spill" type system. It remains unclear whether the saturated layer the moraine bedrock interface is composed of moraine material, or a highly fractured bedrock layer on

top of more competent bedrock. Further, the thickness of this layer remains poorly constrained and likely fluctuates significantly with changes in the water table.

Finally, permafrost structures within the moraine are likely dynamic, and will probably degrade in the future as the climate warms. The melting of permafrost and ice core within the moraine will not only alter the groundwater flow system and the infiltration of rain and snowmelt, but may also represent a contribution to the water balance that has not been quantified. Consequently, the presence of ice cores presents further challenges to modelling alpine watershed response to climate change, as the relationships between ice-core extent, melt-rate, and climate remain unknown. Future work is required to determine: a) at what rates these ice-cores are melting; b) if melt from ice-core is a significant component of the water balance; and c) how common these processes are, both in the Rockies, and globally.

Material	Resistivity (Ωm)	P-wave velocity (m/s)
Ice-core	> 100 000	2500 to 4500
Degrading Permafrost	20 000 to 200 000	1200 to 2500
Unfrozen Moraine Material	5000 to 50 000	400 to 1200
Water-saturated Moraine Material	< 6000	???
Bedrock	20 000 to 50 000	3000 to 6000

Table 2-1. Expected values for the resistivity and p-wave velocity of different moraine materials (from Hauck and Kneisel, 2008).

	Amplitude	Phase Angle	Phase Lag (h)	Peak Time
East Tarn	0.0104	2.436	9.3	9:18
Opabin Lake	0.00130	3.029	---	---
West Tarn	0.00160	-2.504	14.4	14:26
South Tarn	0.00262	-0.0406	---	---
Air Temperature	1.143	-1.916	16.7	16:42
Net Radiation	121.410	-2.646	13.9	13:54

Table 2-2. Amplitude and phase angle of the diurnal signal are calculated from the fast Fourier transform. Response times calculated from the phase angle are not presented for Opabin Lake and the South Tarn due to their lack of a strong diurnal signal (determined from power spectrum plots).

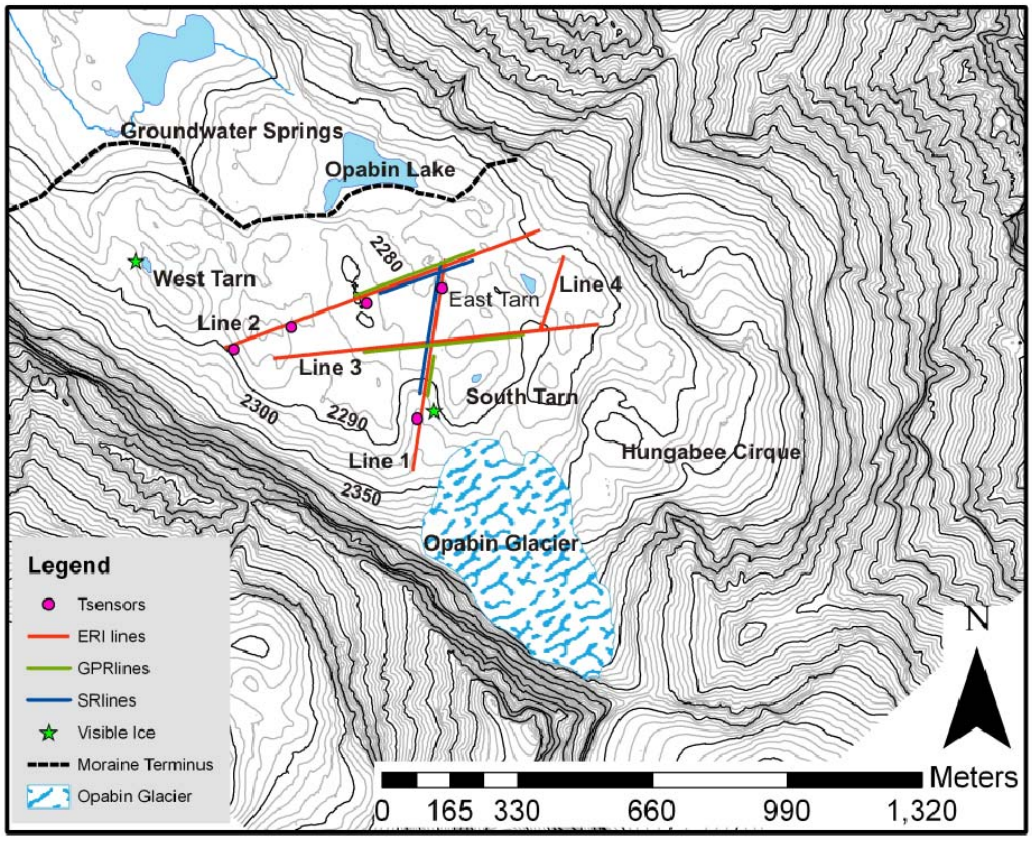

Figure 2-1. A site map of the Opabin Moraine. The thick dashed black line delineates the moraine terminus. Significant water bodies are labeled and geophysical surveys were conducted as shown. The locations where thinly-buried ice is visible and the positions of temperatures sensors used to measure temperature at the snow-moraine interface are also shown.

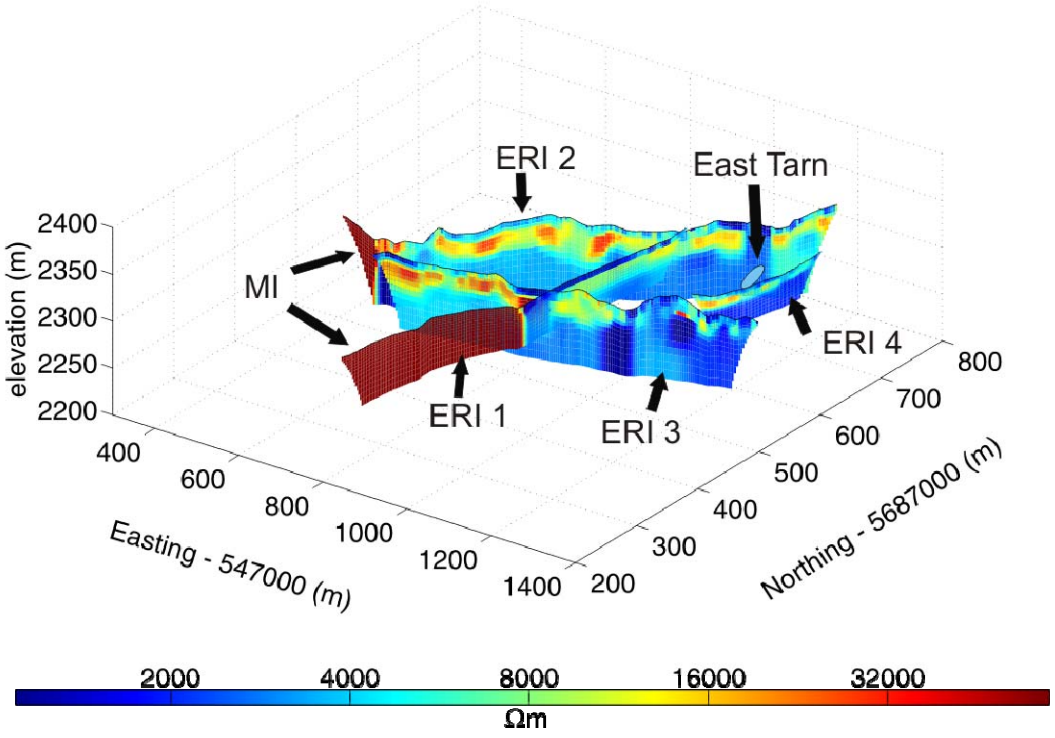

Figure 2-2. A 3D presentation of all resistivity tomograms. Consistency in the location and value of boundaries provides confidence in the results of individual surveys. Note the general pattern of relatively low resistivity in the top 5 m of the moraine, higher resistivity between ~ 5 and 15 m and lower resistivity below 15 m depth.

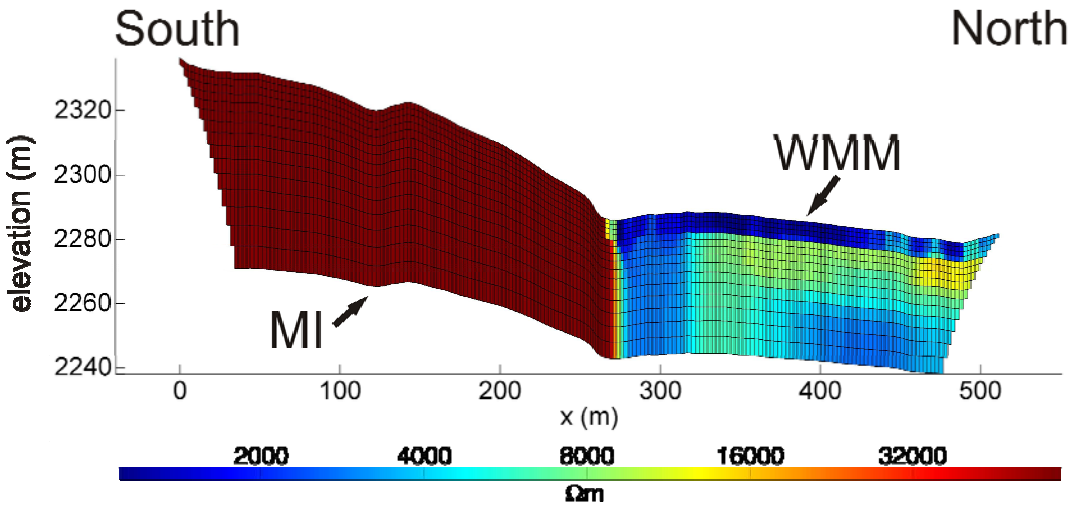

Figure 2-3. Resistivity tomogram for ERI line 1. Massive ice (MI) is clearly delineated by the high resistivity on the left-hand side of the image. The low resistivity in the upper 5 m of the moraine in the right-hand side of the images is interpreted to be wet moraine material (WMM).

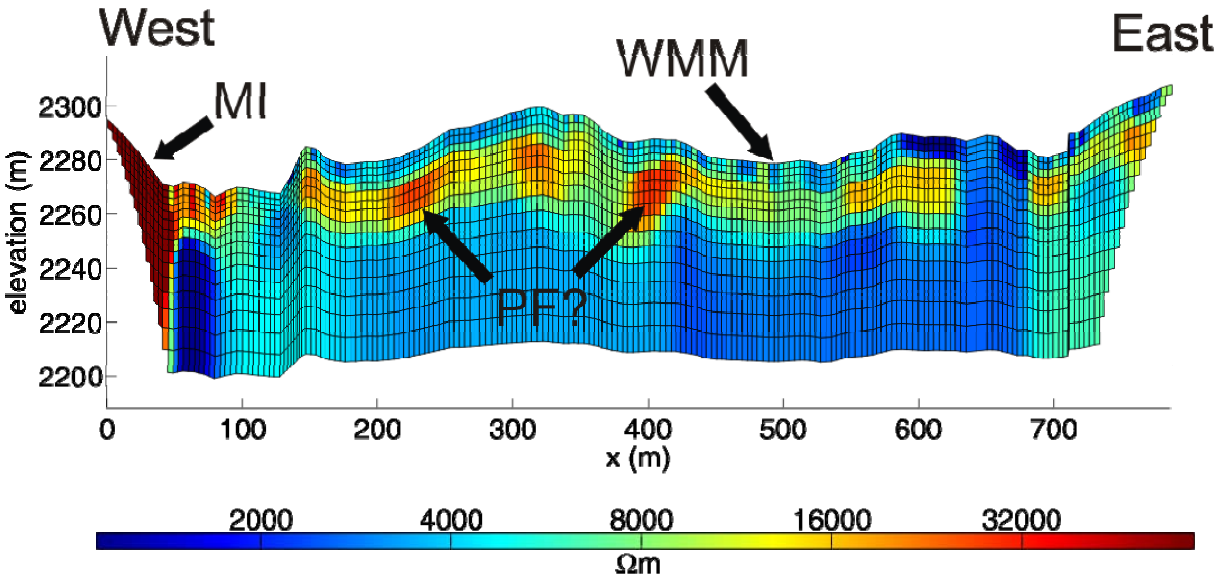

Figure 2-4. Resistivity tomogram for ERI line 2. Evidence of wet moraine material (WMM) is seen in the top 5 m of the moraine. Massive ice (MI) is also clearly seen in the left-hand (west) of the image. Resistivity above 20 000 Ωm may indicate degrading permafrost (PF).

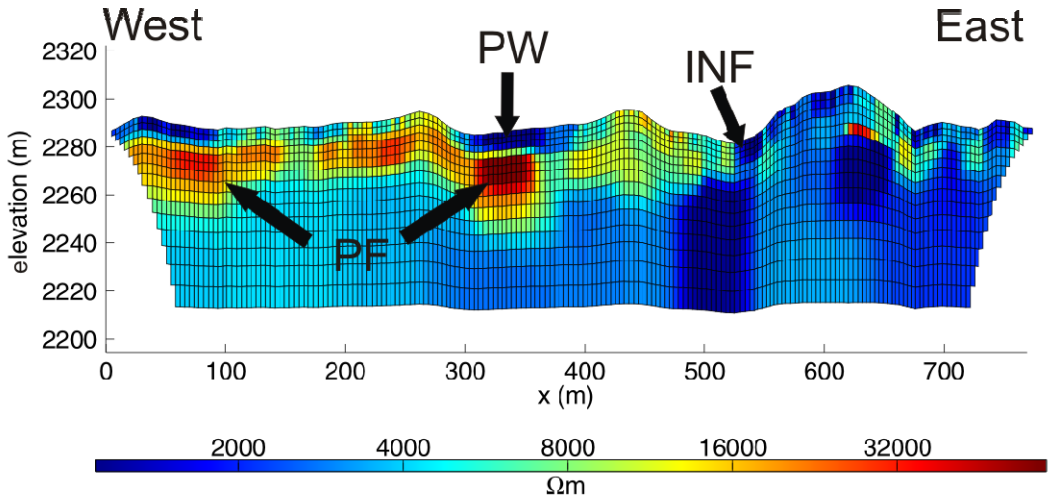

Figure 2-5. Resistivity tomogram for ERI line 3. The high resistivity below the relatively conductive region near the middle of the image is interpreted as saturated sediments (PW) perched on a permafrost layer (PF). Another conductive region appears to the east of the resistive layer. This feature occurs at the base of a depression and is interpreted to represent depression focused infiltration (INF).

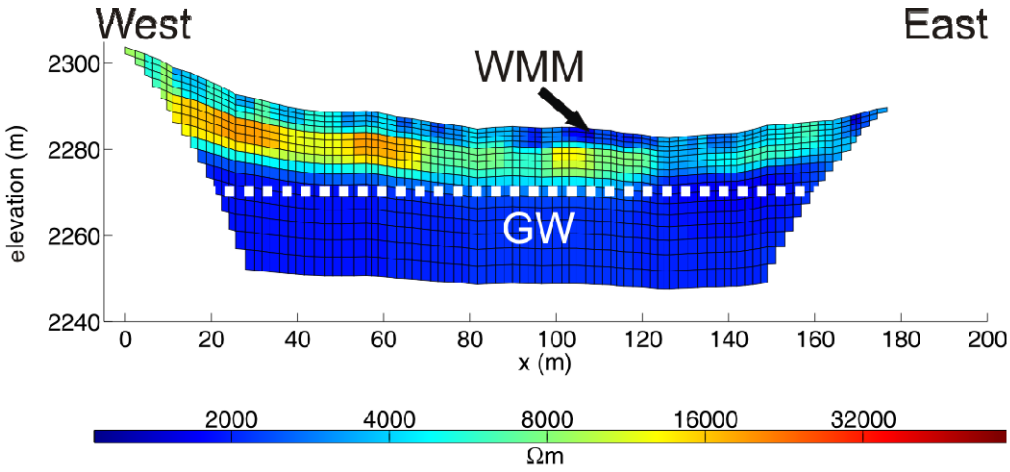

Figure 2-6. Resistivity tomogram for ERI line 4. The upper boundary of the low resistivity in the bottom of the image (dashed white line) is interpreted to represent the top of the water table (GW).

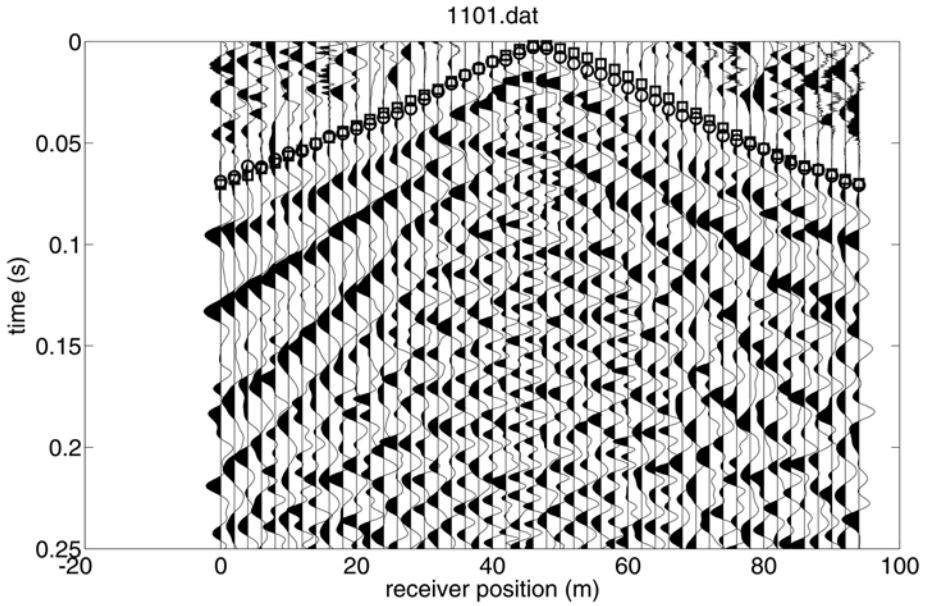

Figure 2-7. A representative shot gather. Plotted circles represent the first break picks, while plotted squares represent the first arrivals modelled, by the inversion algorithm.

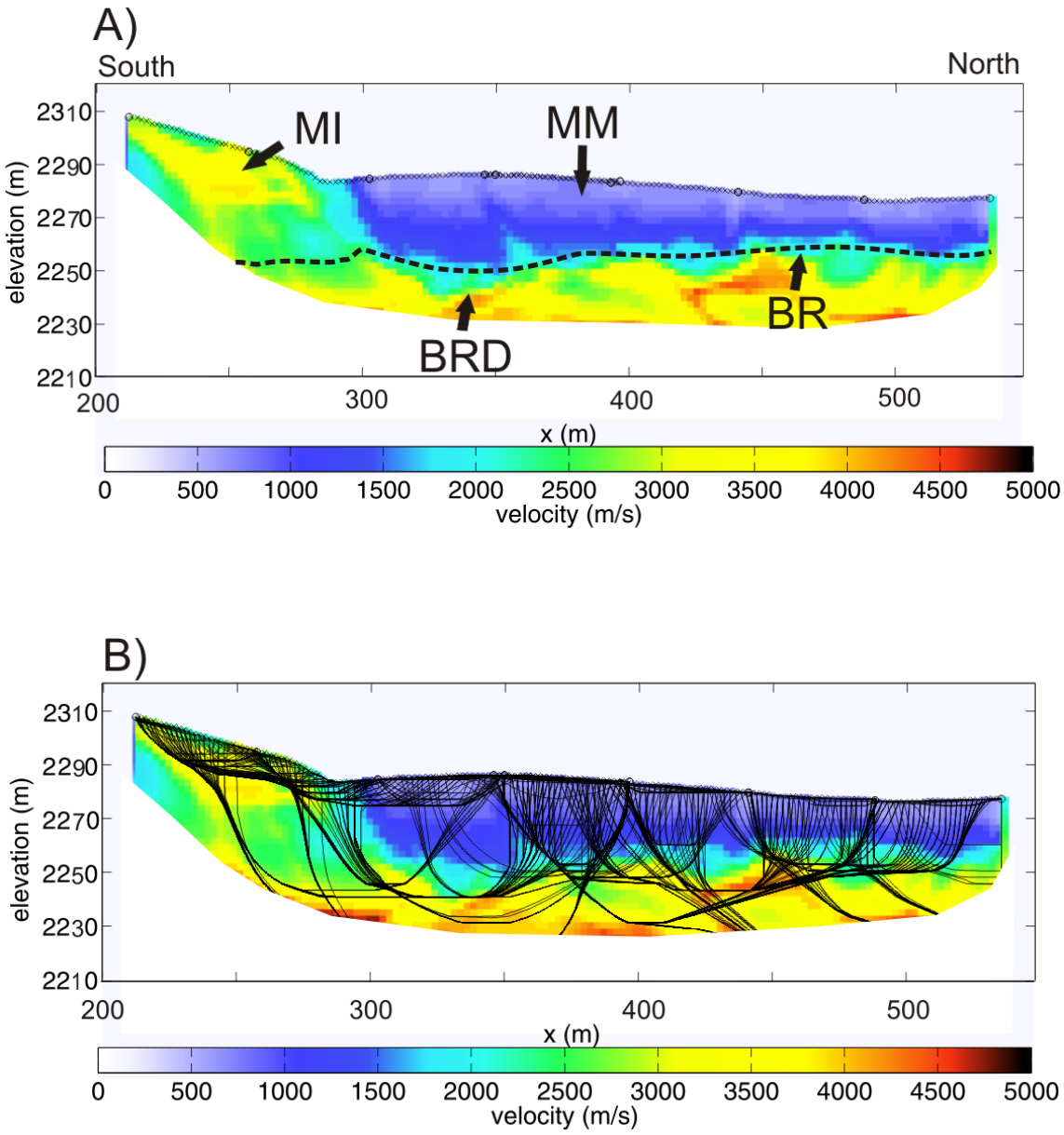
A)
South
North
MI
MM
BR
BRD
elevation (m)
2310
2290
2270
2250
2230
2210
200
300
400
500
x (m)
0
500
1000
1500
2000
2500
3000
3500
4000
4500
5000
velocity (m/s)
B)
elevation (m)
2310
2290
2270
2250
2230
2210
200
300
400
500
x (m)
0
500
1000
1500
2000
2500
3000
3500
4000
4500
5000
velocity (m/s)

Figure 2-8. A) Seismic line 1 tomogram. Massive ice (MI) is indicated by the high velocities seen in the same ridge as the high resistivity values. No indication of massive ice occurs in the moraine below the ridge and this region is interpreted as unfrozen moraine material (MM). Bedrock is interpreted as the high velocity later at the bottom of the image (BR and dashed line). A depression in the bedrock (BRD) may be the result of glacial scouring and could provide a site for groundwater storage.

B) Ray traces indicate areas below the high velocity layer and at the edges of the model are poorly constrained. Dense ray coverage in the shallow subsurface and the middle of the model indicates regions that are well constrained.

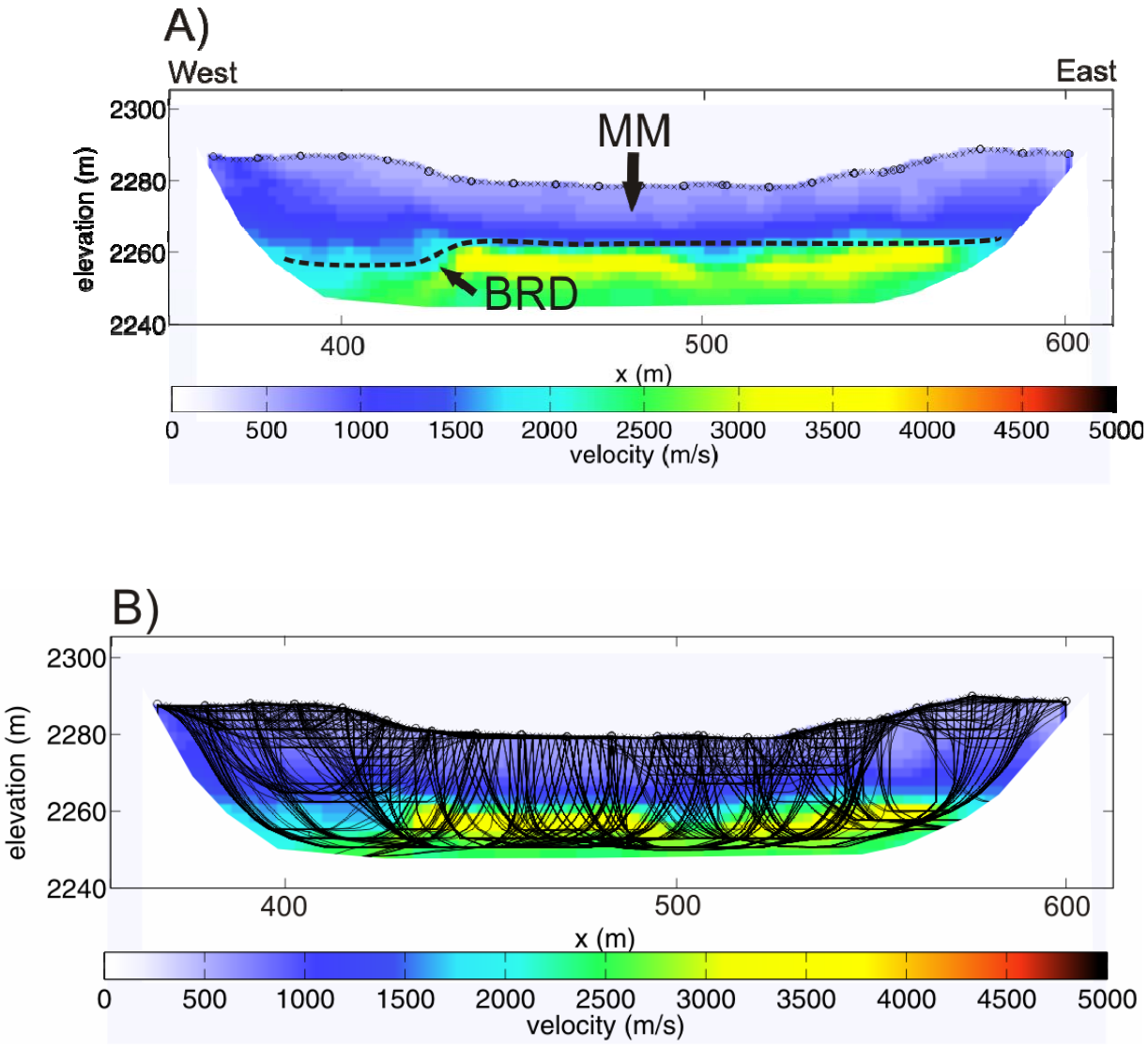

Figure 2-9. A) Seismic line 2 tomogram. The interpreted top of bedrock is again represented by the dashed line. This image is hypothesized to be perpendicular to groundwater flow. Thus, the depression in the bedrock (BDR) may play an important role in routing groundwater flow. There is no indication of ice or permafrost in the moraine material (MM) above the bedrock layer. B) Ray traces indicate the model is fairly well constrained throughout the image.

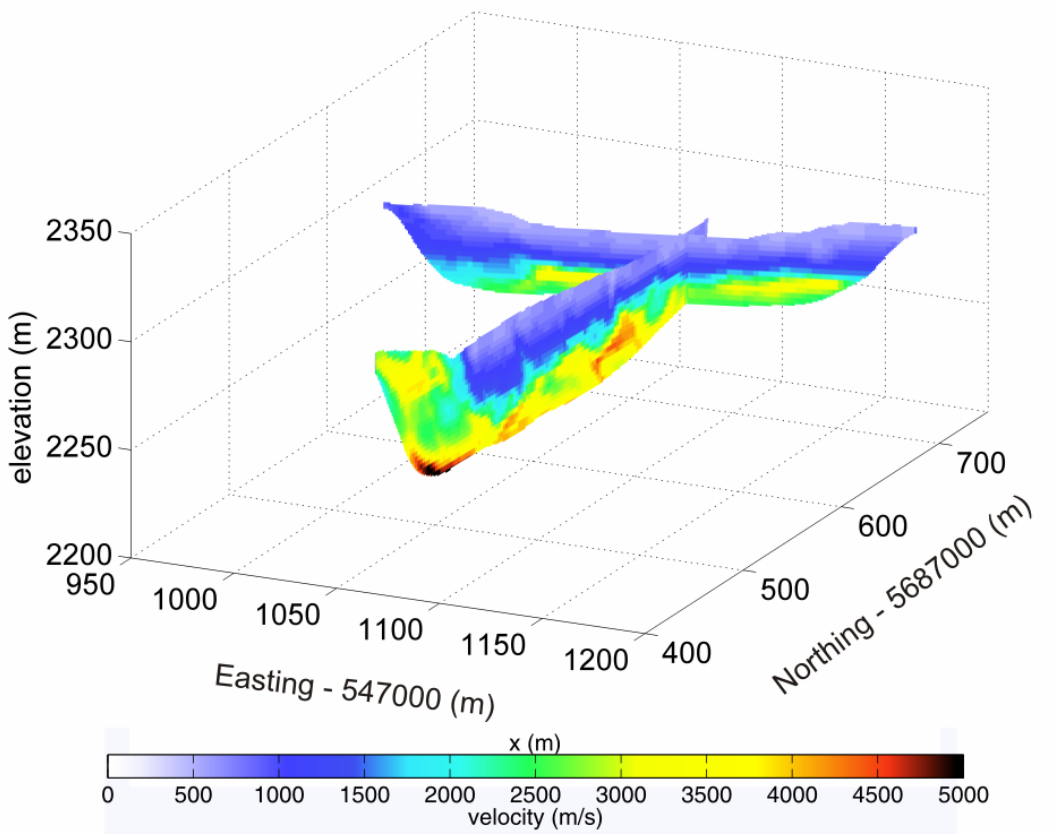

Figure 2-10. Tomograms for seismic line 1 and 2 plotted together. Consistency in the boundary locations and values at the cross location provides confidence in the results of this method. Differences in the total depths of the models are the result of larger shot spacing for seismic line 1.

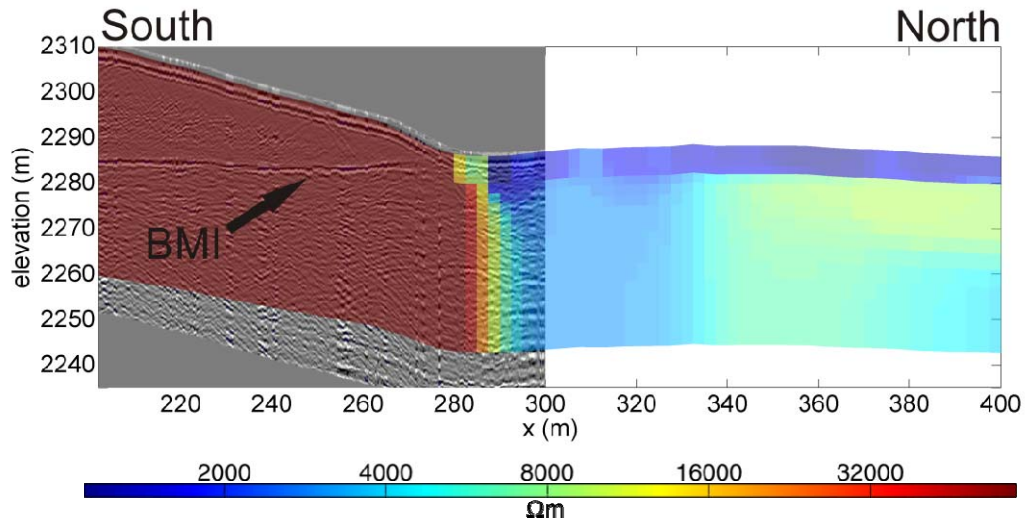

Figure 2-11. GPR profile overlain on ERI 1 tomogram. The strong reflection at c.a. 2287 m likely represents the bottom of the massive ice. The high resistivity of the ice prevents current flow to this region resulting in this boundary being undetected by the electrical resistivity model.

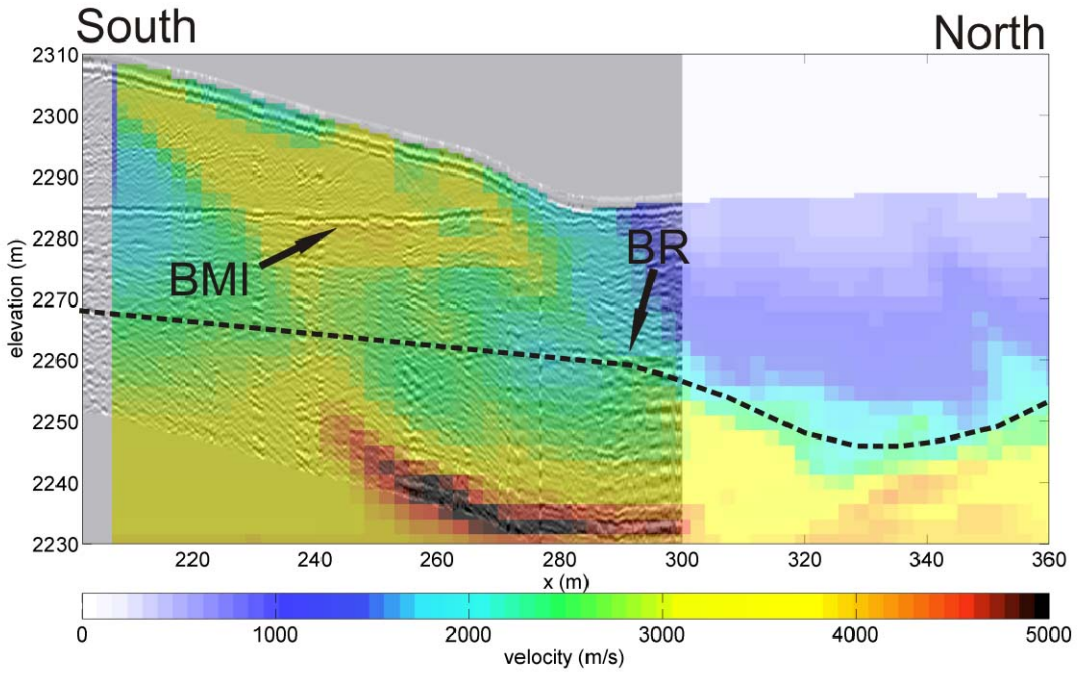

Figure 2-12. GPR line 1 overlain on the corresponding portion of the seismic line 1 tomogram. The strong reflection (BMI) is interpreted as the bottom of the ice, while the beginning of another reflection appears to correspond with what has been interpreted as bedrock. The hypothesized top of bedrock is delineated by the dashed line.

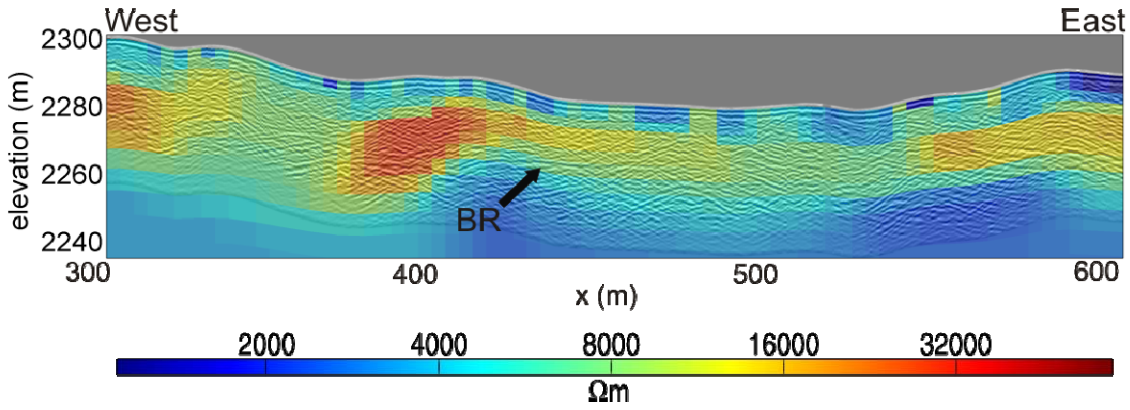

Figure 2-13. GPR line 2 overlain on the corresponding portion of the ERI line 2 tomogram. The GPR reflection indicated by BR, corresponds roughly to the bottom of the more resistive layer. Consequently this reflection is interpreted as the top of the bedrock.

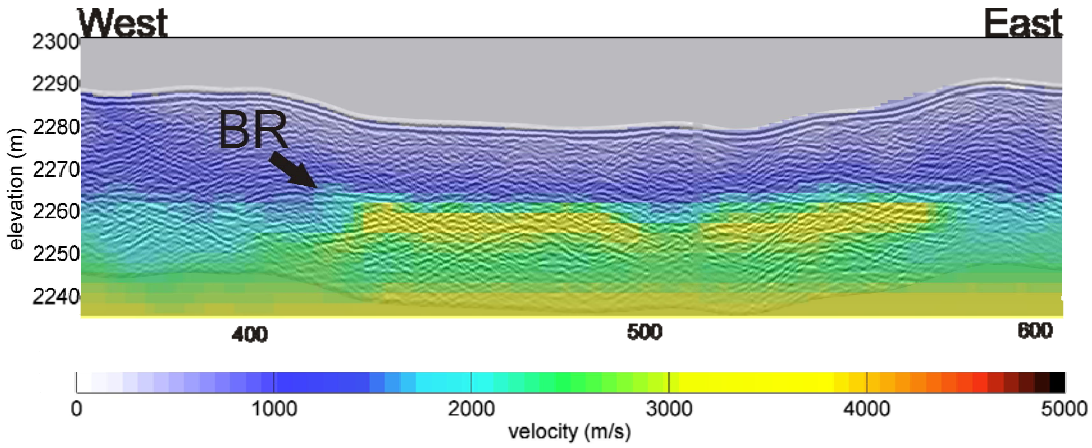

Figure 2-14. GPR line 2 overlain on the corresponding portion of the seismic line 2 tomogram. The reflection appears to correspond with the top of the high velocity layer providing further evidence that this reflection represents the top of the bedrock (BR).

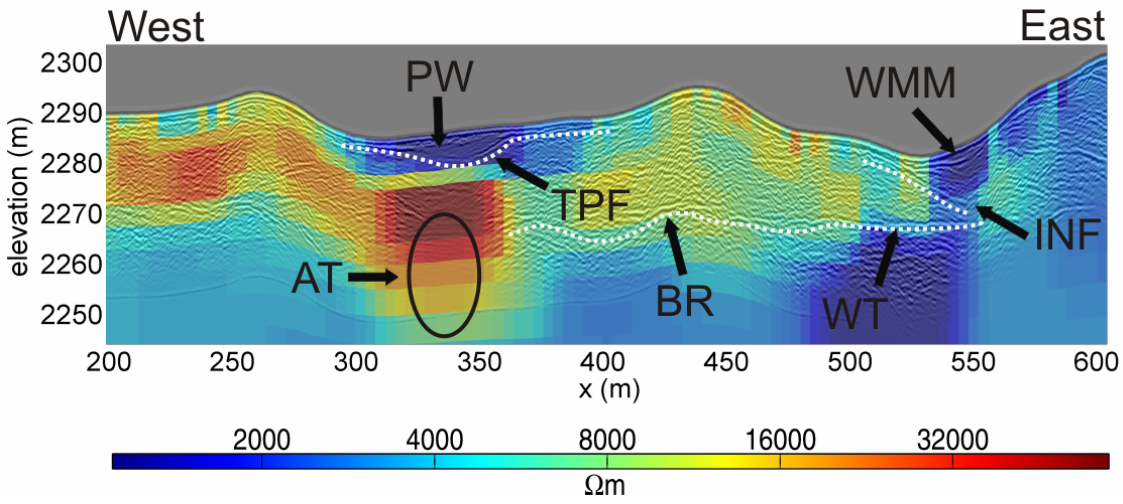

Figure 2-15. GPR line 3 overlain on the ERI line 3 tomogram. The GPR shows considerable detail, with numerous continuous reflections. Key GPR reflections are underlined by a dashed white line The upper reflection is interpreted to be the top of a permafrost layer (TPF), while the lower is interpreted as bedrock (BR) as it coincides roughly with the base of the resistive layer. Further evidence that the conductive region interpreted as perched water (PW) in Figure 6 is provided by the attenuation of the radar signal (AT). The upper and lower reflections appear to pinch out at the eastern end of the image supporting the hypothesis that this region may be a region focused infiltration (INF). Below this region the bottom reflection flattens and overlays a conductive region suggesting the bottom reflection may represent the water table in this region (WT). Attenuation in the radar signal is not pronounced suggesting that the wet moraine material (WMM) above the infiltration point is unsaturated.

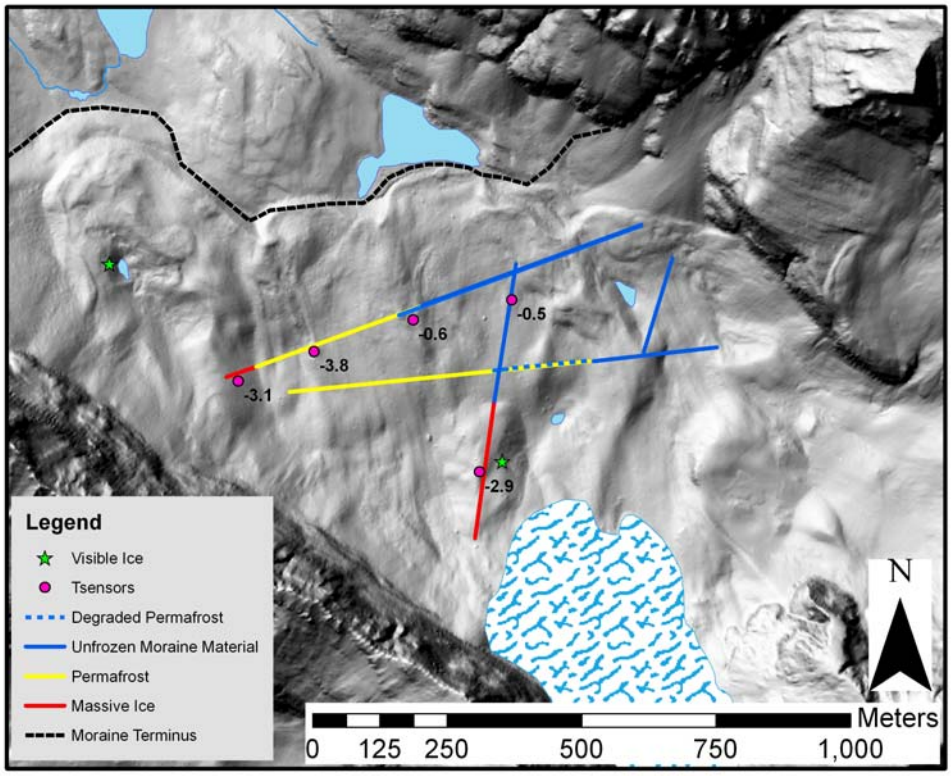

Figure 2-16. Average temperatures are displayed next to the corresponding temperature sensor location. Areas interpreted to be massive ice, degrading permafrost and unfrozen moraine material based on the ERI, seismic and GPR surveys are also shown.

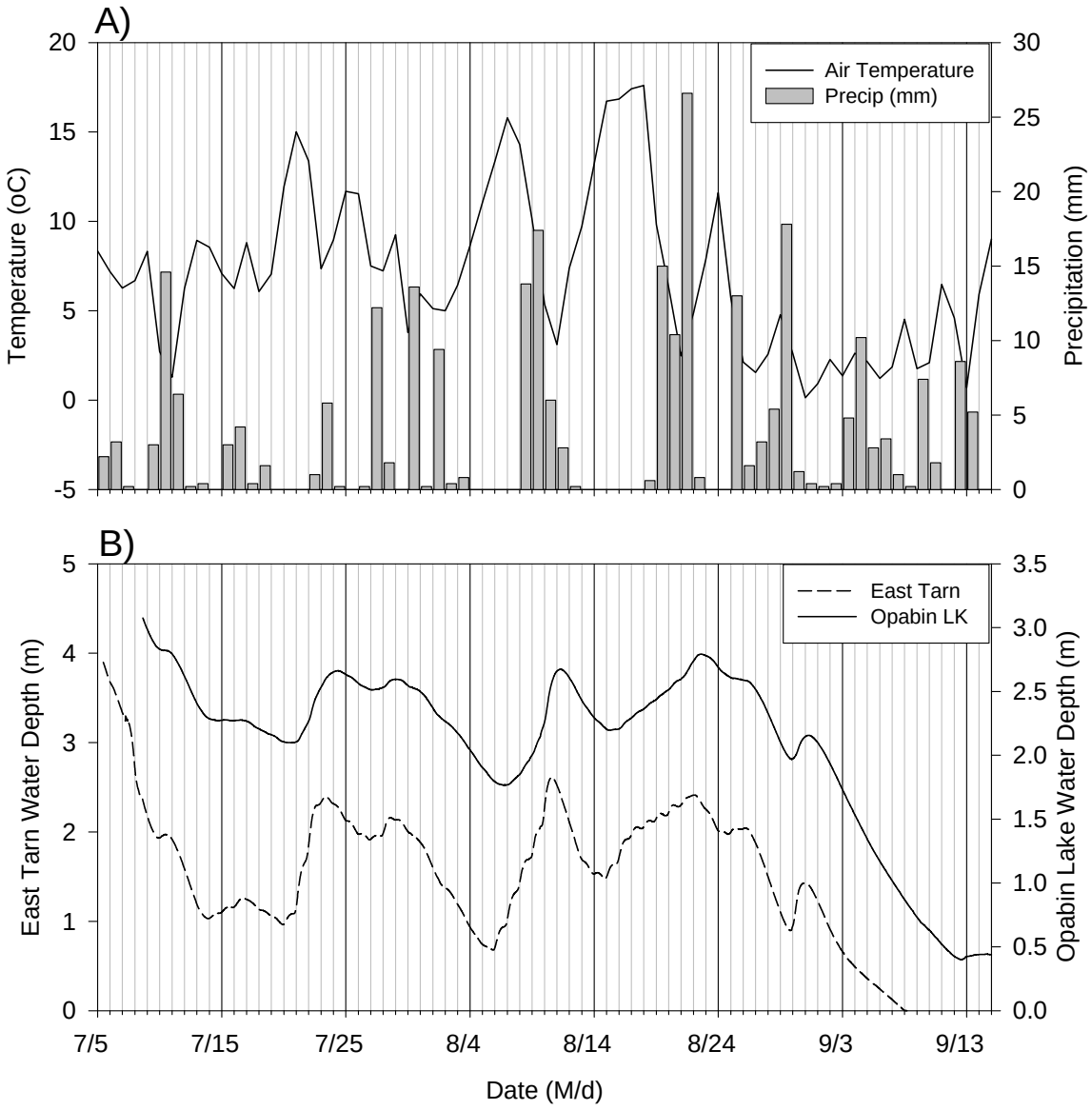
A)
Air Temperature
Precip (mm)
Temperature (oC)
Precipitation (mm)
20
15
10
5
0
-5
30
25
20
15
10
5
0
B)
East Tarn
Opabin LK
East Tarn Water Depth (m)
Opabin Lake Water Depth (m)
5
4
3
2
1
0
3.5
3.0
2.5
2.0
1.5
1.0
0.5
0.0
7/5
7/15
7/25
8/4
8/14
8/24
9/3
9/13
Date (M/d)

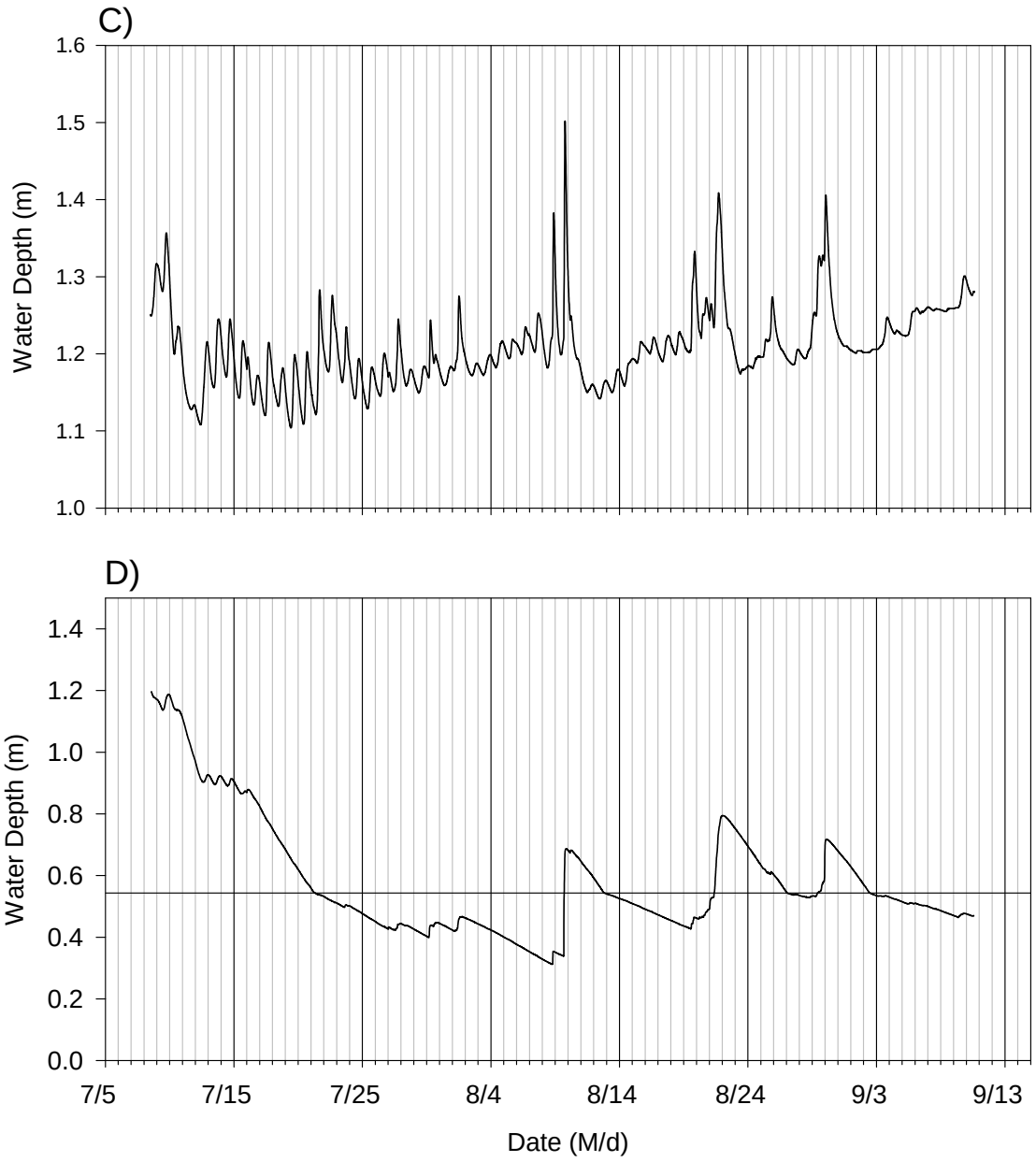

Figure 2-17. A) Precipitation and daily average air temperature, and recorded water level for Opabin Lake and the East Tarn (B), the West Tarn (C) and the South Tarn (D). Vertical grid lines represent 1-day intervals. The horizontal black line in D indicates the consistent break in slope seen in the water level recession curves.

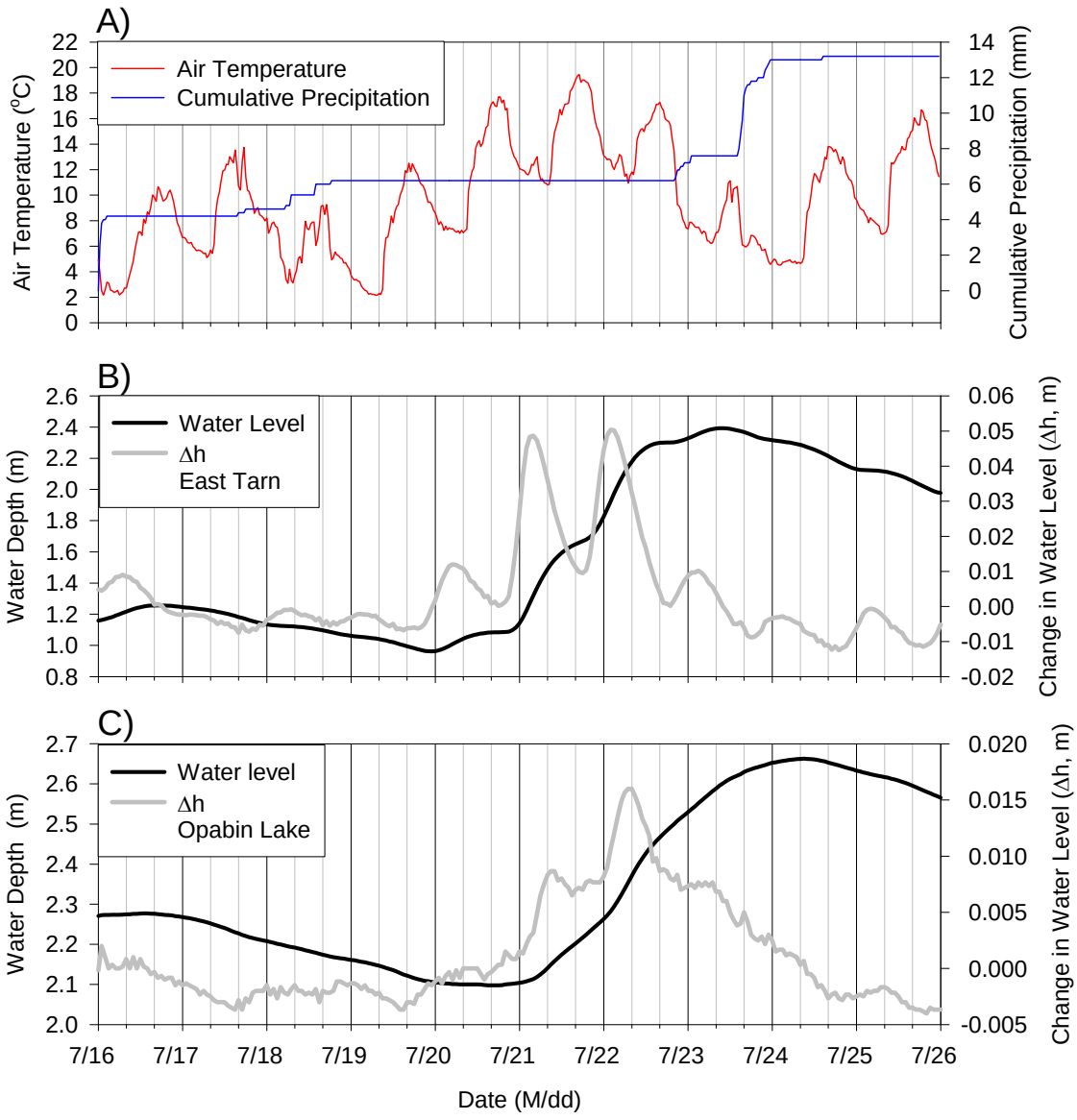

Figure 2-18. A comparison of air temperature and cumulative precipitation (A) with water depth and water level change for the East Tarn (B) and Opabin Lake (C).

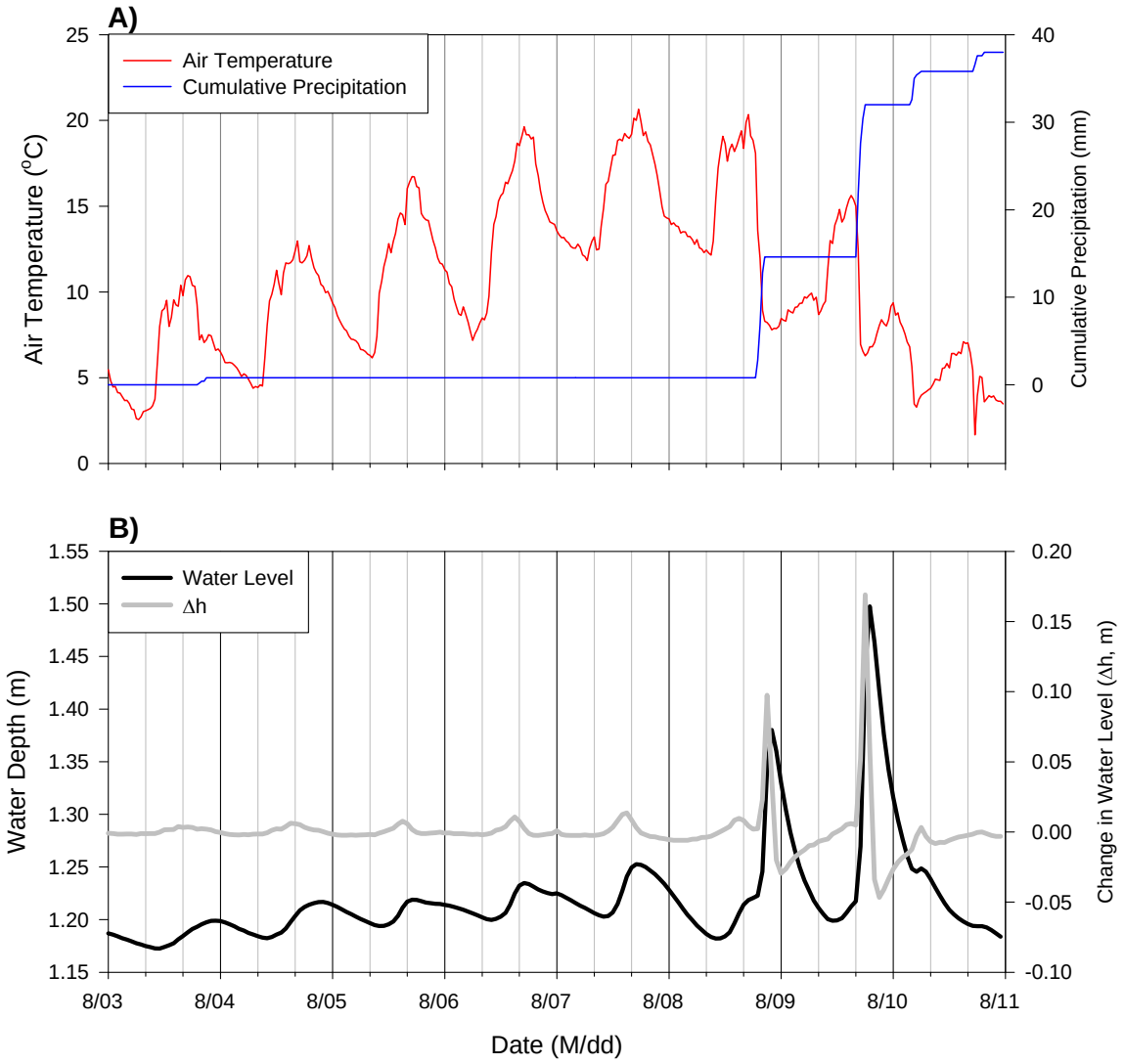

Figure 2-19. A comparison of air temperature and cumulative precipitation (A) with water depth and water level change for the West Tarn (B).

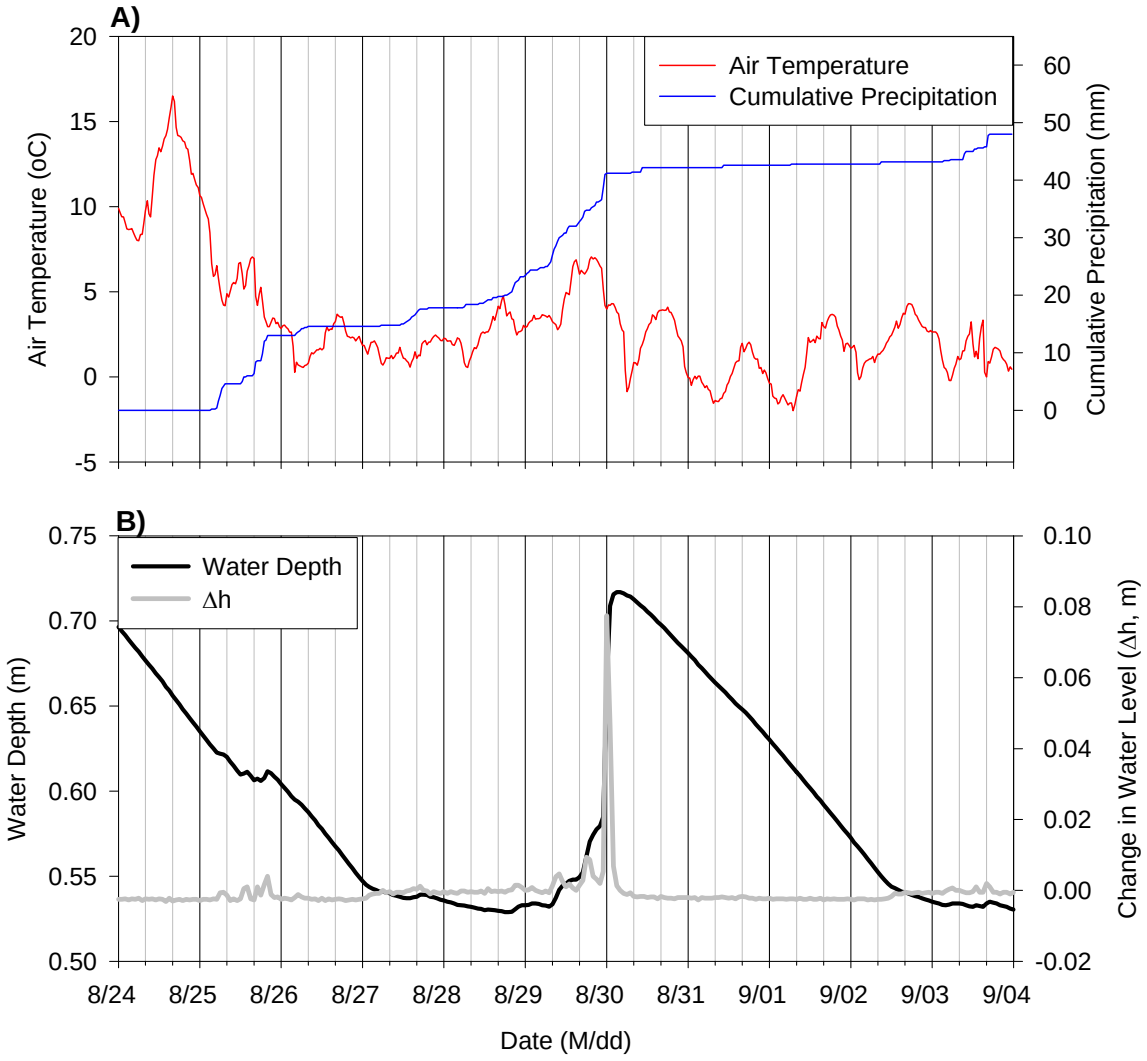

Figure 2-20. A comparison of air temperature and cumulative precipitation (A) with water depth and water level change for the South Tarn (B).

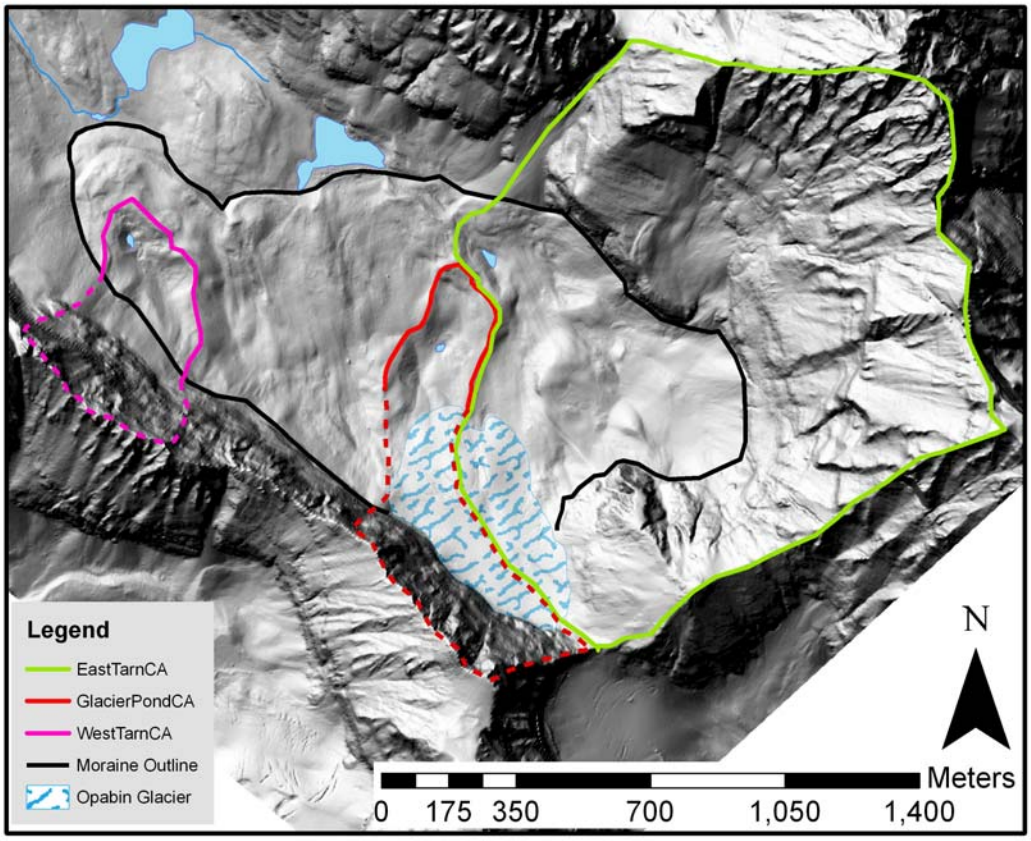

Figure 2-21. Estimated contributing areas are outlined for the East Tarn, South Tarn and West Tarn. Note that although elevation indicates that a portion of the glacier is should contribute melt water to the South Tarn, the hydrograph clearly shows that the South Tarn is unaffected by glacier melt.The dashed portion of the contributing area outline reflects this uncertainty. Similarly, while elevation indicates that melt-water and precipitation from a portion of the north-east facing cliffs should contribute to the West Tarn, this results in a contributing area much larger than that estimated from the hydrographs. Thus, this region is also delineated by a dashed line to reflect its uncertainty.

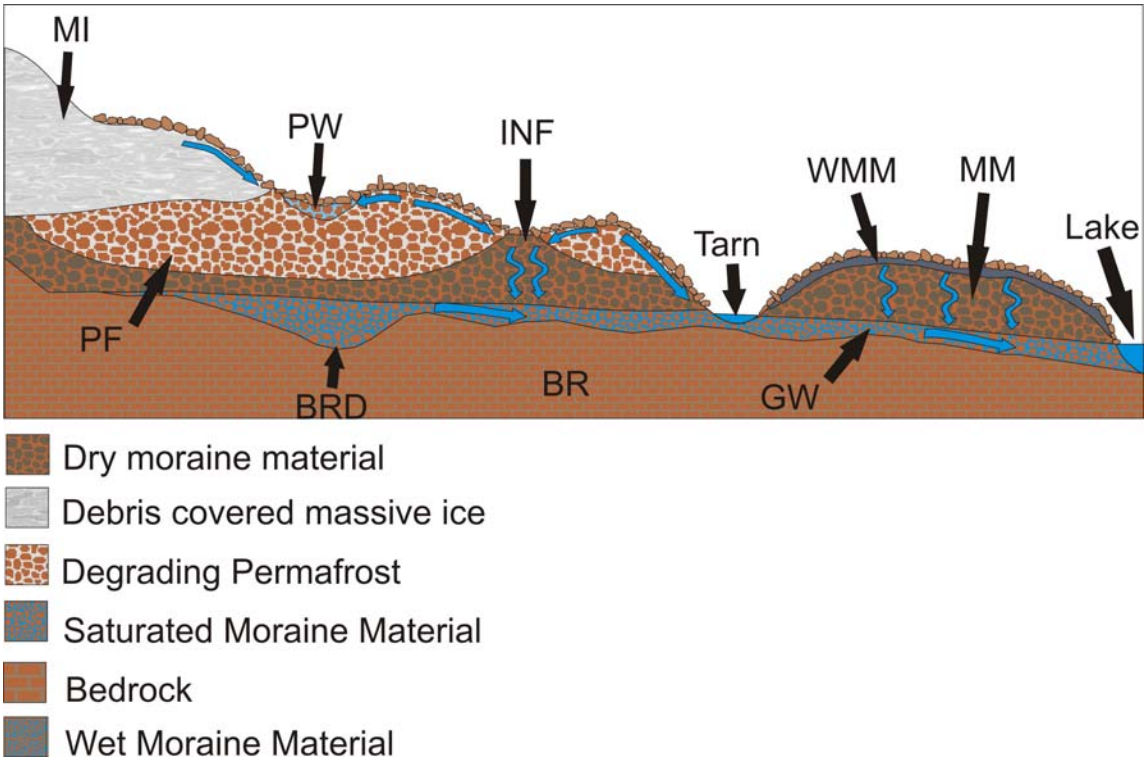

Figure 2-22. Conceptual model of water flow through the moraine based on the geophysical evidence. Labels indicating massive ice (MI), permafrost (PF), perched water (PW), focused infiltration (INF), moraine material, moist moraine material (WMM), bedrock (BR) and a bedrock depression (BRD) and saturated groundwater flow (GW) correspond with features interpreted from the geophysical images presented Section 2.4.

Chapter Three: Characterization of Groundwater – Surface Water Interactions in a Proglacial Moraine Using Heat and Solute Tracers

3.1 Introduction

Alpine watersheds represent an important source of freshwater for many regions of the world, including much of western Canada. These watersheds are dominated by snow and ice melt processes. Thus both the quantity and timing of discharge will likely be affected by changes in local glacier storage, precipitation and snow-cover patterns that are predicted by current climate change scenarios [*IPCC*, 2007]. Less snowfall and earlier snow melt will shift peak discharge away from summer and autumn when demands are highest [*Barnett et al.*, 2005; *Milner et al.*, 2009; *Rood et al.*, 2008; *Tague and Grant*, 2009]. An improved understanding of the hydrological processes in alpine environments will be critical for assessing the complex and changing interactions between climate and watershed hydrology.

Recent studies have shown that groundwater plays an important role in alpine watershed hydrology. Liu et al. [2004] showed that groundwater flow contributes more than two-thirds of stream flow at two study locations in the Colorado Rockies. Hood et al. [2006] used a water-balance approach to show that groundwater inflow accounts for 30 to 75% of the total water input to Lake O'Hara, an alpine lake in the Canadian Rockies. Groundwater is also a significant component of the water balance of two other lakes within the Lake O'Hara watershed [*Roy and Hayashi*, 2008]. In addition, groundwater plays an important role in controlling the timing of watershed discharge and thus has significant implications for water resources mangament [*Tague and Grant*, 2009]. Finally, groundwater can strongly influence both the hydrochemical and thermal

regimes of alpine streams, which in turn, has important ecological implications for benthic and stream organisms [*Bales et al.*, 2006; *Brown et al.*, 2006; *Milner et al.*, 2009].

Coarse deposits, such as moraines, rock glaciers and talus, are thought to play a significant role in groundwater transport and storage. Talus slopes are the primary groundwater reservoirs at a study site in the Colorado Rockies, with groundwater discharge from these deposits accounting for >75% of storm streamflow and winter baseflow [*Clow et al.*, 2003]. Roy and Hayashi [2008] show that in the Lake O'Hara watershed, the Opabin moraine is an important source of groundwater for both an alpine lake and for the major outlet stream of the watershed.

Hydrochemical analyses are commonly used to elucidate groundwater flow pathways in coarse deposits. Results from several of these studies suggest multiple sources and distinct flow paths through coarse deposits, and classify these flow systems by their response times [e.g., fast vs. slow response flow systems; *Brown et al.*, 2006; *Roy and Hayashi*, 2009; *Williams et al.*, 2006]. These studies suggest that a slow response system is likely the result of deeper groundwater flow, whereas a fast flow likely represents shallow subsurface flow along impermeable boundaries such as permafrost and buried ice [*Brown et al.*, 2006; *Tenthorey*, 1992; *Williams et al.*, 2006]. Geophysical data from the Opabin moraine indicates that the deeper groundwater flow is transmitted in a saturated layer at the moraine bedrock interface and controlled by bedrock topography (Chapter 2). Further, large ice and permafrost structures were imaged in the moraine, supporting the hypothesis that fast flow occurs as shallow subsurface flow over these features (Chapter 2).

A key knowledge gap in the current understanding of alpine groundwater systems exists regarding groundwater flow rates and the hydraulic properties (e.g. conductivity, storativity) of coarse deposits, especially in deep groundwater flow systems. In one of only two known studies to examine water flow rates through rock glaciers, Krainer and Mostler [2002] employed dye-tracer experiments to study three rock glaciers in Austria. Their results suggested that groundwater moved through two distinct storage reservoirs, and they hypothesized that both a quickflow and baseflow system were present. They interpreted flow velocities of 0.015 to 0.037 ms^{-1} as representing channelled flow in the quickflow response system (shallow groundwater flow in contact with ice). Baseflow was reported to be relatively minor in these systems and these flow rates were not quantified.

The second study of groundwater flow through rock glaciers also employed a tracer test on three rock glaciers in the Alps [*Tenthorey*, 1992]. This study suggested fast "supra flow" velocities of 0.058 ms^{-1} and "intra flow" velocities of 0.0002 to 0.0004 ms^{-1}. Deeper groundwater flow traveled slower than intra-flow, but again velocities were not quantified. Furthermore, this review of the literature suggests that, no such tracer tests have been conducted on proglacial moraines. Thus, the successful modelling of alpine watersheds will require the parameterization of these deeper groundwater flow systems and of hydrological response units such as moraines.

The lack of information regarding the hydraulic properties of coarse deposits is largely the result of the challenging alpine environment, which makes it logistically difficult and prohibitively costly to install monitoring wells and other infrastructure. Consequently, alternate methods for investigating the groundwater flow systems within

course deposits are required. One potentially useful method is studying groundwater-surface water (GW-SW) interactions. Because surface water is an expression or 'outcrop' of the groundwater system, studying GW-SW interactions can provide useful information regarding the groundwater system [*Siegel*, 2008].

Heat can be an effective natural tracer for investigating GW-SW interactions. Heat has been used to determine groundwater discharge and seepage across streambeds, and to delineate gaining and losing reaches of streams [*Anderson*, 2005; *Conant*, 2004; *Constantz*, 2008; *Hatch et al.*, 2006; *Schmidt et al.*, 2007]. The advection of thermal energy by groundwater to lakes is commonly assumed to be a negligible component of lake energy balance [*Elo*, 2007; *Rodriguez-Rodriguez et al.*, 2004; *Rouse et al.*, 2008], but has been shown to play a significant role in the energy balance of a coastal lagoon [*Rodriguez-Rodriguez and Moreno-Ostos*, 2006]. It is plausible that for small alpine lakes that are heavily influenced by groundwater, such as those in the Lake O'Hara watershed, the advection of heat by groundwater could play an important role in the lake energy balance. If so, a detailed energy-balance study could provide useful information regarding groundwater flow rates through coarse deposits connected to these small lakes and tarns.

Artificial chemical tracers have also been used effectively to investigate GW-SW interactions [*Kalbus et al.*, 2006]. Parsons et al. [2004] performed a whole-wetland tracer experiment to investigate infiltration in a prairie wetland. A chemical mass-balance approach has been used to measure groundwater exchange with alpine lakes in Montana [*Gurrieri and Furniss*, 2004] and to estimate groundwater seepage to and from a closed-basin lake [*LaBaugh et al.*, 1997]. However, LaBaugh et al. [1997] noted that seepage-

rate estimates based on the chemical mass balance did not agree with values determined from flow nets and isotope analysis. They therefore suggested using a combination of hydrogeologic and chemical approaches to determine seepage rates.

Previous work by Roy and Hayashi [2009] and that presented in Chapter 2 has shown that a deep groundwater flow system likely represents the majority of groundwater flow through the Opabin Moraine. The current chapter investigates this deep groundwater flow system by examining the groundwater-surface water interactions between the moraine and a small tarn (East Tarn) that is connected to this flow system, as shown in Chapter 2. The primary objectives of this study were:

1) To determine the complete water balance for the tarn, including groundwater flow into and out of the tarn.

2) To characterize this flow system by determining a value for its hydraulic conductivity.

To address objective 1, two independent tracer experiments were conducted over a six day period during August 2008. The first experiment was a full-tarn chloride dilution experiment, in which groundwater flow out of the tarn was calculated from daily changes in chloride mass within the tarn. The second experiment calculated groundwater flow into the tarn using detailed energy balance measurements to quantify the heat advection by groundwater. These methods provide new approaches for investigating groundwater flow using groundwater – surface water interactions in challenging alpine environments.

Objective 2 was addressed using a numerical simulation of the tarn, and the inverse determination of the model's hydraulic conductivity value based on the calculated

groundwater flow rates determined in objective 1. The sensitivity of the groundwater flow calculations to potential errors is discussed to give an indication of the magnitude of uncertainty associated with these methods. The response of the groundwater flow system to melt and precipitation events is also examined to elucidate the response time of the system to these events and to characterize their relative importance in sourcing groundwater. Together, the results of these experiments and the resulting discussions parameterize a moraine as a hydrologic response unit, and thus make an important contribution to understanding groundwater flow in alpine watersheds.

3.2 Study Site

The Opabin watershed is a small (ca. 5 km^2) alpine watershed located in the Lake O'Hara research basin in Yoho National Park, British Columbia, Canada (Figure 3-1A). The watershed ranges from 2050 to 3490 m.a.s.l. and is characterized by rugged sub-alpine and alpine terrain. By area, the watershed is ca. 60% moraine and talus deposits, 25% exposed bedrock and 15% alpine meadow and sub-alpine forest. Bedrock in this region is composed primarily of thickly bedded quartzite and quartzose sandstone, separated by thin layers of siltstone, sandstone and grey shale of the Cambrian Gog Group. Carbonate rocks of Mt. Whyte, Cathedral, Stephen and Eldon Formations are present in the moraine and talus material [*Lickorish and Simony*, 1995; *Price et al.*, 1980]. A small glacier (the Opabin glacier, ca. 0.2 km^2) is located at the southern end of the watershed, and is separated from the rest of the watershed by a large moraine complex. There is no surface water flow over the moraine. Thus, all snowmelt, glacier melt, and rain that occurs on or up-gradient of the moraine is transported through the

moraine as groundwater. Groundwater from the moraine is discharged from a series of springs located at its western terminus (Figure 3-1B). Groundwater may also discharge into Opabin lake before being re-routed back through the lower moraine to the groundwater springs [*Roy and Hayashi*, 2009]. Geophysical and visual evidence show that regions of the moraine are ice-cored (Chapter 2). Groundwater flow paths through the moraine are therefore hypothesized to be controlled primarily by bedrock topography and buried ice, where it exists.

This study focuses on a small tarn located on the eastern edge of the moraine (hereafter East Tarn; Figures 3-1B and 3-1C). There are no surface water inflows or outflows to the tarn, and previous work (Chapter 2) indicated that the tarn's water balance is groundwater dominated, suggesting that its water level is representative of the local groundwater table. The tarn is ephemeral, generally holding water from the beginning of July to mid-September. Thus, the local water table seems to drop below the bottom of the tarn towards the end of the summer season. The tarn is snow-covered prior to the beginning of July, but water likely saturates the base of the snowpack as the local water table rises in response to spring and early summer snow-melt. A comparison of water levels between the East Tarn, Opabin Lake, and the groundwater springs indicates that the East Tarn is connected to the primary groundwater flow system through the moraine (Chapter 2). Consequently, groundwater flow rates into and out of the tarn are representative of the primary groundwater flow system.

3.3 Methods

3.3.1 Water Balance

A water balance approach was used to investigate the GW-SW interactions occurring at the East Tarn. Since there are no surface water inflows or outflows to the tarn, the water balance equation simplifies to:

$$\Delta S = P - E + GW_{in} - GW_{out} \quad (1)$$

where ΔS is the change in tarn storage (m^3), P (m^3) is the precipitation received at the tarn surface, E (m^3) is evaporation from the tarn surface, GW_{in} (m^3) is the incoming groundwater and GW_{out} (m^3) is the outgoing groundwater.

Both tarn surface area and water volume are directly related to tarn water depth. A digital elevation model (DEM) of the tarn (Figure 3-2A) and the software program Surfer 8 (Golden Software Inc.) were used to develop depth-area and depth-volume relationships following the method outlined by Hayashi and van der Kamp [2000] (Figure 3-2B and 3-2C). The DEM was created from a detailed differential global positioning system (DGPS) survey of the tarn, conducted in mid-September when the water level was sufficiently low to be able to survey the tarn bottom. The relative root mean squared error (RMSE) for the depth-area and depth-volume relationships was 3.5% and 1.5%, respectively. These values indicate that the relationships accurately predict both tarn surface area and volume. Tarn water depth was measured every 10 min with a pressure transducer (In-situ Inc., Level troll accuracy ca. ± 0.5 mm), providing a detailed record of changes in tarn depth. The recorded water-level data and the depth area and depth-volume relationships were used to determine tarn surface area and changes in tarn water

storage. A photograph of the tarn taken during the August study period is shown in Figure 3-2D.

Precipitation (mm) was measured using a tipping bucket rain gauge located ca. 1 km northwest of the tarn. The volume contribution of precipitation to the tarn was calculated as the amount of precipitation multiplied by the area of the tarn surface. The latter was determined from the depth-area relationship describe above (Figure 3-2B).

Evaporation from the tarn surface was measured from August 3 to September 3 2008, using a floating evaporation pan with a surface area of 700 cm^2. Note that due to the floating tipping bucket drifting into shore and precipitation events, reliable evaporation data was only available for August 3, 5, 6, 7, 13, 14, 16, 17, 23 and 24. Evaporation for August 4 was extrapolated from the August 3 and 5 values. Volumetric evaporation was then calculated using the average daily surface area of the tarn, as determined from the depth-area relationship and the daily measured evaporation rate.

The water balance equation (Eq. 1) was solved simultaneously with a chloride mass balance equation or an energy balance equation to determine GW_{in} and GW_{out} (see below).

3.3.2 Chloride Mass Balance

A chloride dilution experiment was conducted from August 3 to 8 to determine the groundwater components of the tarn water balance. Chloride concentration in the tarn was increased by a one-time injection of 44 kg of sodium chloride (NaCl) on August 3, using a method similar to that described by Parsons et al. [2004]. This mass of NaCl was determined based on preliminary estimates of the Cl mass require to measurably elevate

tarn Cl concentration, but was limited by the amount that could be reasonably transported to the site. The NaCl was dissolved in 20-L pails of cold tarn water until saturation was reached before being transferred in solution to seven, 20- to 30-L containers with spigots. The solution was then distributed over the tarn surface as evenly as possible by draining the solution through the spigots while paddling around the tarn over a 1 h period. After all the solution was added, the tarn surface was mixed by vigorous paddling before being left to equilibrate.

The chloride mass balance within the tarn can be calculated as follows:

$$\Delta(CV) = C_P P - C_{tarn} GW_{out} + C_{gw} GW_{in} \quad (2)$$

where C is the chloride concentration for each storage / flux term. Thus, $\Delta(CV)$ is the change in chloride mass in the tarn, $C_P P$ is the chloride mass contribution from precipitation, $C_{tarn} GW_{out}$ is the chloride mass loss from groundwater outflow, and $C_{gw} GW_{in}$ is the chloride mass contribution from groundwater inflow. No precipitation was recorded from August 2 to 9, so the chloride contribution due to precipitation ($C_P P$) was zero. Groundwater chloride concentration (C_{gw}) was assumed to be constant and equal to the concentration of the tarn on August 2 (1.3 mg/L), determined as described below.

Tarn chloride concentration was determined from the chloride concentration of water samples and measurements of tarn-water electrical conductivity (EC). Samples were collected daily, using a pre-rinsed syringe and flexible plastic tubing, from three depths (bottom, middle and top) at six marked locations (Figure 3-2D). Water sampling started the day before the NaCl was added (August 2) and continued until the chloride concentration returned to background levels (August 8). Sample bottles were rinsed three

times with filtered sample water before use and each sample was filtered in the field using a 0.45 μm disposable filter. Water temperature and electrical conductivity (EC) were measured for each sample. EC measurements were corrected to 25 ^{o}C [*Hayashi*, 2004]. Chloride concentration was determined using ion-exchange chromatography. Linear relationships between EC and chloride concentration were determined for each day of the experiment using the chloride concentration of water samples and the corresponding EC measurements. These relationships were used to convert EC measurements to chloride concentrations (Figure 3-3). The relative RMSE for each relationship ranged from 12 to 15%, with the exception of the August 7, for which it was 21%.

To account for spatial variability in chloride concentration within the tarn, transects of EC and temperature measurements were conducted along the major tarn axis on August 2 and from August 4 to 8 (Figure 3-2D). A transect was not conducted on August 3 due to time constraints. Temperature and EC were measured every 2 m at three depths (bottom, middle and top). EC measurements were corrected to 25 ^{o}C and converted to chloride concentration. A two dimensional profile of chloride concentration was generated using the kriging interpolation method in Surfer 8 [*Cressie*, 1991]. Kriging was performed in order to visualize chloride distribution within the tarn only, and was not used in the calculations of chloride concentration described below.

Chloride concentration in the tarn (C_{tarn}) was assumed to equal the average chloride concentration of the cross sectional surveys. Thus, C_{tarn} was determined as the volume-weighted average of the calculated (EC transects) and measured (water samples) chloride concentrations using the following equation:

$$C_{tarn} = \frac{C_1 \times V_1 + C_2 \times V_2 + C_3 \times V_3}{V_1 + V_2 + V_3} \quad (3)$$

V_1, V_2 and V_3 are water volumes determined by dividing the tarn into three sections of equal depth and using Surfer and the tarn DEM to determine the volume of each section. C_1, C_2 and C_3 are the arithmetic averages of chloride concentration for each corresponding volume.

The uncertainty associated with C_{tarn} values was calculated as follows:

$$Wy = \sqrt{\left(\frac{V_1}{V_T} \times W_1\right)^2 + \left(\frac{V_2}{V_T} \times W_2\right)^2 + \left(\frac{V_3}{V_T} \times W_3\right)^2} \quad (4)$$

where Wy is the uncertainty in the volume-weighted average chloride concentration of the tarn (%), V_T is the total volume of the tarn, and W_1, W_2 and W_3 are the standard deviations of C_1, C_2, and C_3 respectively (expressed as a percentage of the arithmetic average)[*Genereux*, 1998]. This uncertainty ranged from 8.8 to 11.9%, with the exception of August 6, for which the uncertainty was 16.4%.

The change in chloride mass ($\Delta(CV)$) was then determined by:

$$\Delta(CV) = \left(C_{tarn}(t_i) \times V_{tarn}(t_i) - C_{tarn}(t_{i-1}) \times V_{tarn}(t_{i-1})\right) \quad (5)$$

where $C_{tarn}(t_i)$ is the tarn concentration at the i^{th} time step as calculated by Eq. 3 and $V_{tarn}(t_i)$ is the volume of the tarn at the i^{th} time step determined using the depth-volume relationship.

The groundwater flux out of the tarn was calculated by simultaneously solving equations 1 and 2, which yields:

$$GW_{out} = \frac{\Delta(CV) - C_{gw} \times \Delta S - C_{gw} \times E}{C_{gw} - C_{tarn}} \quad (6)$$

Groundwater flux into the tarn was then calculated from Eq. 1.

3.3.3 Energy Balance

Groundwater flow into the tarn (GW_{in}) results in the advection of energy and can thus be calculated from the advection term (Q_a) of the tarn energy balance equation. To do this, the remaining energy balance terms must first be determined.

The energy balance of the East Tarn can be written as follows:

$$Q_n + Q_a + Q_P + Q_E + Q_H + Q_{cond} = Q_w \quad (7)$$

where, Q_n is net radiation, Q_a is net advection of energy by groundwater, Q_P is the energy contribution due to precipitation, Q_E is the latent heat flux, Q_H is the sensible heat flux, Q_{cond} is the energy lost or gained from the tarn due to conduction through the tarn bed, and Q_w is the energy stored in the lake. Note all terms are expressed as total energy (Joules) over a time interval of computation.

Net radiation was determined by measuring incoming shortwave and longwave radiation and calculating outgoing shortwave and longwave radiation. Incoming radiation was measured with a CNR1 net radiometer (Kipp and Zonen) located ca. 10 m from the tarn. Based on the manufacturer specifications, the expected accuracy of the CNR1 sensor for daily totals is ± 10%. Due to difficult terrain and large fluctuations in tarn water levels, the net radiometer could not be installed directly over the tarn surface to measure outgoing radiation directly; thus outgoing radiation components were calcualted. Outgoing shortwave radiation was calculated using an albedo for the tarn surface of 0.064

[*Cogley*, 1979]. Outgoing longwave radiation was calculated using the Stefan-Boltzman equation:

$$LW_{out} = \sigma \varepsilon T_s^{\,4} \tag{8}$$

where σ is the Stefan-Boltzman constant (5.67 x 10^{-8} $Wm^{-2}K^{-1}$), ε is the emissivity of water (0.95)[*Oke*, 1988], and T_s is the temperature of the tarn surface (K) as measured by thermistor (Campbell Scientific 107B, accuracy ± 0.2 K) shielded from direct solar radiation. Radiation components were measured or calculated in Wm^{-2} and converted to W using the tarn depth-area relationship. These values were then converted to Joules base on the computational interval time.

The energy contribution to the tarn due to rainfall was calculated as:

$$Q_P = Pc_p \rho_w \left(T_{rain} - T_{tarn}\right) \tag{9}$$

where ρ_w is the density of water, T_{tarn} is the average tarn temperature (^oC), and T_{rain} is the temperature of rain (^oC). Rain temperature was assumed to be equal to air temperature during rain events. Rainfall amount was measured as described for the water balance, whereas air temperature was measured using a shielded thermistor (Campbell Scientific HMP45C, accuracy ± 0.2 ^oC) installed at the same location as the net radiometer.

The energy lost from the tarn due to evaporation (Q_E) was calculated as:

$$Q_E = -E\lambda_v \rho_w \tag{10}$$

where λ_v (2.5 x 10^6 J kg^{-1}) is the latent heat of vapourization.

The Bowen Ratio method was used to estimate the sensible heat component of the energy balance ($Q_{H,}$) from Q_E:

$$Q_H = \beta Q_E \tag{11}$$

where β is the Bowen ratio, calculated as:

$$\beta = \gamma \frac{(T_s - T_{air})}{(e_s - e_{air})} \quad (12)$$

where γ is the psychometric constant (kPa K^{-1}) , T_{air} is the temperature of the air measured by a thermistor (HMP45C), ca. 2 m above the ground surface at the same location as the net radiometer. In Equation 12, e_s (kPa) is the vapour pressure of the tarn surface (equal to the saturated vapour pressure, e_s^*)[*Dingman*, 2002]:

$$e_s = e_s^* = 0.611 \cdot \exp \frac{(17.3 \cdot T_s)}{(T_s + 273.3)} \quad (13)$$

and, e_{air} is the vapour pressure of the air calculated as:

$$e_a = RH \cdot e_a^* \quad (14)$$

where *RH* is the relative humidity (expressed as a ratio) as measured 2 m above the ground surface by the HMP 45C sensor (accuracy ± 2%), and e_a^* is the saturated vapour pressure calculated by:

$$e_a^* = 0.611 \cdot \exp \frac{(17.3 \cdot T_a)}{(T_a + 273.3)} \quad (15)$$

where T_a is the air temperature in ^oC as measured by the HMP 45 sensor.

The psychometric constant was calculated as:

$$\gamma = \frac{ca \cdot P_a}{0.622 \cdot \lambda_v} \quad (16)$$

where c_a is the specific heat of air (1.00 x 10^{-3} MJ kg^{-1} K^{-1})[*Dingman*, 2002]. P_a is the barometric pressure measured by a pressure sensor (Vaisala PTB101B) located at the Lake O'Hara weather station ca. 4 km from the tarn, and corrected for elevation

differences. The constant 0.622 is the ratio of the molecular weight of water to the molecular weight of dry air.

Heat conduction from the tarn was estimated using the analytical solution for heat transfer from an ellipsoid (Hayashi pers. comm.). The thermal conductivity of saturated moraine material was calculated to be 1.5 W m^{-1} K^{-1}, using the following equation from Côté and Konrad [2005]:

$$k_{sat} = k_s^{1-n} \cdot k_w^n \quad (17)$$

where k_{sat} is the saturated thermal conductivity of the material, k_s is the thermal conductivity of the solid particles (3.4 $Wm^{-1}K^{-1}$). Solid particles were assumed to be limestone based on the composition of moraine material (carbonate rocks of the Mt. Whyte, Cathedral, Stephen and Eldon Formations [*Lickorish and Simony*, 1995; *Price et al.*, 1980], k_w is the thermal conductivity of water (0.6 $Wm^{-1}K^{-1}$), and n is the porosity (estimated to be 0.3, based on the porosity of newly deposited basal till [*Ronnert and Mickelson*, 1992]).

The rate of energy storage in the lake (Q_w from Eq. 7) was calculated by:

$$Q_w = \Delta T_{tarn} \cdot c_p \rho_w V \quad (18)$$

where ΔT_{tarn} is the change in water temperature, c_p is the specific heat of water (J kg K^{-1}), and V is the volume of the tarn (m^3).

For August 2 and 4 to 8, tarn temperature was calculated from temperatures recorded during the transect surveys using the same volume averaging method described above (Eq. 4). Uncertainty in the average tarn temperature values (determined using Eq.

5) ranged from 6.7 to 11.9%, indicating that average tarn temperature (and therefore Q_w) was well constrained.

Energy-balance calculations were also made for other days when evaporation was well constrained (August 5,6, 7, 13, 14, 16, 17, 23, 24). Note that evaporation was not well constrained for August 4 as mentioned in section 3.3.1, or for August 8 which received precipitation late in the day after the interval of computation for the more detailed tracer experiments. A vertical profile of temperature in the deepest region of the tarn was recorded from August 2 to September 3 and used to determine average tarn temperature during these days. Temperature was recorded every 30 min by copper constantan thermocouples positioned every 20 cm from the bottom of the tarn to a height of 140 cm above the bottom. When tarn water depth was > 140 cm, tarn temperature was linearly interpolated between 140 cm above the tarn bottom and the tarn surface, where temperature was measured by a floating thermistor as described above. A linear relationship between the average tarn temperature measured by the thermocouple profile and average temperature based on the transect measurements was determined and used to correct the profile temperature average (Figure 3-4). The relative RMSE of this relationship was 2.3%, indicating that this relationship accurately predicted average tarn temperature from the vertical temperature profile for August 2 to 8. This relationship was used to calculate average tarn temperature, and subsequently $Q_{w,}$ for dates for which evaporation was well constrained, allowing energy balance calculations of GW_{in} and GW_{out} to be made for this extended period.

The net advection component (Q_{a}) of the energy balance equations can be written as:

$$Q_a = c_p \times \rho_w \left[GW_{in} \left(T_{gw} - T_o \right) - GW_{out} \left(T_{tarn} - T_o \right) \right] \quad (19)$$

where T_{gw} is the temperature of the groundwater and T_o is the reference temperature (taken to be 0 ^oC, the minimum possible water temperature).

Groundwater temperature during this study (0.6^oC) was determined as the average between the estimated lower and upper bounds for groundwater temperature within the moraine. Since buried ice exists in some regions of the moraine, groundwater in contact with this ice would have a minimum temperature of 0 ^oC representing the lower bound for groundwater temperature. At an ice-free region of the moraine ca. 200 m west of the tarn, annual mean soil temperature for 2008 at 40-cm depth was 1.3 ^oC; (Jaime Hood, unpublished data). This temperature is hypothesized to represent the upper bound of groundwater temperature within the moraine as water in contact with this sediment would equilibrate to this temperature. Note that the estimate of groundwater temperature used in the energy balance calculations is consistent with the temperature of groundwater in a spring discharging from the Opabin Moraine monitored in 2006 by Roy et. al. [in review, SS2 in Figure 1b]. Over a 4-month period, they found groundwater temperatures at this spring to be very stable, ranging between 0.5 and 0.7 °C and hypothesized this groundwater to have been in contact with ice or directly sourced from snow and/or ice-melt. Note that this temperature is also within the range presented by Krainer and Mostler [2002] for groundwater discharged from active rock glaciers (between 0.5 and 0.8 ^oC, ±0.2 ^oC).

By simultaneously solving Equations 2 and 15, groundwater flow into the tarn can be calculated as:

$$GW_{in} = \left(\frac{Q_a}{c_p \times \rho_w} - \Delta S \times T_{tarn} - E \times T_{tarn} \right) / \left(T_{gw} - T_{tarn} \right) \quad (20)$$

where Q_a is determined as:

$$Q_a = Q_w - Q_n - Q_E - Q_H \quad (21)$$

3.3.4 Estimating Hydraulic Conductivity

The hydraulic conductivity for the dominant flow paths within the Opabin Moraine is estimated using the GW-SW interactions calculated above, and a simple groundwater-flow simulation of the tarn-aquifer system. This approach follows from previous studies that have used steady-state flow models to refine our understanding of GW-SW interactions for shallow lakes by classifying lake-flow regimes and simulating the groundwater flow patterns near lakes [*Nield et al.*, 1994; *Townley and Trefry*, 2000; *Winter*, 1978; *Zlotnik et al.*, 2009]. Although the most recent studies use dimensional analysis to develop useful simplifications for investigating GW–SW interactions within shallow lakes, they assume that lake depth is small compared with aquifer thickness. This assumption is violated by the geometry of the East Tarn – Opabin Moraine system. Therefore, estimates of hydraulic conductivity for the moraine are based on a simple numerical simulation (described below), rather than the dimensionless ratios presented by Townley and Trefry [2000] and Zlotnik et al.[2009]

MODFLOW-2000 (Waterloo Hydrogeologic Inc.), a block-centered finite difference code for modelling saturated flow, was used to construct a numerical simulation of the analytical solution thought to best represent the groundwater flow system around the tarn. Aquifer width was estimated from the DEM as the approximate

distance (120 m) between moraine-surface topographic high points east and west of the tarn. Aquifer thickness was estimated to be 10 m based on geophysical surveys presented in Chapter 2, which indicated bedrock underlying the moraine at an elevation of ca. 2260 m.a.s.l., i.e. 11 m below the bottom of the tarn. The model domain was arbitrarily assigned a length (L) of 240 m, which is sufficiently long to avoid boundary effects. The model domain is represented by a 90 x 60 x 26 cell grid, with the mesh grid being more refined near the tarn (e.g. the centre and top layers of the model domain; Figure 3-5). To simulate the water table, grid cells were marked inactive along the upper boundary of the model. Similarly, cells were inactivated along the bottom of the domain to simulate the bedrock (no flow) boundary. Constant head boundary conditions were used to simulate the tarn within the model and were assigned such that the depth of the model tarn (2 m) was similar to that of the East Tarn from August 4 to 8. Constant head values were also assigned to the up-gradient and down-gradient boundaries of the model to simulate the regional hydraulic gradient, which was estimated from the average water levels of the East Tarn and Opabin Lake from August 4 to 8 (Figure 3-5).

No recharge or evaporative fluxes were assigned to the top layer of the model and the remaining boundaries were assumed to be no-flow. Hydraulic conductivity for the model was estimated by varying its value until groundwater flow through the model tarn approached the average groundwater flux (average of GW_{in} and GW_{out} for both methods) calculated for August 4 to 8.

3.4 Results

3.4.1 Chloride Mass Balance

The spatial distribution of chloride in the tarn is shown in the two-dimensional cross sections generated from the transect surveys (Figure 3-6). The cross sections show some localization of chloride at the deepest regions of the tarn, suggesting that chloride may preferentially accumulate in these regions. Note that the vertical exaggeration for these figures (five to one) exaggerates the vertical appearance of these localized regions. There does not appear to be any consistent longitudinal trend in the spatial distribution of chloride, and in general we interpret the chloride tracer within the tarn to be reasonably well mixed.

Chloride concentration in the tarn decayed exponentially to pre-tracer release levels in approximately five days (Figure 3-7). This relatively quick decay indicates substantial groundwater-surface water exchange. Due to time constraints it was not possible to conduct a transect survey of chloride concentration on August 3. Thus, the initial chloride concentration for the experiment (87.6 mgL^{-1}) was calculated from the amount of chloride added to the tarn and the volume of the tarn at the time of tracer release.

The calculated water balance for the East Tarn is presented in Table 1. Neither precipitation nor evaporation are included in Table 1, since no precipitation occurred during the experiment, and evaporation, which accounted for < 1% of the daily water budget, was deemed a negligible component of the water balance. Groundwater flow out of the tarn calculated from the chloride mass balance ranged from 108 to 510 m^3d^{-1}. Tarn

volume during this period ranged from 72 to 723 m^3, thus daily groundwater flow through the tarn was on the same order of magnitude as the tarn volume.

3.4.2 Energy Balance

During the August 4 to 8 study period, net radiation and the advection term consistently represented significant components of the energy balance for the tarn. Conversely, the relative importance of the energy storage and latent and sensible heat flux terms to the tarn energy balance varied considerably during this period (Figure 3-8). Note that the heat conduction term represented only a minor component of the energy balance. Note also that increases in the sensible heat flux term correspond with increases in the magnitude of the advection term making the influence of the sensible heat flux on tarn temperature appear insignificant. This is illustrated by a comparison of air temperature, water level and water temperature (recorded at the tarn bottom) during this period.

High air temperatures were generally followed by an increase in tarn water level (Figure 3-9). However, tarn water temperature decreased with increased water level, resulting in the counter-intuitive pattern of decreased water temperature with increased air temperature (Figure 3-9). Since, higher air temperatures are associated with periods greater melt, increases in water level are likely the result of increased groundwater flow into the tarn due to melting snow and/or glacier ice and possibly buried ice. The pattern of decreasing tarn-water temperatures with increasing air temperature indicates the temperature of groundwater flowing into the tarn is low. That the cooling effect of increased groundwater flow outweighed any direct warming effect of higher air

temperatures further emphasizes the importance of the advection term in the tarn energy balance. A more detailed comparison of the tarn response to meteorological variables is provided in the discussion.

Cross-sectional plots of temperature provide spatial information regarding groundwater exchange with the tarn (Figure 3-10). The cross section for August 2 shows a lateral increase in temperature from ca. 3 ^{o}C at the south end of the tarn to 5 ^{o}C at the north end (Figure 3-10). This pattern suggests that the tarn acted as a flow-through system, with cool groundwater flowing into the south end of the tarn and gradually warming before flowing out of the tarn at the north end. This is consistent with the direction of groundwater flow hypothesized from surface topography. As water level in the tarn decreases, tarn temperature increases and becomes less variable (see above). Small localized regions of cooler temperatures appear in the deepest regions of the tarn, and likely represent regions of groundwater inflow.

Groundwater flow rates into the tarn calculated from the energy balance ranged from 75 to 930 m^3d^{-1} (Table 3-1). Groundwater flow out of the tarn was calculated using the water balance equation and ranged from 159 to 717 m^3d^{-1}. These values are compared to the values of GW_{out} calculated from the chloride mass-balance approach in Figure 3-11A and Table 3-2.

Whether calculated using the chloride balance or energy balance method, GW_{out} varies with tarn water level, such that as water level increases or decreases so does GW_{out} (Figure 3-11A). Water depth has two important effects on GW_{out}. Firstly, the hydraulic gradient driving flow out of the tarn is likely represent to some degree by the difference in water level elevation between the East Tarn and Opabin Lake. Since water level

increase due to melt and precipitation is larger for the East Tarn than for Opabin Lake, water level increases for the East Tarn likely also represent increases in hydraulic gradient. Secondly, increases in the East Tarn depth also represent increases in the saturated thickness of the local aquifer thereby increase the area available fro water flow. Consequently, the relationship between tarn water depth and GW_{out} likely represents the relationship between the combined effects of increase hydraulic gradient and saturated thickness and GW_{out}. Figure 3-11B shows the relationship between tarn depth and GW_{out} calculated using both the energy and mass-balance methods.

To further investigate this relationship, energy balance calculations were made for August 5, 6, 7, 13, 14, 16, 17, 23, and 24 (i.e. beyond the period for which chloride mass balance data are available) by calculating Q_w from a vertical temperature profile as described in the methods. The conduction component was not included in the calculations, as it played a negligible role in the energy balance (see above). Although the precipitation term was included in the calculations, it too was found to represent a negligible proportion of the energy budget.

Calculated groundwater flow rates (m^3d^{-1}) for August 5, 6, 7, 13, 14, 16, 17, 23, and 24 are plotted against corresponding daily average tarn water levels, including flow rates calculated using the mass balance and more detailed energy balance methods (Figure 3-12). Note that calculated flow rates for August 16 and 17, appear much higher than predicted by the trend determined in Figure 3-11B. This is likely the result of poor quantification of the energy storage term. As described in the methods, transect surveys of temperature were replaced by a single vertical temperature profile and linear interpolation of temperature as water level increased above the top of the temperature

profile. It is likely that this method did not represent the energy stored within the tarn as well as the 2D profiling, and resulted in less accurate predictions of groundwater flow rates. Despite the data variability, the positive relationship between water level and GW_{out} confirms that higher water levels in the tarn result in increased groundwater flow rates.

3.4.3 Estimating Hydraulic Conductivity

The numerical simulation representing the East Tarn-Opabin Moraine groundwater flow system converged with a mass balance difference of <0.15%, indicating that the governing partial differential flow equations are well represented by MODFLOW's algebraic approximations. Particle tracking results show that the depth and width of the capture zone are approximately 9 and 16 m, respectively. The hydraulic conductivity of the model domain was estimated to range between 4.0×10^{-5} to 5.3×10^{-4} m s^{-1} as these values resulted in the best approximations of the minimum and maximum groundwater fluxes for the tarn (ca. 75 and 930 m^3d^{-1} respectively) calculated for the August 4 to 8 period. A hydraulic conductivity value of 1.9×10^{-4} m/s is interpreted to represent a "best guess" estimate as this value resulted in the best approximation of average groundwater flux through the tarn for Aug. 4 to 8 (338.7 m^3d^{-1}). Based on the "best guess" conductivity estimate, groundwater flow rates into and out of the tarn were both 321.5 m^3d^{-1}. Although this approach provides only a rough estimate of hydraulic conductivity, this value seems reasonable for this type of material, and provides an important first estimation for parameterizing this type of hydrological response unit.

3.5 Discussion

3.5.1 Sensitivity and Error Analysis

Sensitivity analysis was performed to determine the response of calculated GW_{out} to changes in the variables used to calculate it, for both the energy balance and chloride mass-balance methods. The individual terms used to calculate groundwater flow rates were individually by ± 5, 10, 20 and 50%, and the resulting change in the calculated groundwater flow rate recorded. This analysis provides an indication of the potential error in groundwater flow rates resulting from measurement errors. Note that the range of variation shown is larger than the expected error associated with each variable. This is done to indicate the possible errors should these methods be employed in future studies with larger degree of data uncertainty.

Sensitivity analyses were performed each day from August 4 to 8 for both chloride mass balance calculations and the energy balance calculations. Results of the sensitivity analysis are presented graphically in Figure 3-13 for the chloride mass-balance method and Figure 3-14 for the energy balance approach.

Calculated values of GW_{out} showed the highest sensitivity to changes in C_{gw} and C_{tarn}. Changes in GW_{out} ranged from -60 to 60% for changes in C_{gw} of -50 and 50% respectively (Figure 3-13A), and from 220 to -60% for changes in C_{tarn} of -50 and 50% respectively (Figure 3-13B). Changes in GW_{out} did not exceed ± 50% given variable changes of ± 20%, with the exception of a -20% change to C_{tarn} on August 8. Note that sensitivity is non-linear for these parameters and that a discontinuity exists when C_{gw} is equal to C_{tarn}. Consequently, the sensitivity of GW_{out} to changes in C_{gw} and C_{tarn} increases with time as C_{gw} approaches C_{tarn}. Variable changes that resulted in $C_{tarn} \leq C_{gw}$

were not included in the sensitivity analysis. With respect to changes in ΔS, GW_{out} became sensitive to changes in ΔS as C_{tarn} decreased. Thus, data from August 8 showed the greatest sensitivity, with changes in ΔS of -50 and 50% resulting in changes in GW_{out} of ca. -30 and 30% respectively. However, with that exception, variations in GW_{out} did not exceed ± 15% for the changes made to ΔS (Figure 3-13C). Conversely, GW_{out} was most sensitive to changes in $\Delta(CV)$ during earlier dates (August 4 and 5) when C_{tarn} was highest. Changes in GW_{out} did not exceed ±50% for the changes made to $\Delta(CV)$ (Figure 3-13D). The sensitivity of GW_{out} to the evaporation term of the chloride mass-balance calculations is not presented, as the effect of this term was negligible.

The relative RMSE's for calculations of chloride concentration from EC measurements were ≤ 21%, and the uncertainty associated with the average chloride concentration values was ≤ 16%. Since the uncertainties in the two variables are independent, the errors associated with C_{gw} and C_{tarn} were < 30% and likely closer to 20%. The relative RMSE of the depth-volume relationship indicates that ΔS is well constrained and that the estimated error associated with this value is < 10%. Since $\Delta(CV)$ is calculated from C_{tarn} and ΔS, the error associated with this value is likely between 10 and 20%. Given this range of possible errors the estimated error associated with mass balance calculations of GW_{out} is < 50%.

Sensitivity analysis results for the energy balance method are presented for changes to net radiation (Q_n), the storage component (Q_w), the latent heat flux (Q_E), the sensible heat flux (Q_H),and groundwater temperature (T_{gw}). Sensitivity analysis for the heat conduction term was not performed since it had a negligible effect on the calculated groundwater flow rates. The sensitivity of GW_{out} to variations in Q_n varied considerably

between days. For changes of up to ± 50% in Q_n, variations in GW_{out} never exceeded ± 100%, and generally did not exceed ± 50% with an exception of net radiation changes of ± 50% for August 4 and 5 (Figure 3-14A). Calculated values of GW_{out} were considerably less sensitive to changes in Q_w and Qe, with changes to GW_{out} not exceeding ±20% given the changes made to these terms (Figure 3-14B and C). Similarly, changes to *GWout* did not exceed ±30% for variations in Q_H (Figure 3-14D). The sensitivity of GW_{out} to variations in groundwater temperature was minimal and did not exceed ± 6% (Figure 3-14E). This is partially the result of the low groundwater temperature, such that changes of ±50% corresponded to temperature changes of only ± 0.3 ^{o}C. Thus, T_{gw} was increased by 1 ^{o}C (200%) to further assess the sensitivity of GW_{out} to groundwater temperature. This increase resulted in only a 20% increase in GW_{out}, indicating the GW_{out} is relatively insensitive to changes in T_{gw}.

Whilst GW_{out} appears most sensitive to changes in net radiation, net radiation is considered well-constrained (error < 10%) based on the measurement accuracy of the net radiometer, the well-defined values of albedo and emissivity, and the ease and accuracy of measuring tarn surface temperature used to calculate LW_{out}. Since the change in GW_{out} did not exceed ± 40% for changes in Q_n of ± 20% or less, expected errors in GW_{out} resulting from net radiation measurement errors are < ± 50%. Since Q_w is calculated from ΔS and average tarn temperature, which is also estimated to be well constrained (uncertainty <12%), the error in GW_{out} due to errors associated with Q_w is estimated to be <10%. Similarly, based on the reasoning for the estimate of groundwater temperature, the errors in GW_{out} due to errors associated with T_{gw} are expected to be <20%. Thus, for

the energy balance calculations it seems unlikely that the error associated with calculated values of GW_{out} exceeds 100%, and I suggest it is likely <50%. Note that the error associated with the extended energy balance calculations is likely higher as the average tarn temperature values are less well-constrained.

Although the sensitivity analyses showed the possibility of considerable error associated with calculations of GW_{out}, the consistency in results generated by energy balance and chloride mass balance methods provides confidence in their accuracy. A comparison of GW_{in} and GW_{out} values calculated using these methods is shown in Table 2. With the exception of GW_{out} for August 6 and 7, the difference between values is <70%, which is within the range of possible error attributed to measurement and assumption errors. The cause of the higher difference noted on August 6 and 7 remains unclear, however this suggests that the errors in groundwater flow calculations for this day are slightly higher than the errors estimated above.

3.5.2 Characterizing the Groundwater Flow System

Water balance calculations provide important information regarding groundwater-surface water interactions and the hydrologic response of the groundwater flow system. Fundamentally, the flow regime of shallow groundwater-dominated lakes can be classified as either a recharge lake ($GW_{in} > 0$ and $GW_{out} = 0$), a flow-through lake ($GW_{in} > 0$ and $GW_{out} > 0$), or a losing lake ($GW_{in} = 0$ and $GW_{out} > 0$) [*Born et al.*, 1979]. Based on this classification scheme, the East Tarn clearly acts as a flow through lake. The response time of the flow system to precipitation and melt events can be assessed by

comparing the water balance with meteorological measurements such as air temperature, precipitation and net radiation.

Previous work (Chapter 2) has shown that snow and ice melt contributes significantly to increases in tarn water level and thus groundwater flow. To further assess this, the East Tarn water balance is compared with net radiation calculated over a hypothetical snow surface. The tarn water balance for July 24 to September 4 was calculated using the regression equation from Figure 3-11 to calculate GW_{out}, the depth-volume relationship to calculate the change in tarn water storage, and Equation 2 to calculated GW_{in}. A comparison of the tarn water-balance with air temperature, cumulative precipitation and net all-wave radiation for a snow surface (a source of melt water) is shown in Figure 3-15. The incoming components of the net radiation estimate were equal to the incoming shortwave and longwave components measured for the energy balance experiment. Outgoing shortwave radiation for the snow surface was calculated using an albedo estimate for old snow [0.4, *Oke*, 1988] and outgoing longwave was calculated from Eq. 8 using a surface temperature of 0 ^{o}C. The comparison shown in Figure 3-15 indicates that GW_{out} lagged GW_{in} and ΔS by ca. half a day. Peaks in GW_{in} generally follow periods of high net radiation and air temperature, supporting the results of Chapter 2 that suggested groundwater flux into the tarn is dominated by snow and or ice-melt events. At this time scale of comparison, it is difficult to ascertain the response of GW_{in} to precipitation events and to accurately determine the time lag between melt events and GW_{in} response. Consequently, a comparison of the tarn water balance with the meteorological measurements described

above is provide for August 3 to 10 and for August 24 to September 4 in Figures 3-16 and 17, respectively.

The response of the tarn water balance to melt events (i.e. high net radiation and temperature) is best illustrated by Figure 3-16. Increasing net radiation and air temperature starting on August 5 resulted in pronounced diurnal fluctuations superimposed on an overall increase in GW_{in}, with peak GW_{in} occurring at ca. 0200h. Thus, peak GW_{in} appears to lag behind peak net radiation by ca. 16 h, and behind peak air temperature by ca. 12 h. This time lag indicates that the melt water pulse travels some distance before reaching the tarn and is not the result of shallow subsurface runoff in the tarn's immediate vicinity. Comparatively, precipitation events occurring on August 8 at ca. 1930h and on August 9 at ca. 1600h resulted in small but instantaneous peaks in ΔS, likely the result of direct precipitation input to the tarn surface. Peaks in GW_{in} and ΔS observed ca. 0400h on August 9, and 0030h on August 10 are also attributed to the precipitation events occurring on August 8 ca. 1930 h and August 9 ca. 1600h, respectively. Thus, the time lag between the rainfall events and the resulting peaks in GW_{in} is 8.5 h. Note that this is 3.5 h less than the lag between peak air temperature and the corresponding melt-induced peaks in GW_{in}. The reason for this difference remains unclear; however one hypothesis is that on average source if precipitation is closer to the tarn than the average source of meltwater.

The response of GW_{in} to precipitation is more clearly observed during August 24 to September 4 (Figure 3-17). The large increase in GW_{in} observed on August 30 at ca. 0800h appears to be in response to relatively small precipitation (compared to the sharp spikes in precipitation observed in Figure 3-16) between August 27 and late August 29.

Net radiation and air temperature were generally low during this period, suggesting that this peak is not influenced by a melt event. Although the rate of increase in GW_{in} beginning on August 27 is initially gradual, this rate increases at ca. 1600 h on August 29. This change in response suggests a cumulative precipitation threshold exists, below which precipitation results in a minimal increase in groundwater flow, but above which precipitation results in large increases in groundwater flow. Such thresholds are indicative of the spill-and-fill systems described in Chapter 2 and by Spence and Woo [2003] and Tromp_van Meerveld and McDonnell [2006] and likely represent the precipitation required to fill small depressions in the underlying bedrock. Filling these depressions increases the connectivity of the saturated sediments in the subsurface which results in higher groundwater flow rates [*Tromp-van Meerveld and McDonnell*, 2006]. Note the lag time between the end of the precipitation event and peak GW_{in} (ca. 8 h) is similar to that observed for the August 8 and 9 precipitation events.

3.6 Summary and Conclusions

Two independent methods were used to calculate the groundwater components of the East Tarn water balance from August 4 to 8. The first method calculated groundwater flow rates based on a full-tarn dilution experiment using a one-time injection of sodium chloride. The second method involved detailed energy balance measurements to determine the advection of energy to the tarn due to groundwater flow, from which groundwater flow rates were calculated. Although both methods showed considerable sensitivity to potential measurement errors, they produced similar results, providing confidence in the calculated values. Sensitivity analyses suggested that it is essential to

account for spatial variability when determining both average tarn temperature and average chloride concentration, as error in these values can cause considerable errors in the calculated flow rates. These methods provide a useful tool for examining groundwater-surface water interactions for small water bodies in challenging environments.

Detailed water balance calculations showed that the East Tarn acts as a flow-through pond. Between August 4 and 8 2008, calculated groundwater flow rates ranged from ca. 75 to 930 m^3d^{-1}. Thus, daily flow into and out of the tarn can be on the same order of magnitude as the volume of the tarn itself. When compared with tarn water-level, a linear equation could be used to describe the relationship between groundwater flow out of the tarn and tarn water depth, where water depth likely represents the combined effects of changes in hydraulic gradient and saturated thickness. To further test this relationship groundwater flow rates were calculated from energy balance measurements made from August 5, 6, 7, 13, 14, 16, 17, 23, and 24. Although, more scatter in the relationship existed, likely due to errors associated with the determination of the energy storage term, the relationship between GW_{out} and tarn water depth was confirmed.

Using a numerical simulation of the tarn and the calculated groundwater fluxes, hydraulic conductivity for unfrozen moraine material was estimated to range from 4.0×10^{-5} to 5.3×10^{-4} ms^{-1} with 1.9×10^{-4} m/s being a "best guess" estimate. These estimates represent the first known attempt a quantifying hydraulic conductivity for moraine material and provide an important building block for future watershed models.

A comparison of the calculated water balance between July 24 and September 4 with temperature and precipitation indicates that groundwater flow into the tarn is largely sourced from snow and/or ice melt. The lag time between peak daily radiation and peak daily groundwater flow into the tarn suggests that melt water is sourced some distance up-gradient from the tarn. Finally, there appears to be a threshold response to precipitation events, such that precipitation amounts below the threshold do not result in measurable groundwater flow, while precipitation amounts above the threshold contribute significantly to the large, deep groundwater flow system.

Date (2008) (m/d)	Energy Balance				Choride Mass Balance			
	$\Delta S(m^3)$	GW_{in} (m^3)	GW_{out} (m^3)	GW_{out}/GW_{in}	$\Delta S(m^3)$	GW_{in} (m^3)	GW_{out} (m^3)	GW_{out}/GW_{in}
8/3 15:30 to 8/4 16:00	-87.3	75.6	162.9	2.15	-87.3	209.7	296.9	1.41
8/4 16:00 to 8/5 18:30	-36.6	122.3	158.9	1.30	-36.6	72.1	108.7	1.50
8/5 18:30 to 8/6 16:50	85.0	330.3	245.3	0.74	85.0	196.6	111.5	0.56
8/6 16:50 to 8/7 17:50	185.5	663.1	477.6	0.72	185.5	428.1	242.6	0.56
8/7 17:50 to 8/8 16:30	212.4	930.8	718.3	0.77	212.4	722.8	510.4	0.70

Table 3-1. East Tarn water balance calculated by both the energy and chloride mass balance ratios. The ratios of GW_{out}/GW_{in} indicate the East Tarn is acting as a flow through lake.

Date (2008) (m/d)	Energy Balance GW_{in} (m^3)	Cl Mass Balance GW_{in} (m^3)	% difference	Energy Balance GW_{out} (m^3)	Cl Mass Balance GW_{out} (m^3)	% difference
8/3 15:30 to 8/4 16:00	75.6	209.7	63.9	162.9	296.9	44.9
8/416:00 to 8/5 18:30	122.3	72.1	-69.6	158.9	108.7	-46.7
8/5 18:30 to 8/6 16:50	330.3	196.6	-68.1	245.3	111.5	-121.0
8/6 16:50 to 8/7 17:50	663.1	428.1	-54.9	477.6	242.6	-98.1
8/7 17:50 to 8/8 16:30	930.8	722.8	-28.8	718.3	510.4	-41.1

Table 3-2. A comparison of the calculated values for GW_{in} and GW_{out} from both methods

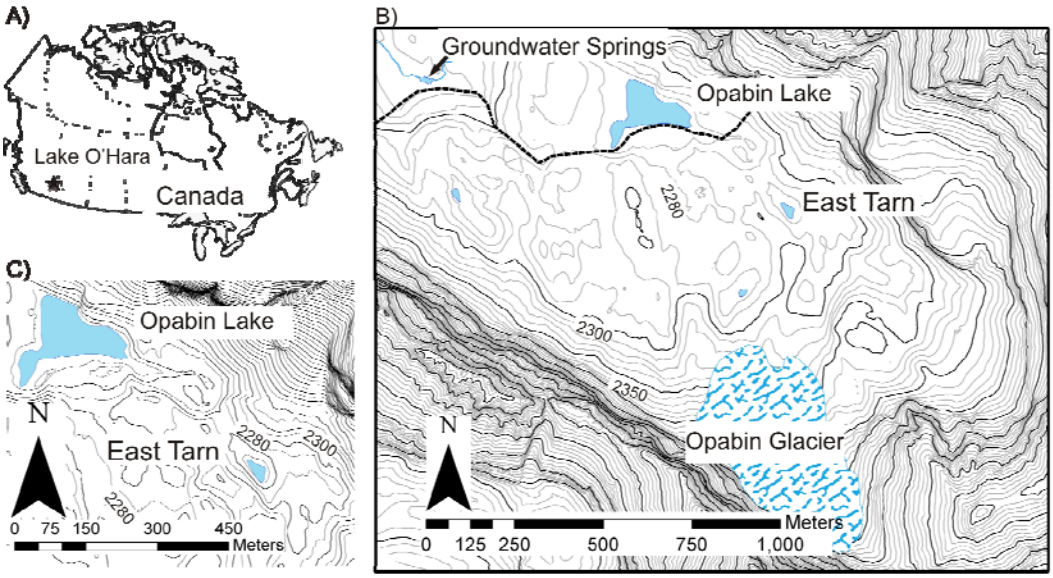

Figure 3-1. A) The location of the study site within the Canadian Rockies. B) The Opabin glacier and moraine complex including the East Tarn and a number of other surface water features. The terminus of the moraine is delineated by the thick dashed line. C) A close-up view of the East Tarn and Opabin Lake region of the moraine. Elevation is shown by 10 m contour intervals.

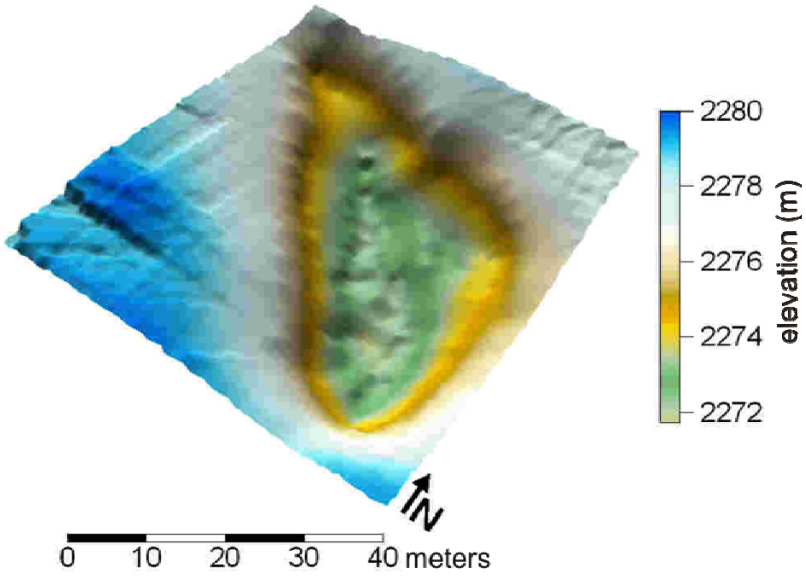
2280
2278
2276
2274
2272
elevation (m)
N
0
10
20
30
40 meters

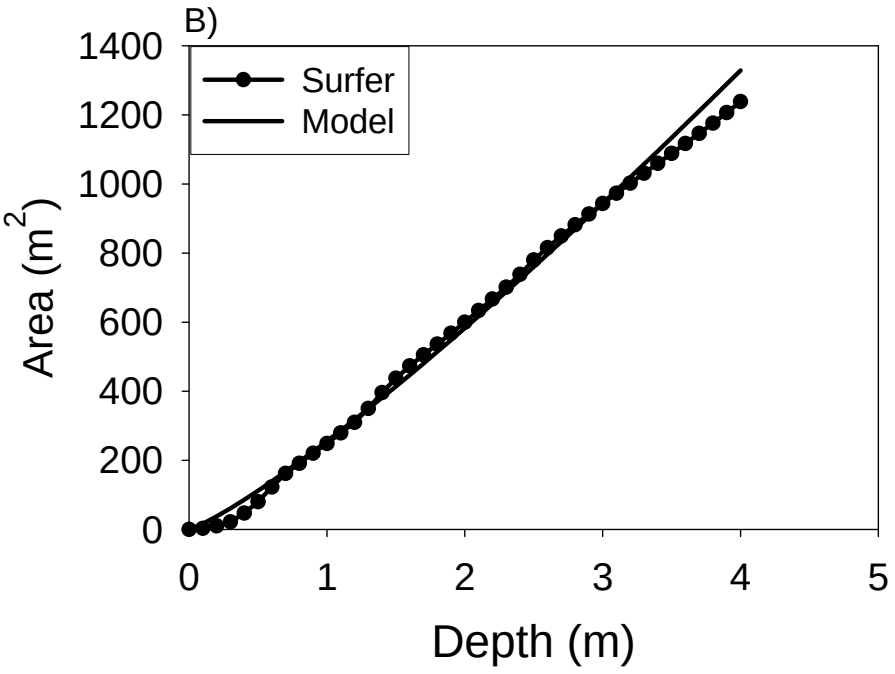
B)
Surfer
Model
Area (m2)
Depth (m)
0
200
400
600
800
1000
1200
1400
0
1
2
3
4
5

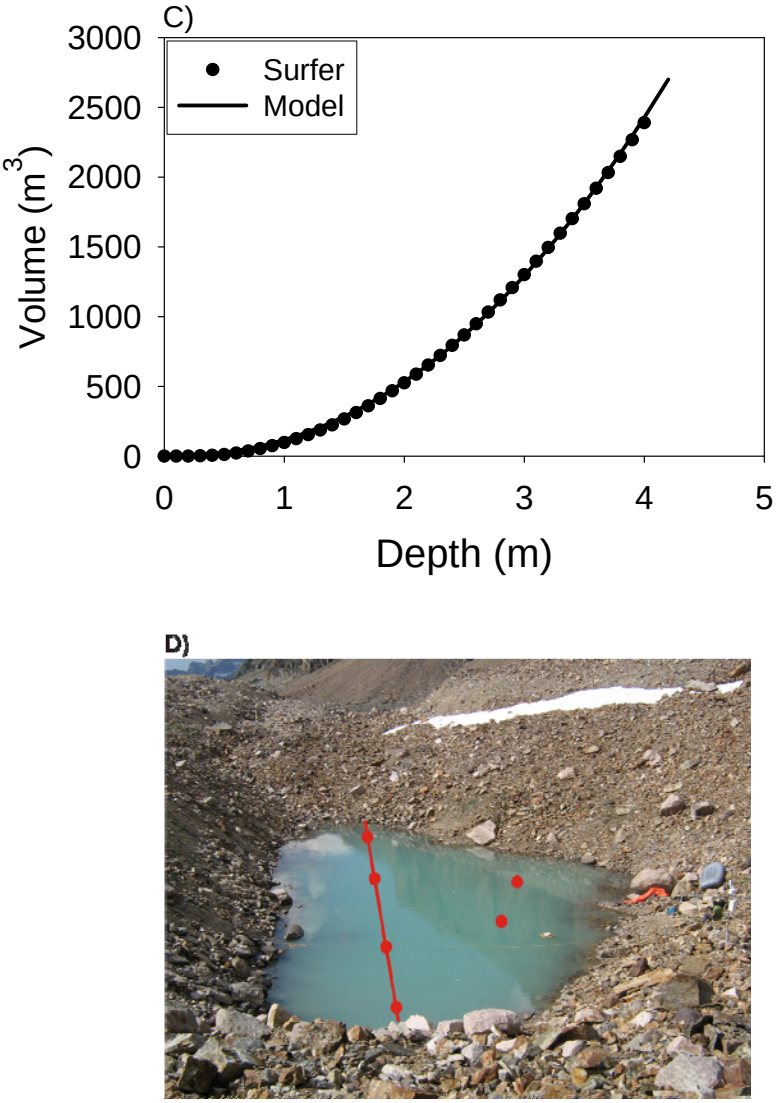

Figure 3-2. A) The digital elevation model of the tarn, and B) the depth-Area and C) depth volume relationships. Solid circles indicate data points determined using the Surfer software, while lines represent the power functions described by Hayashi and van der Kamp [2000]. A photograph of the tarn taken during the experiment shows the location of the transect surveys (red line) conducted to quantify tarn chloride concentration and average temperature and the water sampling locations (solid red circles) (D).

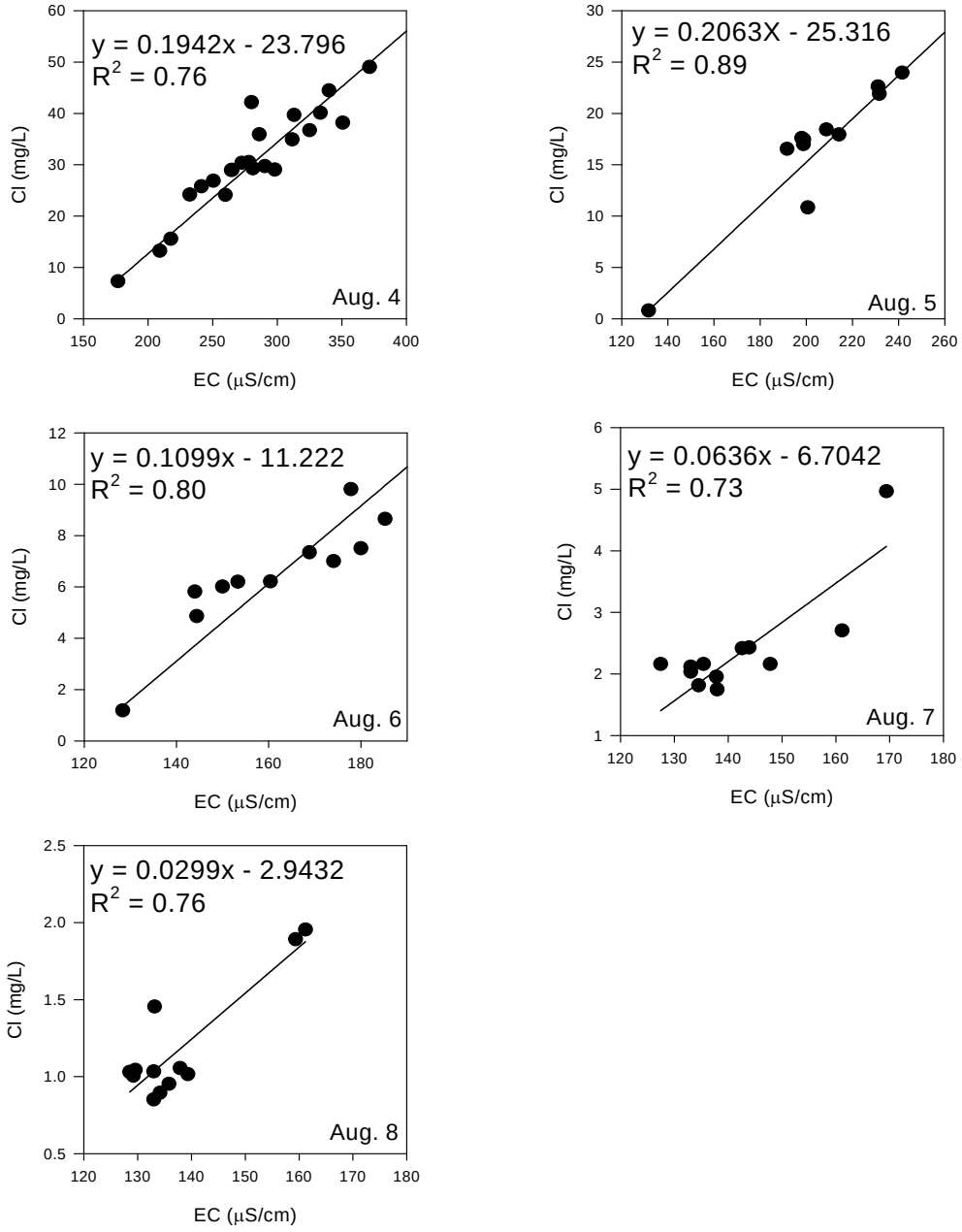

Figure 3-3. Daily empirical relationships between electrical conductivity and chloride concentration were used to determine chloride mass change and spatial distribution within the tarn.

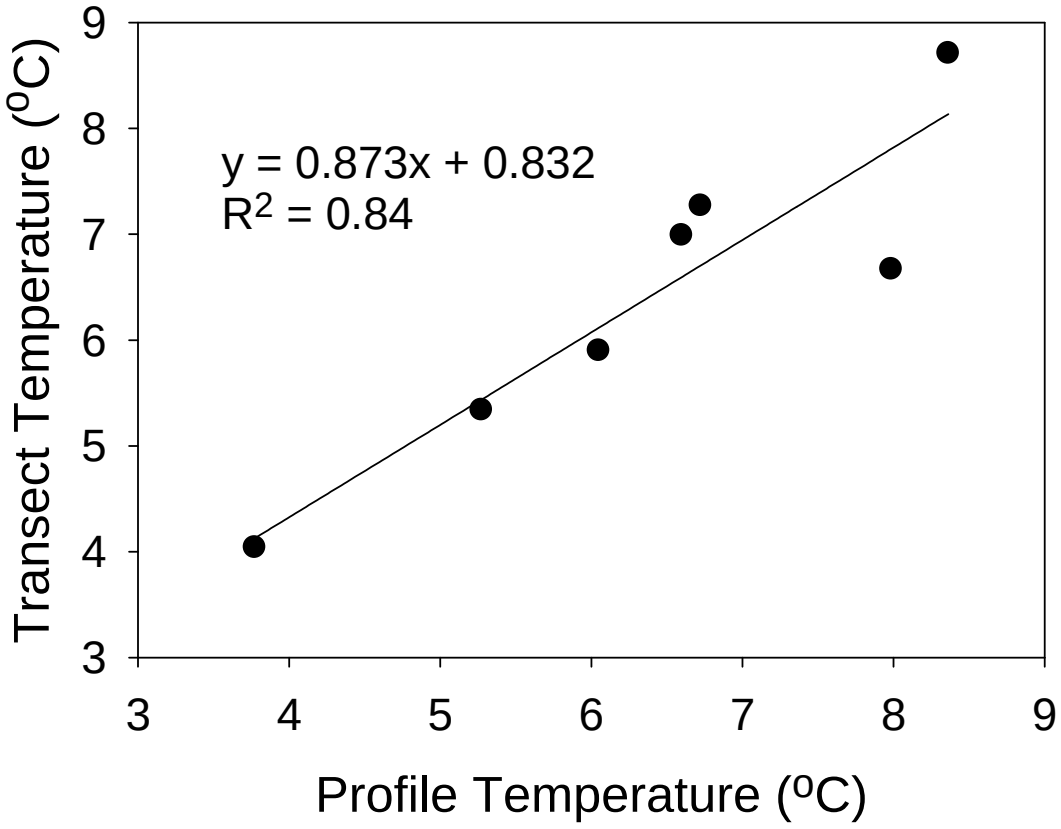

Figure 3-4. The linear relationship between the average tarn temperature measured by a vertical thermocouple profile and average tarn temperature calculated from the transect measurements. This relationship was used to correct the tarn temperatures measured by the profile so that tarn energy balance calculations could be perform for the period of August 2 to September 4. The relative RMSE of this relationship was 2.3%, indicating that this relationship accurately predicted average tarn temperature from the vertical temperature profile for August 2 to 8.

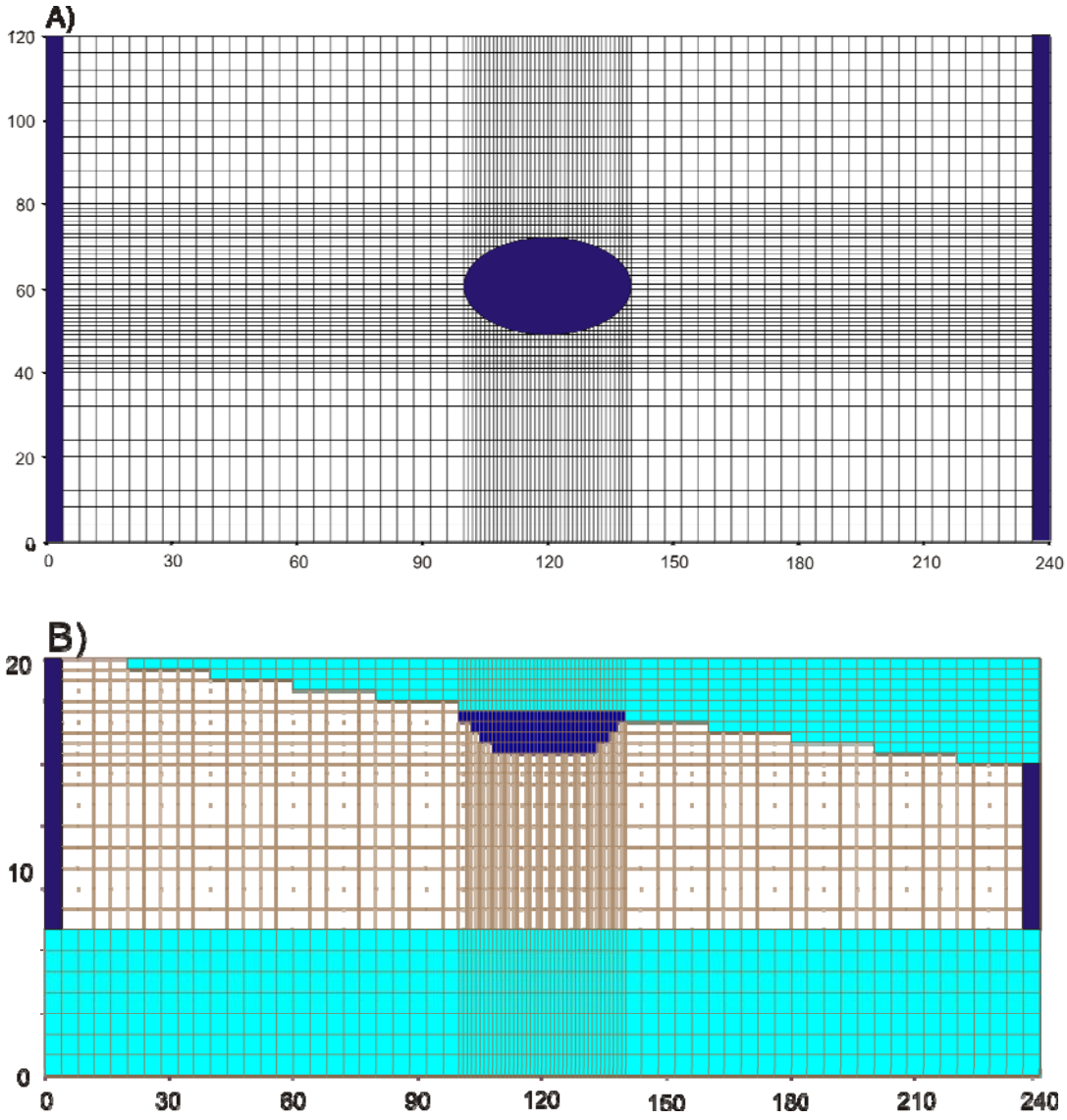

Figure 3-5. A top-down (A) and side (B) view of the mesh grid representing the model domain used to estimate hydraulic conductivity. Dark Blue regions represent constant head boundaries, where the constant head boundaries at 0 and 240 m are used to represent the regional hydraulic gradient and the region at the centre of the model domain represents the tarn. Light blue models cells are inactive (no flow boundaries), and are used to define bedrock at the bottom of the model and the water table at the top of the model.

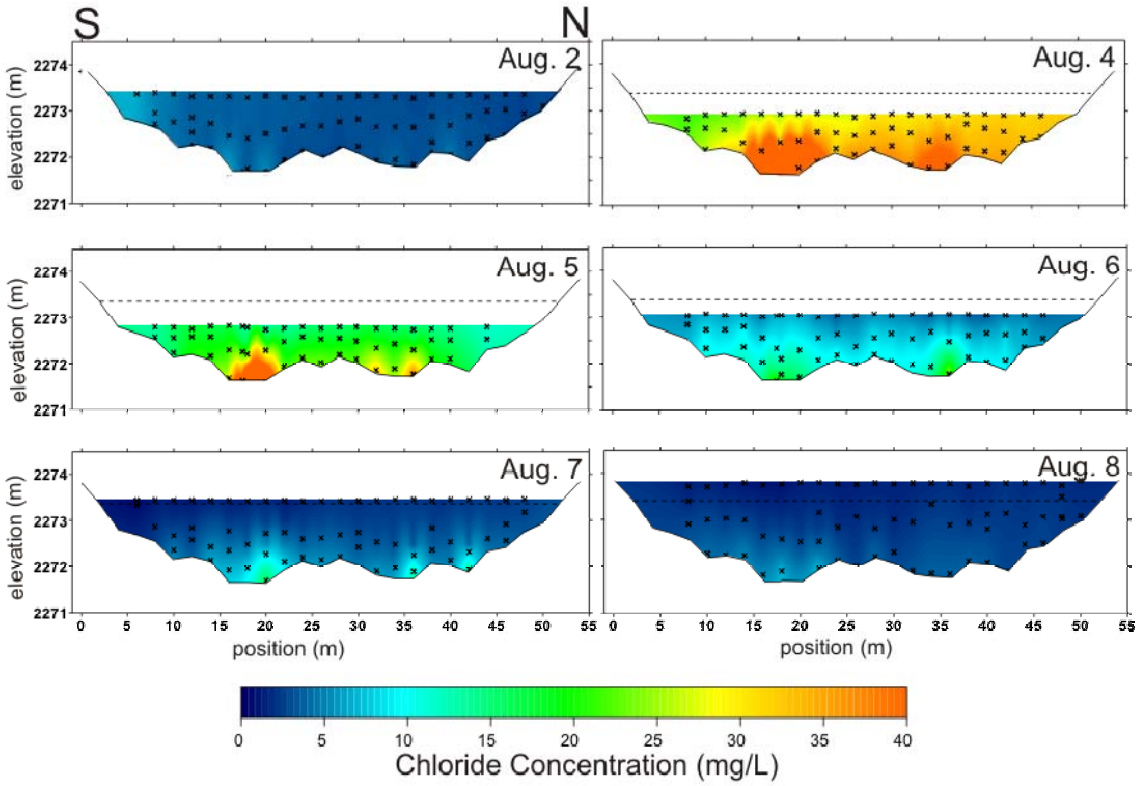

Figure 3-6. Two-dimension profiles of chloride concentration within the tarn calculated form EC measurements. The hypothesized direction of water flow is from left to right. The thick dashed line represents the water level at the start of the experiments (August 2), while the x's mark measurement locations.

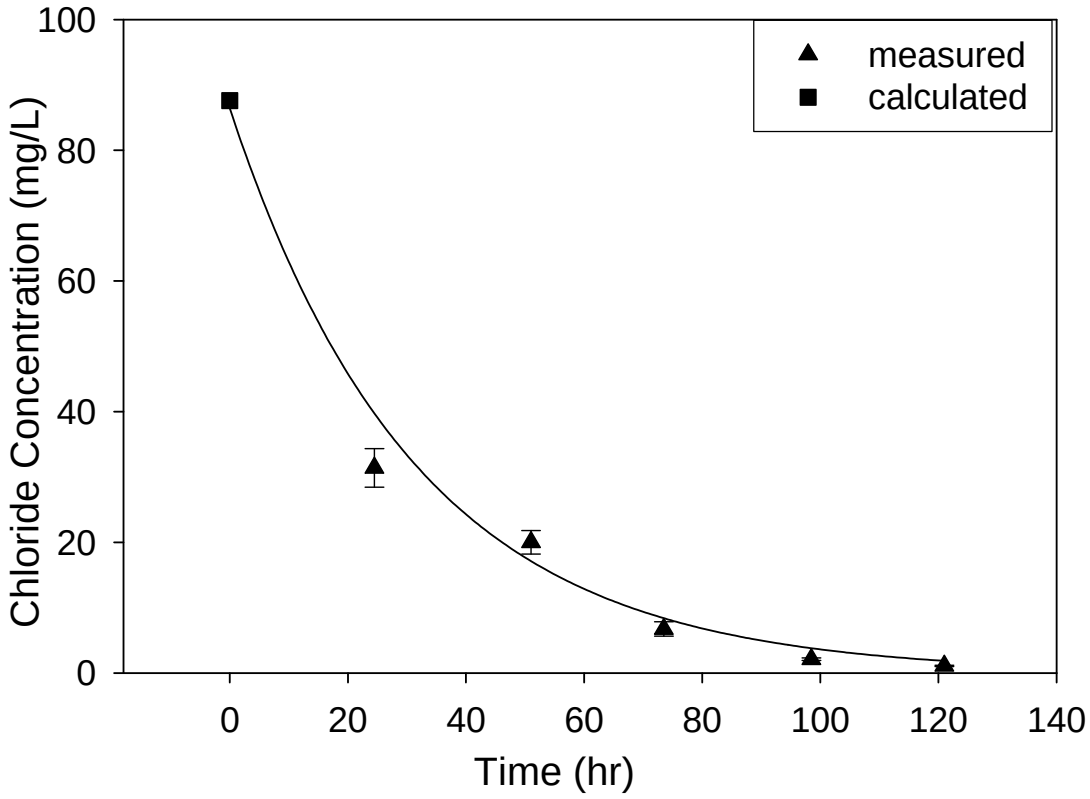

Figure 3-7. Chloride concentration in the tarn decays quickly indicating a high rate of groundwater – tarn water exchange. The chloride decay curve is represented by the solid line which is the line of best fit for the data points shown on the graph. Error bars represent the uncertainty in the calculated averages as determined from Eq. 5.

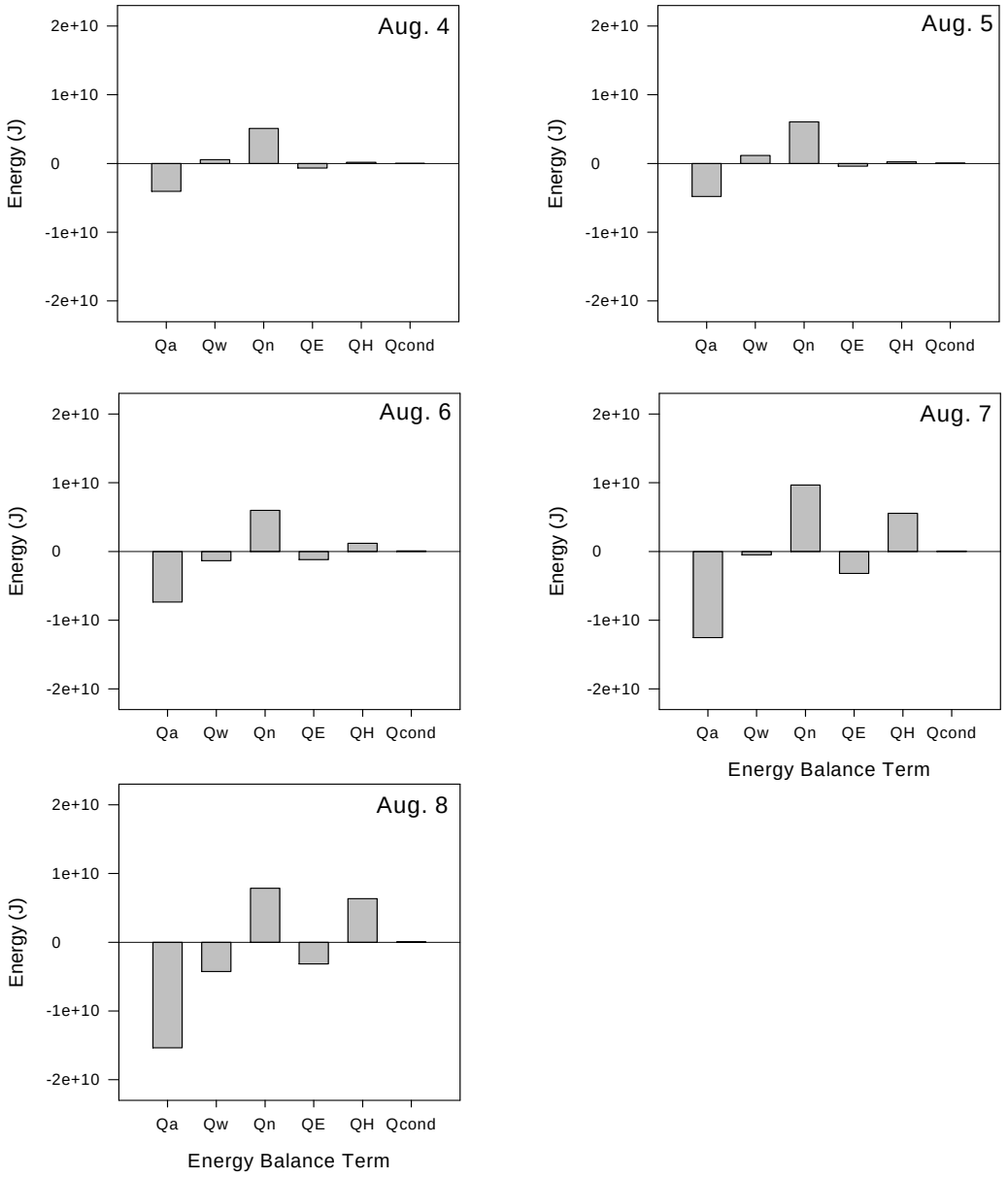

Figure 3-8. Daily energy balance for the East Tarn. The conductivity term represents only a minor component of the daily energy budget. Net radiation (Q_n) and the advection term (Q_a) are consistently large components of the energy balance, while the relative magnitude of the energy storage term (Q_w), and the latent and sensible heat fluxes (Q_E and Q_H), are more variable.

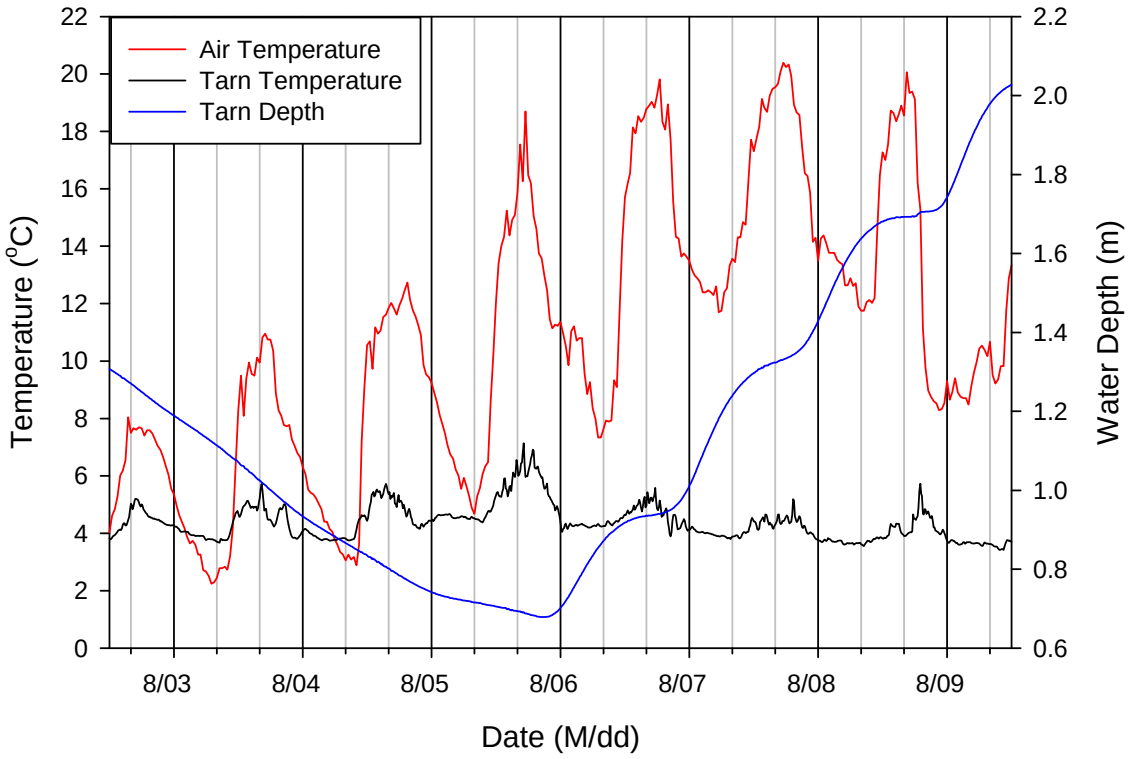

Figure 3-9. A comparison of tarn water depth, tarn water temperature and air temperature. Gridlines are spaced at 8 hour intervals. Note that while tarn water depth appears to increase in response to the high temperatures, tarn temperature decreases. This suggests groundwater temperatures are low.

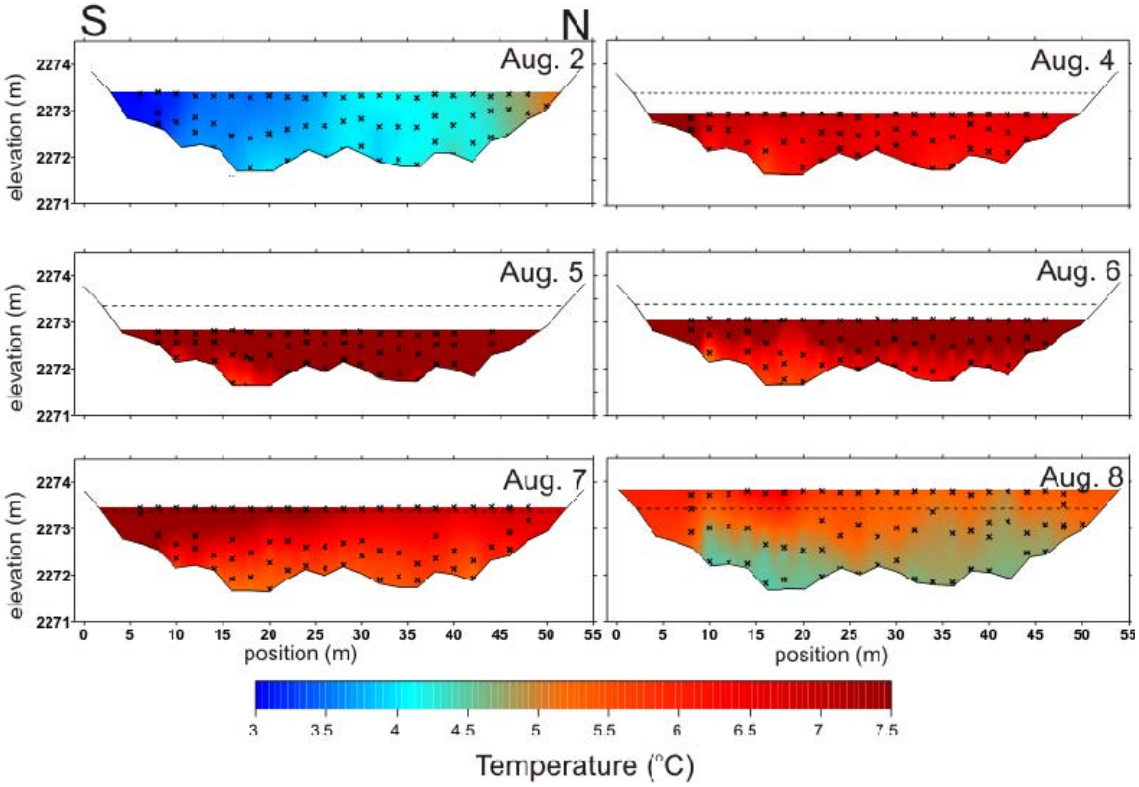

Figure 3-10. Two-dimension profiles of tarn water temperature. The hypothesized direction of water flow is from left to right. The thick dashed line represents the water level at the start of the experiments (Aug. 2), while the x's mark measurement locations.

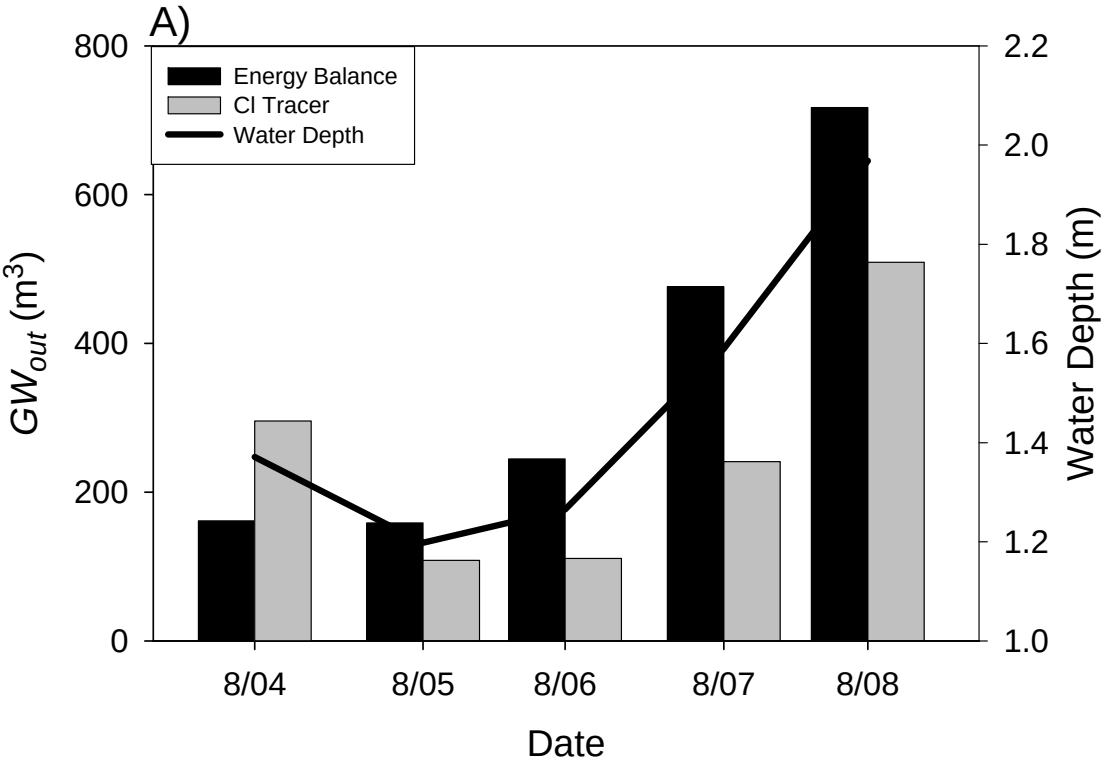
A)
Energy Balance
Cl Tracer
Water Depth
800
600
400
200
0
2.2
2.0
1.8
1.6
1.4
1.2
1.0
GW_{out} (m^3)
Water Depth (m)
8/04
8/05
8/06
8/07
8/08
Date

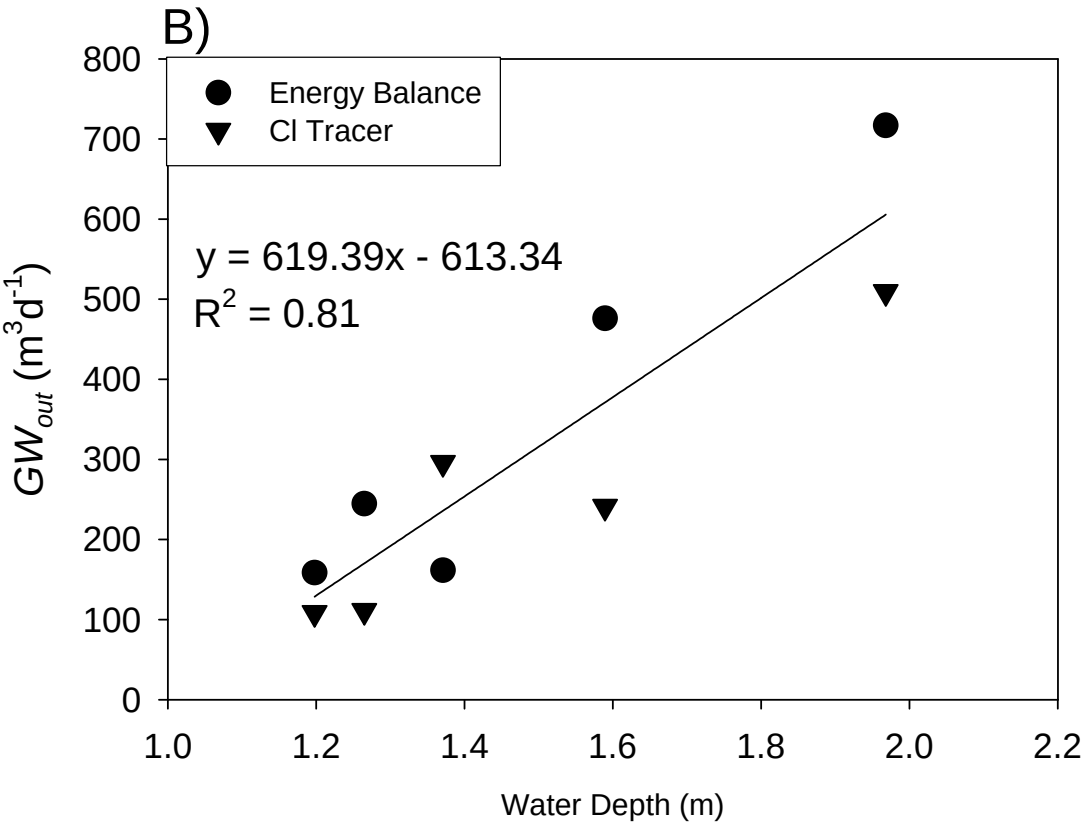

Figure 3-11. A) A comparison of GW_{out} as calculated by the energy balance and mass balance methods. Average daily tarn water depth is shown as the solid black line. B) The relationship between calculated GW_{out} and tarn water depth for August 4 to 8.

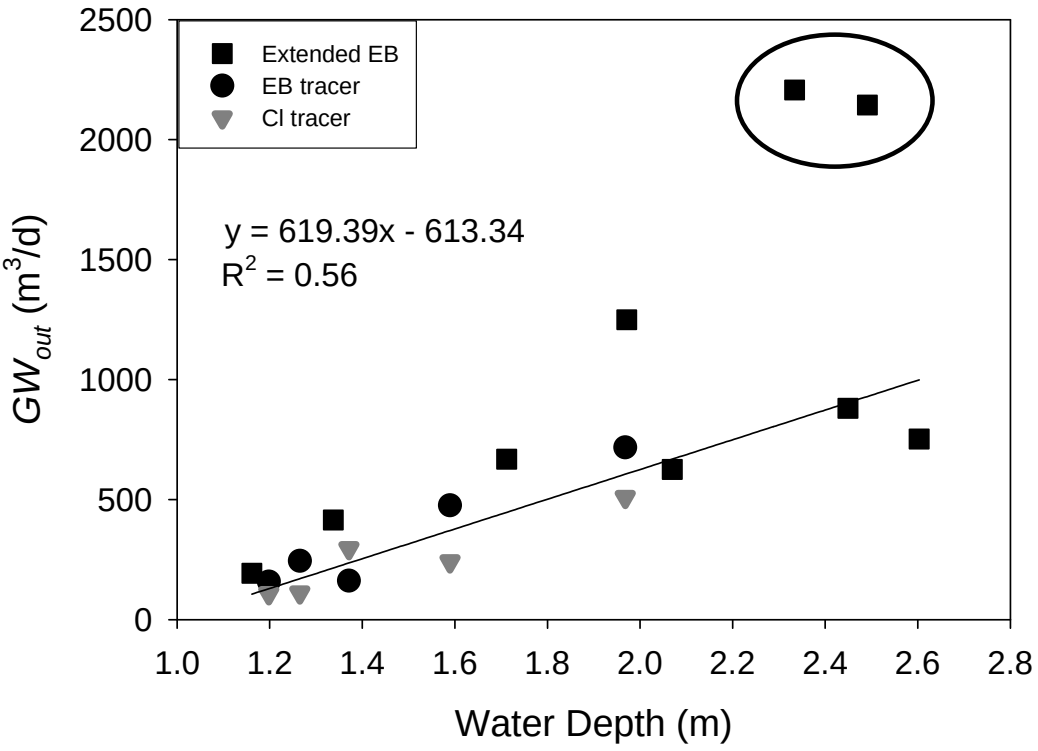

Figure 3-12. The relationship between GW_{out} and tarn water depth calculated from energy balance data for days with well constrained evaporation. Values of GW_{out} for Aug 4. to 8 calculated using the Cl mass balance and more rigorous energy balance methods are plotted for reference. The circled outlier points may be the result of poorly constrained energy storage term during these periods of high tarn depth and therefore volume.

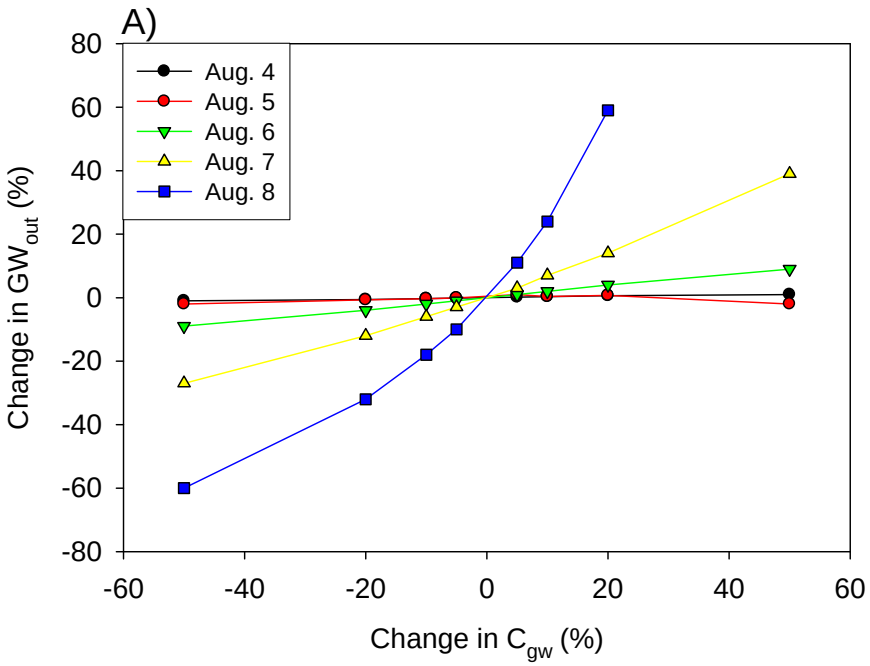
A)
Aug. 4
Aug. 5
Aug. 6
Aug. 7
Aug. 8
Change in GW$_{out}$ (%)
Change in C$_{gw}$ (%)
80
60
40
20
0
-20
-40
-60
-80
-60
-40
-20
0
20
40
60

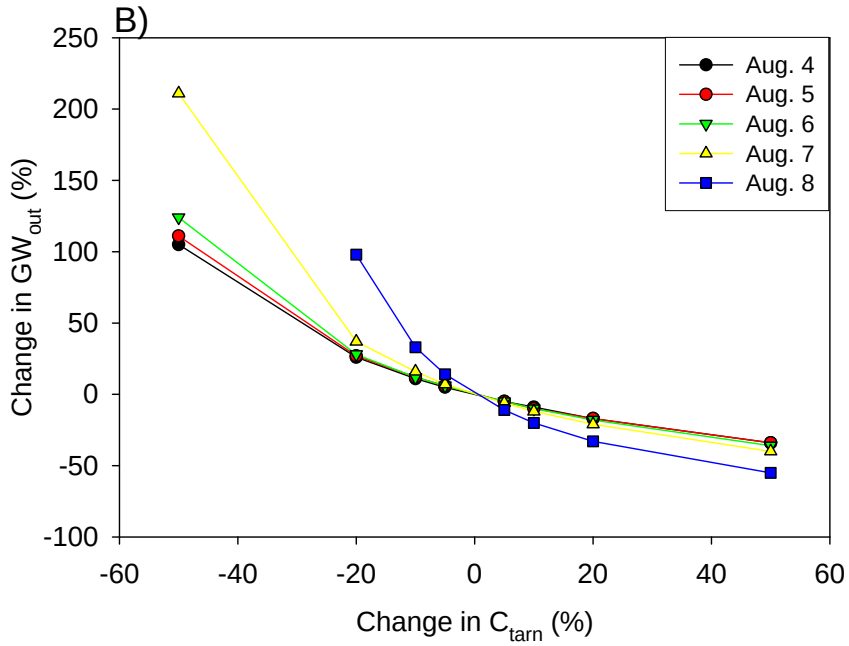
B)
Aug. 4
Aug. 5
Aug. 6
Aug. 7
Aug. 8
Change in GW$_{out}$ (%)
Change in C$_{tarn}$ (%)
250
200
150
100
50
0
-50
-100
-60
-40
-20
0
20
40
60

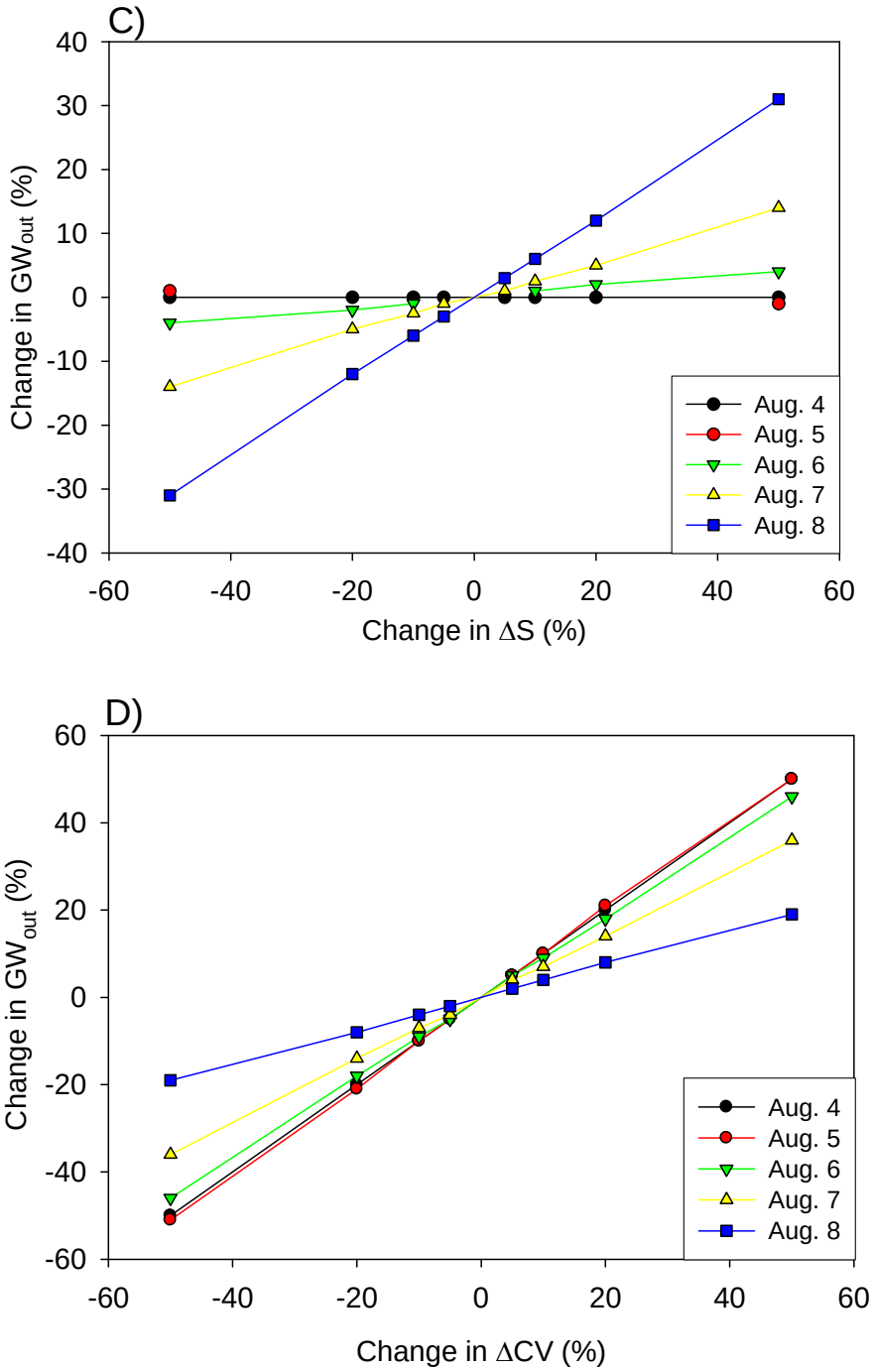

Figure 3-13. Sensitivity of GW_{out} to changes in A) groundwater chloride concentration (C_{gw}), B) tarn chloride concentration (C_{tarn}), C) tarn water storage (ΔS) and D) chloride mass (ΔCV).

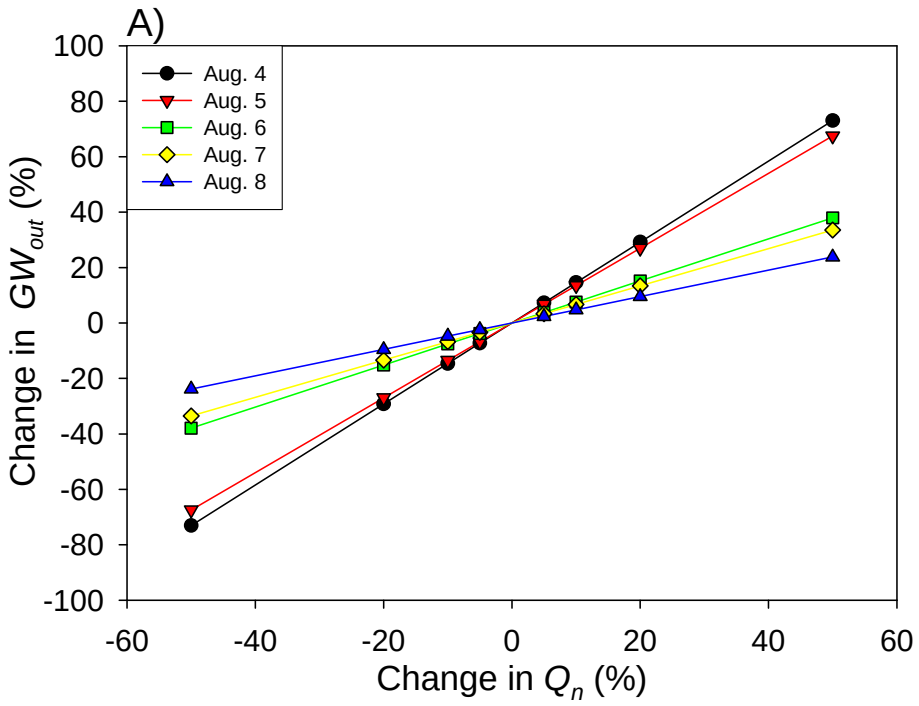
A)
Aug. 4
Aug. 5
Aug. 6
Aug. 7
Aug. 8
Change in GW_{out} (%)
Change in Q_n (%)
100
80
60
40
20
0
-20
-40
-60
-80
-100
-60
-40
-20
0
20
40
60

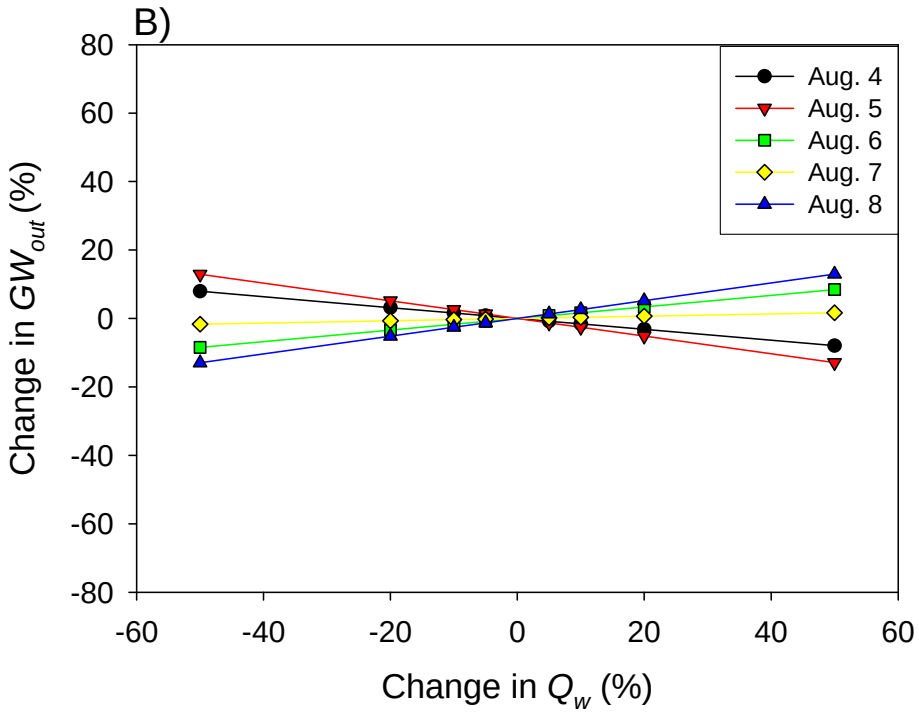
B)
Aug. 4
Aug. 5
Aug. 6
Aug. 7
Aug. 8
Change in GW_{out} (%)
Change in Q_w (%)
80
60
40
20
0
-20
-40
-60
-80
-60
-40
-20
0
20
40
60

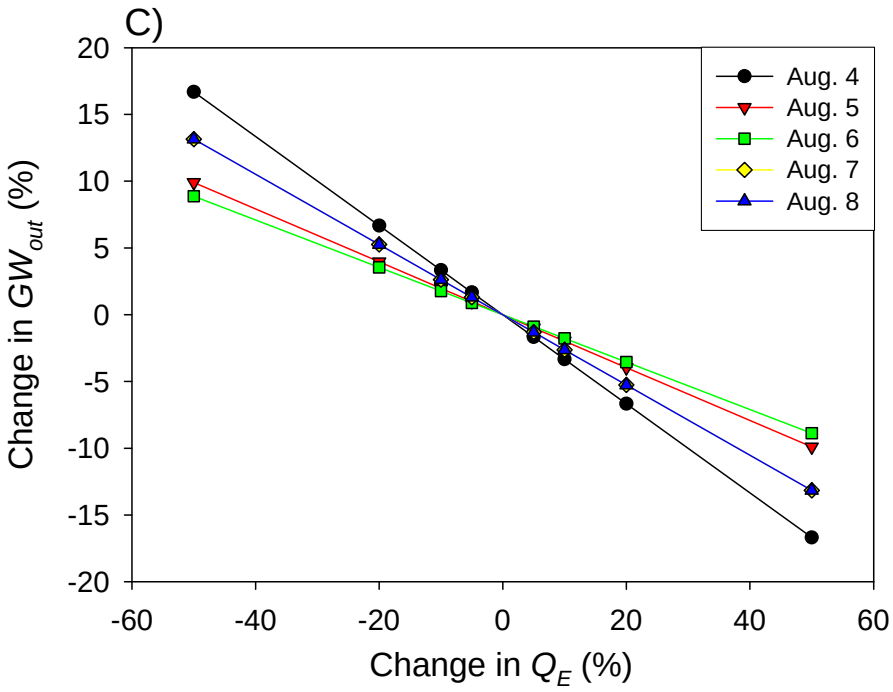
C)
Aug. 4
Aug. 5
Aug. 6
Aug. 7
Aug. 8
Change in GW_{out} (%)
Change in Q_E (%)
20
15
10
5
0
-5
-10
-15
-20
-60
-40
-20
0
20
40
60

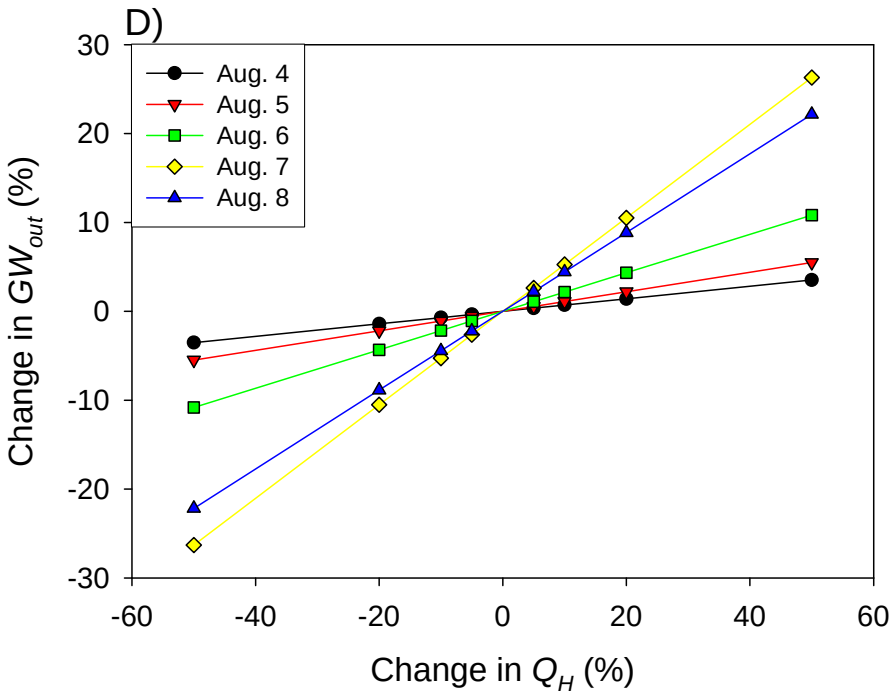
D)
Aug. 4
Aug. 5
Aug. 6
Aug. 7
Aug. 8
Change in GW_{out} (%)
Change in Q_H (%)
30
20
10
0
-10
-20
-30
-60
-40
-20
0
20
40
60

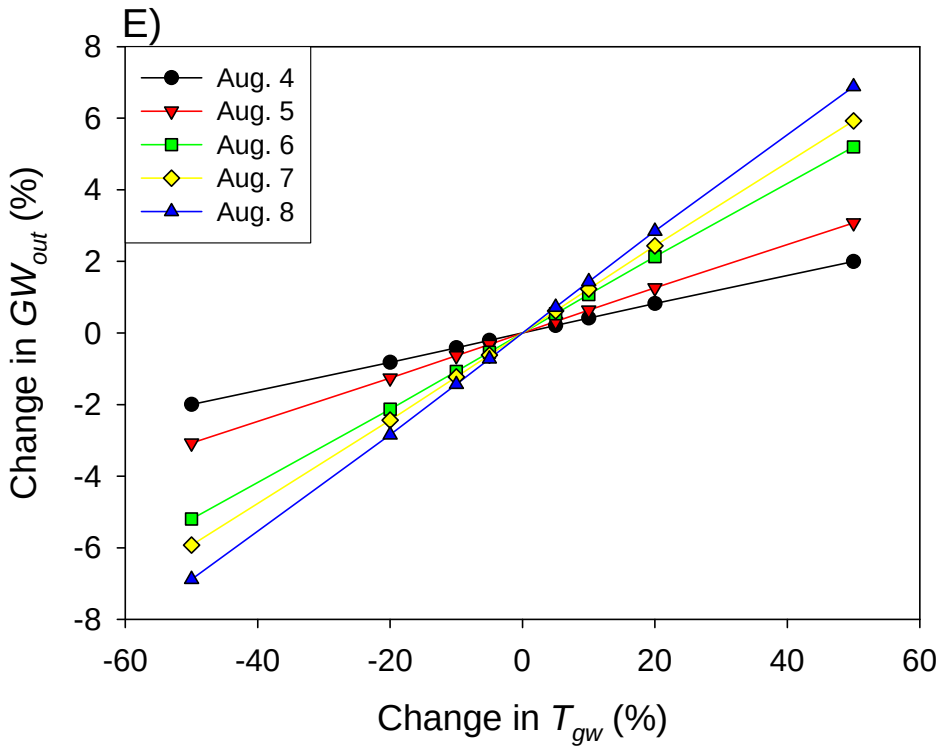

Figure 3-14. Sensitivity of GW_{out} to changes in A) net radiation, B) energy storage term, C) latent heat flux, D) sensible heat flux, E) assumed groundwater temperature.

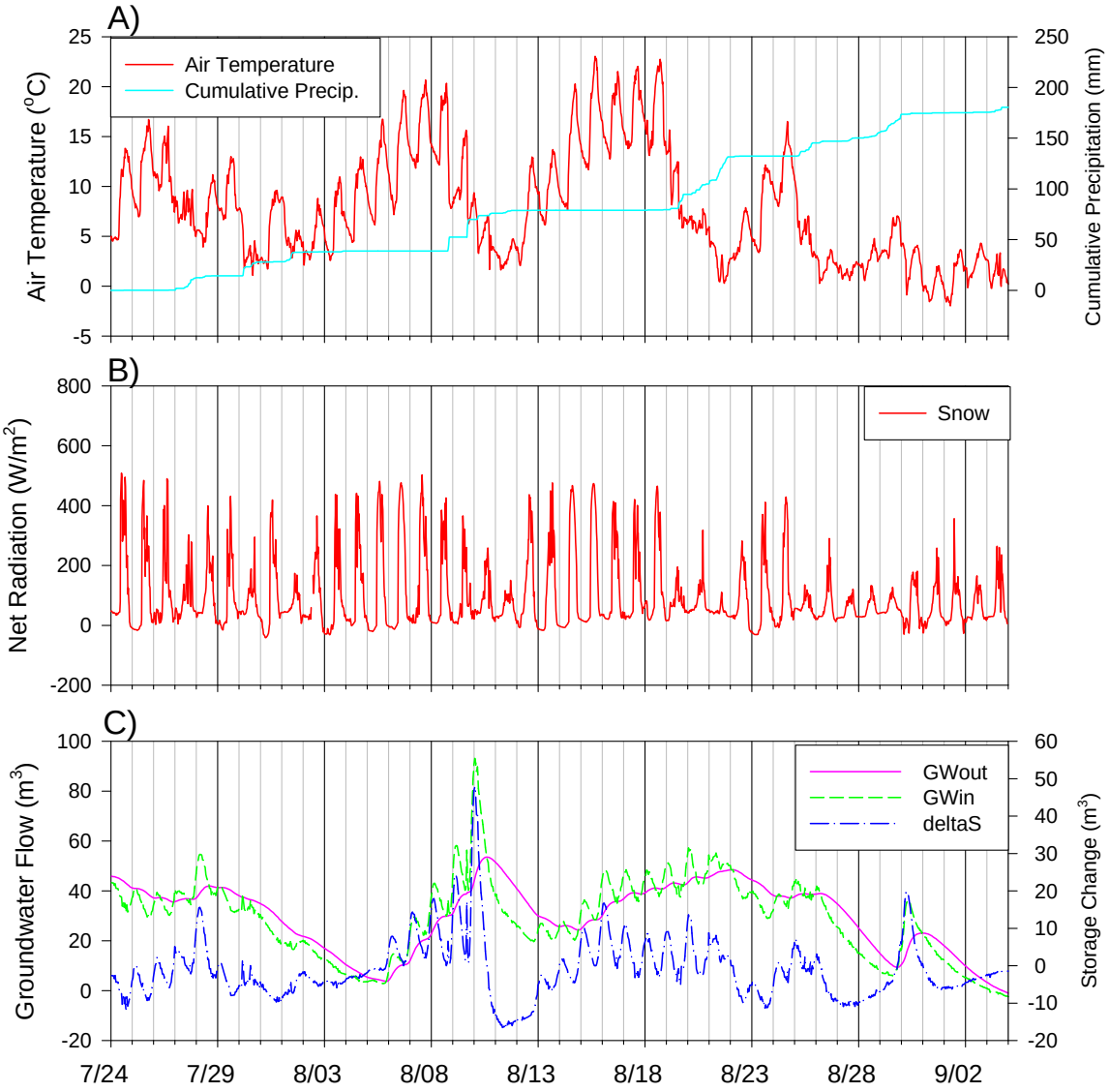

Figure 3-15. A comparison of A) air temperature and cumulative precipitation, B) net all-wave radiation for a snow surface and C) the calculated water balance of the East tarn. Note that periods of high air temperatures and radiation are followed by peak groundwater fluxes, indicating that melt events contribute significantly to groundwater flow into the tarn.

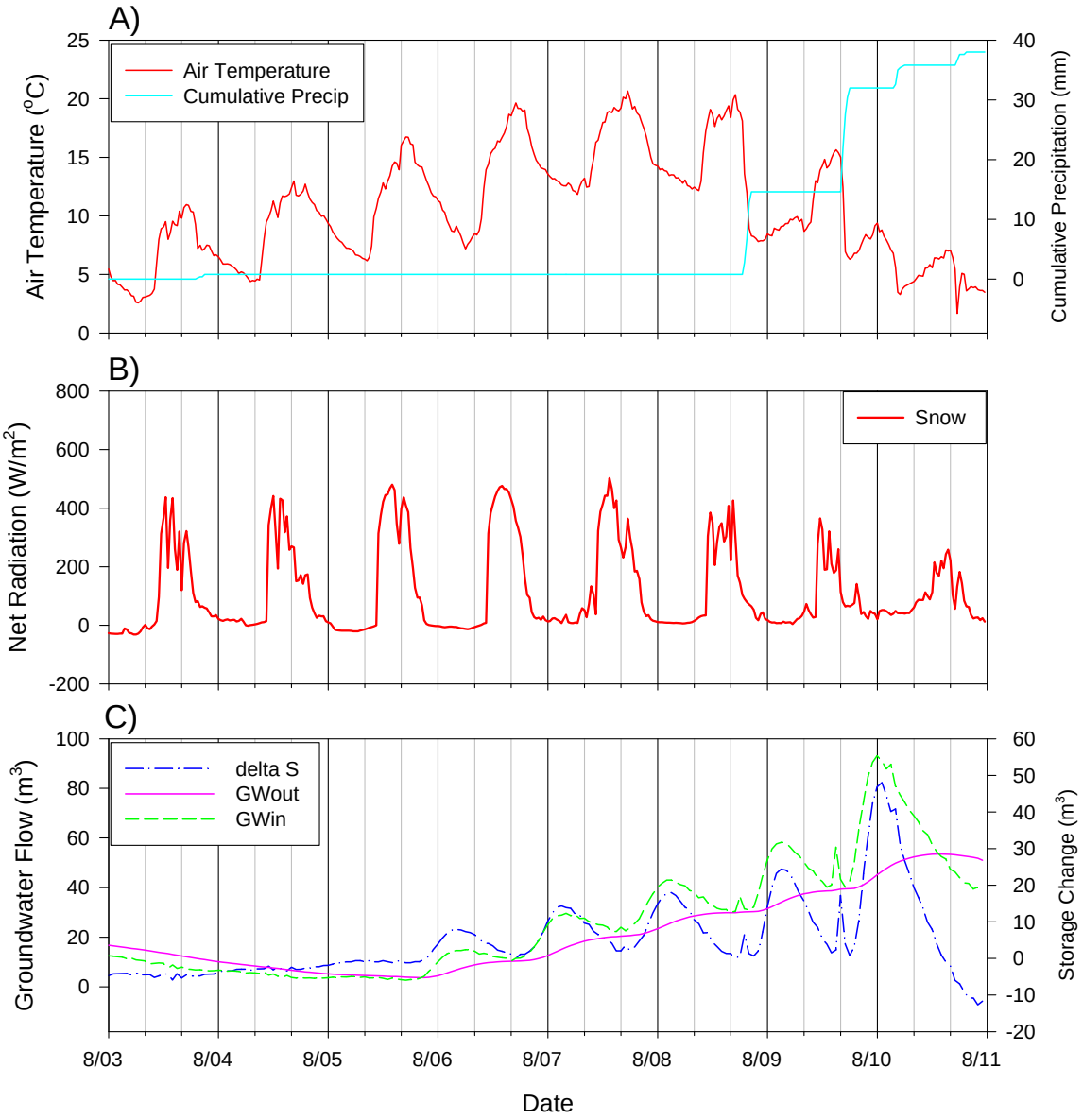

Figure 3-16. A comparison of A) air temperature and cumulative precipitation, B) net all-wave radiation for a snow surface and C) the calculated water balance of the East tarn for August 3 to 11. Peak groundwater flow into the tarn lags peak radiation by ca. 16 hours indicating that the melt water pulse must travel some distance before reaching the tarn.

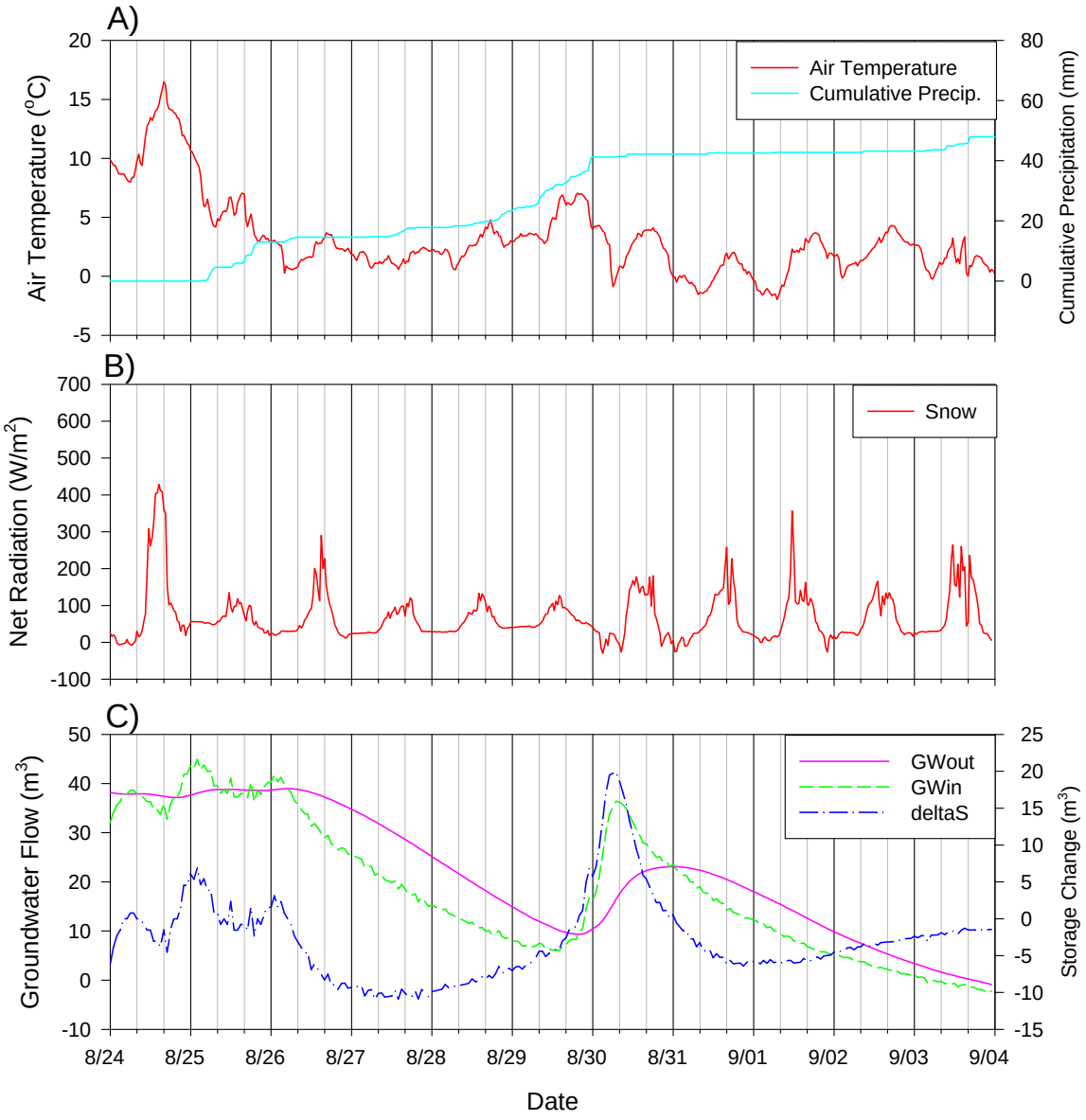

Figure 3-17 A comparison of A) air temperature and cumulative precipitation, B) net all-wave radiation for a snow surface and C) the calculated water balance of the East tarn for August 24 to September 4. Note that change in the rate of increase in GW_{in} at ca. 1600 h on August 29. This may suggest a threshold, such that precipitation amounts less than the threshold result in a minimal increase in groundwater flow, but precipitation amounts greater than the threshold result in large increases in groundwater flow.

Chapter Four: Conclusion

Understanding groundwater processes in alpine watersheds is critical to understanding the timing of water release and late-season stream flow for headwater and downstream environments. This is especially important given the expected impact of changing precipitation patterns and climate warming on stream flow. This thesis aimed to characterize and quantify the hydrological processes occurring within a partially ice-cored, proglacial moraine known to play an important hydrological role in an alpine watershed [*Roy and Hayashi*, 2008; 2009]. Specifically this thesis 1) developed a physically-based conceptual model of groundwater flow and storage for the Opabin Moraine; and 2) characterize groundwater flow through this moraine by determining the hydraulic conductivity of the moraine's primary groundwater flow path.

The conceptual model of groundwater flow through the partially ice-cored Opabin Moraine was presented in Chapter 2. Geophysical surveys specifically targeted at investigating hydrologic processes and groundwater flow paths hypothesized by previous studies [*Roy and Hayashi*, 2009] were used to define the internal structure of the conceptual model. Continuous water-level data from four water bodies connected to the moraine were analysed to show that the moraine's physical structure (e.g. massive ice vs. permafrost vs. no ice) plays an important role in hydrologic response. The conceptual model suggests the following hydrological patterns.

1) The majority of groundwater flows through a saturated layer at the bedrock-moraine interface.
2) In regions of the moraine where massive buried ice does not occur, bedrock topography likely controls the groundwater pathways.

3) Depressions in the bedrock topography may also provide a mechanism for water storage, resulting in the 'fill and spill' response seen in the hydrograph of the South Tarn located on the moraine.

4) In regions of the moraine where massive ice and permafrost occur, these features may channel flow along their impermeable boundaries and control the infiltration rate of water to the deeper groundwater flow path at the bedrock-moraine interface.

Whereas Chapter 2 contributed to the qualitative understanding of groundwater storage and transport mechanisms within the moraine, Chapter 3 sought to characterize the moraine's dominant groundwater flow path by estimating the hydraulic conductivity of ice-free moraine material. This was done by investigating the groundwater-surface water interactions of a small tarn located on the moraine (East Tarn). Groundwater flow rates into and out of the tarn were calculated using two innovative methods: 1) a full-tarn chloride dilution experiment, in which flow rates were determined from changes in the tarn chloride mass balance; and 2) detailed energy balance measurements, in which flow into the tarn was determined from the advection component of the energy balance equation. These methods represent an important contribution to groundwater investigations in challenging alpine environments by providing an alternative to conventional monitoring wells. A numerical simulation of the tarn based on the calculated groundwater fluxes was used to estimate the hydraulic conductivity of unfrozen moraine material. Continuous tarn water balance data were compared with air temperature and precipitation data to characterize the hydrologic response of the tarn to

precipitation and melt events. Combined, the analysis presented in this Chapter led to the following key findings:

1) The tarn primarily acts as a flow-through pond.
2) Daily total groundwater flow into and out of the tarn (0 to 930 m^3) was similar in magnitude to the tarn volume.
3) Groundwater flow into the tarn was largely dominated by snow and/or ice-melt.
4) The lag time between peak daily radiation and peak daily groundwater flow into the tarn suggests that melt water is sourced some distance up-gradient from the tarn.
5) There is a threshold response to precipitation events such that precipitation amounts below the threshold do not result in measurable groundwater flow, but precipitation amounts above the threshold contribute significantly to the large, deep groundwater flow system.
6) Hydraulic conductivity of the moraine material for the deep groundwater flow system ranged from 4.0×10^{-5} to 5.3×10^{-4} m s^{-1} with 1.9×10^{-4} m s^{-1} being a best guess estimate. To my knowledge, this is the first known estimate of hydraulic conductivity for a proglacial moraine.

Although previous studies have indicated that the Opabin Moraine plays an important role in groundwater storage and transport, this is the first study to examine the physical mechanisms controlling these processes. Based on the interpretation of geophysical data (Chapter 2), buried ice and permafrost topography likely controls groundwater flow and storage in the shallow subsurface., whereas bedrock topography

likely controls groundwater flow paths and provides a means for water storage at the moraine-bedrock interface. Given the apparent importance of bedrock topography in controlling groundwater flow, future studies may find that knowledge of glacier extent and flow direction (and thus glacial scouring) can provide additional clues about the locations of groundwater storage and flow pathways.

The threshold response to precipitation events observed for the South Tarn (Chapter 2) and East Tarn (Chapter 3) likely represents the water required to fill subsurface depressions in both the ice and bedrock. Such thresholds and storage mechanisms are characteristic of the spill-and-fill flow systems described by Spence and Woo (2003), and Tromp-van Meerveld and McDonnell [2006]. Future work is required to determine how this "spill-and-fill" system affects the timing of discharge from the groundwater springs at the moraine terminus, which are the primary source of water for the watershed's only outlet stream.

Watershed models will be important tools for understanding how climate change will influence alpine hydrology. Given their importance to alpine hydrology, explicit consideration of moraines as hydrological response units will improve future such models. However, accurately representing moraines will be a significant challenge, given the complex flow systems and multiple source waters. The conceptual model presented in Chapter 2 and the characteriztion of the dominant groundwater flow system in Chapter 3 provide a foundation for incorporating moraines in future modelling attempts. However, this work has also generated several important questions regarding the role of buried ice and permafrost in the hydrology of moraines, and of coarse deposits in general. The following questions will require further study if future watershed models seek to

incorporate ice-cored moraines and test hypotheses regarding long-term changes to alpine hydrology:

1) Since ice and permafrost structures within the moraine are likely dynamic (e.g. melting), how will changes to buried ice and permafrost structures affect moraine storage capacity? And on what timescales will these changes occur
2) How much water is stored within moraines as buried ice and permafrost and at what rate are these features melting?
3) Is melt water from buried ice a significant water balance component?

To answer these questions it is will be essential to develop a method for delineating buried ice and permafrost within moraines and to determine what controls the extent and melt of buried ice and permafrost. A preliminary calculation based on crude assumptions suggests that the amount of water stored as buried ice within the moraine is similar in magnitude to that stored in the Opabin Glacier (see Appendix C). Given the extensive attention paid to the role of glaciers in sustaining summer baseflow of alpine streams [*Hock et al.*, 2008; *Milner et al.*, 2009; *Moore and Demuth*, 2001; *Moore et al.*, 2009], this further highlights the need to recognize ice-cored and partially-ice cored coarse deposits as significant hydrological response units.

Although buried ice and permafrost may play an important role in groundwater storage and shallow subsurface flow, geophysical surveys (Chapter 2) and hydrological analysis (Chapters 2 and 3) indicate that the moraine's dominant groundwater flow system is a saturated layer at the bedrock-moraine interface. Furthermore, both Chapter 2 and 3 show that large increases in East Tarn water level correspond with periods of high air temperature and net radiation suggesting that groundwater flow through the saturated

layer is largely sourced from snow and/or glacier melt. Thus, changes in snow and glacier depth and extent, such as those predicted under current climate change scenarios [*Bales et al.*, 2006; *Barnett et al.*, 2005; *Dettinger and Cayan*, 1995; *Stewart et al.*, 2004], may significantly change the volume and timing of groundwater flow through the moraine and subsequently the watershed.

Finally, this work focuses on a single moraine in the Canadian Rockies. Future work is needed to determine if this moraine is representative of others in the Rockies and other regions of the world. This thesis provides both a useful tool-set for investigating these complex hydrological features and a reference point for comparing results

References

Anderson, M. P. (2005), Heat as a ground water tracer, *Ground Water*, *43*(6), 951-968.

Bales, R. C., N. P. Molotch, T. H. Painter, M. D. Dettinger, R. Rice, and J. Dozier (2006), Mountain hydrology of the western United States, *Water Resources Research*, *42*(8).

Bandyopadhyay, J., D. Kraemer, a. R. Kattelmann, and Z. W. Kundzewicz (1997), Highland waters: A resource of global significance, in *Mountains of the World: A Global Priority*, edited by B. M. a. J. Ives, pp. 131-155, Parthenon, New York.

Barnett, T. P., J. C. Adam, and D. P. Lettenmaier (2005), Potential impacts of a warming climate on water availability in snow-dominated regions, *Nature*, *438*(7066), 303-309.

Barsch, D. (1971), Rock Glaciers and Ice-Cored Moraines, *Geografiska Annaler*, *53*(3/4), 203-206.

Bonnaventure, P. P., and A. G. Lewkowicz (2008), Mountain permafrost probability mapping using the BTS method in two climatically dissimilar locations, northwest Canada, *Canadian Journal of Earth Sciences*, *45*(4), 443-455.

Born, S. M., S. A. Smith, and D. A. Stephenson (1979), Hydrogeology of glacial-terrain lakes, with management and planning applications, *Journal of Hydrology*, *43*(1-4), 7-43.

Brenning, A. (2005), Geomorphological, hydrological and climatic significance of rock glaciers in the Andes of Central Chile (33-35 degrees S), *Permafrost and Periglacial Processes*, *16*(3), 231-240.

Brown, L. E., D. M. Hannah, A. M. Milner, C. Soulsby, A. J. Hodson, and M. J. Brewer (2006), Water source dynamics in a glacierized alpine river basin (Taillon-Gabietous, French Pyrenees), *Water Resources Research*, *42*(8).

Campbell, D. H., D. W. Clow, G. P. Ingersoll, M. A. Mast, N. E. Spahr, and J. T. Turk. (1995), Processes controlling the chemistry of two snowmelt-dominated streams in the Rocky Mountains, *Water Resources Research*, *31*(11), 11.

Clark, S. A., C. A. Zelt, M. B. Magnani, and A. Levander (2008), Characterizing the Caribbean-South American plate boundary at 64 degrees W using wide-angle seismic data, *Journal of Geophysical Research-Solid Earth*, *113*(B7).

Clow, D. W., L. Schrott, R. Webb, D. H. Campbell, A. Torizzo, and M. Dornblaser (2003), Ground water occurrence and contributions to streamflow in an alpine catchment, Colorado Front Range, *Ground Water*, *41*(7), 14.

Cogley, J. G. (1979), Albedo of water as a function of latitude, *Monthly Weather Review*, *107*(6), 775-781.

Conant, B. (2004), Delineating and quantifying ground water discharge zones using streambed temperatures, *Ground Water*, *42*(2), 243-257.

Constantz, J. (2008), Heat as a tracer to determine streambed water exchanges, *Water Resources Research*, *44*.

Cote, J., and J. M. Konrad (2005), Thermal conductivity of base-course materials, *Canadian Geotechnical Journal*, *42*(1), 61-78.

Cressie, N. A. C. (1991), *Statistics for Spatial Data*, 900 pp., John Wiley and Sons Inc., New York.

Croce, F. A., and J. P. Milana (2002), Internal structure and behaviour of a rock glacier in the arid Andes of Argentina, *Permafrost and Periglacial Processes*, *13*(4), 289-299.

Dettinger, M. D., and D. R. Cayan (1995), Large-scale atmospheric forcing of recent trends towards early snowmelt runoff in California, *Journal of Climate*, *8*(3), 606-623.

Dingman, S. L. (2002), *Physical Hydrology*, Prentice Hall, Upper Saddle River, New Jersey.

Driscoll, F. G. (1980), Wastage of the Klutlan ice-cored moraines, Yukon Territory, Canada, *Quarernary Research*, *14*, 19.

Driscoll, F. G. (1984), Reply to Comments by John Pickard Regarding "Wastage of the Klutlan Ice-Cored Moraines, Yukon Territory, Canada", *Quarernary Research*, *22*, 260-261.

Elo, P. A. R. (2007), The energy balance and vertical thermal structure of two small boreal lakes in summer, *Boreal Environ. Res.*, *12*(5), 585-600.

Evin, M., D. Fabre, and P. G. Johnson (1997), Electrical resistivity measurements on the rock glaciers of Grizzly Creek, St Elias Mountains, Yukon, *Permafrost and Periglacial Processes*, *8*(2), 181-191.

Gardner, L. E. M. a. J. S. (1991), Mass Wasting on Valley-Side Ice-Cored Moraines, Boundary Glacier, Alberta, Canada, *Geografiska Annaler*, *73*(3/4), 6.

Genereux, D. (1998), Quantifying uncertainty in tracer-based hydrograph separations, *Water Resour. Res.*, *34*.

Gross, R., A. G. Green, H. Horstmeyer, and J. H. Begg (2004), Location and geometry of the Wellington Fault (New Zealand) defined by detailed three-dimensional georadar data, *Journal of Geophysical Research-Solid Earth*, *109*(B5).

Gurrieri, J. T., and G. Furniss (2004), Estimation of groundwater exchange in alpine lakes using non-steady mass-balance methods, *Journal of Hydrology*, *297*(1-4), 187-208.

Hammer, O., Harper, D.A.T., Ryan, P.D., (2006), PAST – Paleontological Statistics, Ver. 1.51.

Hatch, C. E., A. T. Fisher, J. S. Revenaugh, J. Constantz, and C. Ruehl (2006), Quantifying surface water-groundwater interactions using time series analysis of streambed thermal records: Method development, *Water Resources Research*, *42*(10).

Hauck, C., and D. Vonder Muhll (2003), Inversion and interpretation of two-dimensional geoelectrical measurements for detecting permafrost in mountainous regions, *Permafrost and Periglacial Processes*, *14*(4), 305-318.

Hauck, C., D. Vonder Muhll, and H. Maurer (2003), Using DC resistivity tomography to detect and characterize mountain permafrost, *Geophysical Prospecting*, *51*(4), 273-284.

Hauck, C., K. Isaksen, D. V. Muhll, and J. L. Sollid (2004), Geophysical surveys designed to delineate the altitudinal limit of mountain permafrost: An example from Jotunheimen, Norway.

Hauck, C., and C. Kneisel (2008), *Applied Geophysics in Periglacial Environments*, Cambridge University Press, Cambridge.

Hausmann, H., K. Krainer, E. Bruckl, and W. Mostler (2007), Internal structure and ice content of Reichenkar rock glacier (Stubai alps, Austria) assessed by geophysical investigations, *Permafrost and Periglacial Processes*, *18*(4), 351-367.

Hayashi, M., and G. van der Kamp (2000), Simple equations to represent the volume-area-depth relations of shallow wetlands in small topographic depressions, *Journal of Hydrology*, *237*(1-2), 74-85.

Hayashi, M. (2004), Temperature-electrical conductivity relation of water for environmental monitoring and geophysical data inversion, *Environmental Monitoring and Assessment*, *96*(1-3), 119-128.

Hilbich, C., L. Marescot, C. Hauck, M. H. Loke, and R. Mausbacher (2009), Applicability of electrical resistivity tomography monitoring to coarse blocky and ice-rich permafrost landforms, *Permafrost and Periglacial Processes*, *20*(3), 269-284.

Hock, R., G. Flowers, and T. Johannesson (2008), Glaciers in watershed and global hydrology Preface, *Hydrological Processes*, *22*(19), 3887-3887.

Hoelzle, M., M. Wegmann, and B. Krummenacher (1999), Miniature temperature dataloggers for mapping and monitoring of permafrost in high mountain areas: First experience from the Swiss Alps, *Permafrost and Periglacial Processes*, *10*(2), 113-124.

Hood, J. L., J. W. Roy, and M. Hayashi (2006), Importance of groundwater in the water balance of an alpine headwater lake, *Geophysical Research Letters*, *33*(13).

Ikeda, A. (2006), Combination of conventional geophysical methods for sounding the composition of rock glaciers in the Swiss Alps, *Permafrost and Periglacial Processes*, *17*(1), 35-48.

Intergovernmental Panel on Climate Change (IPCC). (2007), Climate Change 2007: Synthesis report - summary for policy makers, New York.

Jansen, F., and S. Hergarten (2006), Rock glacier dynamics: Stick-slip motion coupled to hydrology, *Geophys. Res. Lett.*, *33*.

Johnson, P. G. (1981), The structure of a talus-derived rock glacier deduced from its hydrology *Canadian Journal of Earth Sciences*, *18*(9), 1422-1430.

Kalbus, E., F. Reinstorf, and M. Schirmer (2006), Measuring methods for groundwater - surface water interactions: a review, *Hydrol. Earth Syst. Sci.*, *10*(6), 873-887.

Kneisel, C. (2004), New insights into mountain permafrost occurrence and characteristics in glacier forefields at high altitude through the application of 2D resistivity imaging.

Kneisel, C. (2006), Assessment of subsurface lithology in mountain environments using 2D resistivity imaging.

Krainer, K., and W. Mostler (2002), Hydrology of active rock glaciers: Examples from the Austrian Alps, *Arctic Antarctic and Alpine Research*, *34*(2), 142-149.

LaBaugh, J. W., T. C. Winter, D. O. Rosenberry, P. F. Schuster, M. M. Reddy, and G. R. Aiken (1997), Hydrological and chemical estimates of the water balance of a closed-basin lake in north central Minnesota, *Water Resources Research*, *33*(12), 2799-2812.

Lanz, E., H. Maurer, and A. G. Green (1998), Refraction tomography over a buried waste disposal site, *Geophysics*, *63*, 1414-1433.

Lewkowicz, A. G., and M. Ednie (2004), Probability mapping of mountain permafrost using the BTS method, Wolf Creek, Yukon Territory, Canada, *Permafrost and Periglacial Processes*, *15*(1), 67-80.

Lickorish, W. H., and P. S. Simony (1995), Evidence for late rifting of the cordilleran margin outlined by stratigraphic division of the Lower Cambrian Gog Group, Rocky-Mountain Main Ranges, British-Columbia and Alberta, *Canadian Journal of Earth Sciences*, *32*(7), 860-874.

Liu, F. J., M. W. Williams, and N. Caine (2004), Source waters and flow paths in an alpine catchment, Colorado Front Range, United States, *Water Resources Research*, *40*(9).

Loke, M. H., and R. D. Barker (1996), Rapid least-squares inversion of apparent resistivity pseudosections by a quasi-Newton method, *Geophysical Prospecting*, *44*(1), 131-152.

Marescot, L., M. H. Loke, D. Chapellier, D. R., C. Lambiel, and E. Reynard (2003), Assessing reliability of 2D resistivity imaging in mountian permafrost studies using the depth of investigation index method, *Near Surface Geophysics*, *1*, 57-67.

Maurer, H., and C. Hauck (2007), Instruments and methods - Geophysical imaging of alpine rock glaciers, *Journal of Glaciology*, *53*(180), 110-120.

Meybeck, M., P. Green, and C. Vorosmarty (2001), A new typology for mountains and other relief classes: An application to global continental water resources and population distribution, *Mountain Research and Development*, *21*(1), 34-45.

Milner, A. M., L. E. Brown, and D. M. Hannah (2009), Hydroecological response of river systems to shrinking glaciers, *Hydrological Processes*, *23*(1), 62-77.

Moore, R. D., and M. N. Demuth (2001), Mass balance and streamflow variability at Place Glacier, Canada, in relation to recent climate fluctuations.

Moore, R. D., S. W. Fleming, B. Menounos, R. Wheate, A. Fountain, K. Stahl, K. Holm, and M. Jakob (2009), Glacier change in western North America: influences on hydrology, geomorphic hazards and water quality, *Hydrological Processes*, *23*(1), 42-61.

Musil, M., H. Maurer, A. G. Green, H. Horstmeyer, F. O. Nitsche, D. Vonder Muhll, and S. Springman (2002), Shallow seismic surveying of an Alpine rock glacier, *Geophysics*, *67*(6), 1701-1710.

Musil, M., H. Maurer, K. Hollinger, and A. G. Green (2006), Internal structure of an alpine rock glacier based on crosshole georadar traveltimes and amplitudes, *Geophysical Prospecting*, *54*(3), 273-285.

Nield, S. P., L. R. Townley, and A. D. Barr (1994), A framework for quantitative analysis of surface water-groundwater interaction - flow geometry in a vertical section, *Water Resources Research*, *30*(8), 2461-2475.

Oke, T. R. (1988), *Boundary Layer Climates*, 2 ed., Routledge, New York.

Oldenburg, D. W., and Y. G. Li (1999), Estimating depth of investigation in dc resistivity and IP surveys, *Geophysics*, *64*(2), 403-416.

Østrem, G. (1959), Ice melting under a thin layer of moraine, and the existence of ice cover in moriane covers in moraine ridges, *Geografiska Annaler*, *41*, 228-230.

Østrem, G., and K. Arnold (1970), Ice-cored moraines in Southern British Columbia and Alberta, Canada, *Geografiska Annaler. Series A, Physical Geography*, *52*(2), 120-128.

Østrem, G. (1971), Rock glaciers and ice-cored moraines, a reply to D. Barsch, *Geografiska Annaler*, *53*(3/4), 207-213.

Parsons, D. F., M. Hayashi, and G. van der Kamp (2004), Infiltration and solute transport under a seasonal wetland: bromide tracer experiments in Saskatoon, Canada, *Hydrological Processes*, *18*(11), 2011-2027.

Paterson, W. S. B. (1999), *The Physics of Glaciers*, Third ed., Butterworth-Heinemann, Oxford.

Pickard, J. (1984), Comment on "Wastage of the Klutlan Ice-Cored Moraines, Yukon Territory, Canada" by Driscoll (1980), *QUATERNARY RESEARCH*, *22*, 1.

Pidlisecky, A., and R. Knight (2008), FW2_5D: A MATLAB 2.5-D electrical resistivity modeling code, *Computers & Geosciences*, *34*(12), 1645-1654.

Price, R., D. Cook, J. Aitken, and E. Mountjoy (1980), Geology, Lake Louise, Alberta and British Columbia, Geological Survey of Canada, Ottawa.

Reynolds, J. M. (1997), *An Introduction to Applied and Environmental Geophysics*, New York.

Rodriguez-Rodriguez, M., E. Moreno-Ostos, I. De Vicente, L. Cruz-Pizarro, and S. L. R. Da Silva (2004), Thermal structure and energy budget in a small high mountain lake: La Caldera, Sierra Nevada, Spain, *New Zealand Journal of Marine and Freshwater Research*, *38*(5), 879-894.

Rodriguez-Rodriguez, M., and E. Moreno-Ostos (2006), Heat budget, energy storage and hydrological regime in a coastal lagoon, *Limnologica*, *36*(4), 217-227.

Ronnert, L., and D. M. Mickelson (1992), High porosity of basal till at Burroughs Glacier, Southeastern Alaska *Geology*, *20*(9), 849-852.

Rood, S. B., J. Pan, K. M. Gill, C. G. Franks, G. M. Samuelson, and A. Shepherd (2008), Declining summer flows of Rocky Mountain rivers: Changing seasonal hydrology and probable impacts on floodplain forests, *Journal of Hydrology*, *349*(3-4), 397-410.

Rouse, W. R., P. D. Blanken, N. Bussieres, C. J. Oswald, W. M. Schertzer, C. Spence, and A. E. Walker (2008), Investigation of the Thermal and Energy Balance Regimes of Great Slave and Great Bear Lakes, *J. Hydrometeorol.*, *9*(6), 1318-1333.

Roy, J. W., and M. Hayashi (2008), Groundwater exchange with two small alpine lakes in the Canadian Rockies.

Roy, J. W., and M. Hayashi (2009), Multiple, distinct groundwater flow systems of a single moraine-talus feature in an alpine watershed, *Journal of Hydrology*, *373*(1-2), 139-150.

Roy, J. W., M. Hayashi, and D. Muir (in review), Small-scale spatial variability of groundwater spring properties in an alpine watershed, *Arctic Antarctic and Alpine Research*.

Sass, O. (2006), Determination of the internal structure of alpine talus deposits using different geophysical methods (Lechtaler Alps, Austria), *Geomorphology*, *80*(1-2), 45-58.

Schmidt, C., B. Conant, M. Bayer-Raich, and M. Schirmer (2007), Evaluation and field-scale application of an analytical method to quantify groundwater discharge using mapped streambed temperatures, *Journal of Hydrology*, *347*(3-4), 292-307.

Schrott, L. (1996), Some geomorphological-hydrological aspects of rock glaciers in the Andes (San Juan, Argentina), *Zeitschrift fur Geomorphologie*, *Supplementband 104*, 13.

Siegel, D. (2008), Reductionist hydrogeology: ten fundamental principles, *Hydrological Processes*, *22*(25), 4967-4970.

Spence, C., and M.-k. Woo (2003), Hydrology of subarctic Canadian shield: soil-filled valleys, *Journal of Hydrology*, *279*(1-4), 151-166.

Stewart, I. T., D. R. Cayan, and M. D. Dettinger (2004), Changes in snowmelt runoff timing in western North America under a 'business as usual' climate change scenario, *Climatic Change*, *62*(1-3), 217-232.

Tague, C., and G. E. Grant (2009), Groundwater dynamics mediate low-flow response to global warming in snow-dominated alpine regions, *Water Resources Research*, *45*.

Tenthorey, G. (1992), Perennial neves and the hydrology of rock glaciers, *Permafrost and Periglacial Processes*, *3*, 6.

Townley, L. R., and M. G. Trefry (2000), Surface water-groundwater interaction near shallow circular lakes: Flow geometry in three dimensions, *Water Resources Research*, *36*(4), 935-948.

Tromp-van Meerveld, H. J., and J. J. McDonnell (2006), Threshold relations in subsurface stormflow: 2. The fill and spill hypothesis, *Water Resour. Res.*, *42*.

Viviroli, D., R. Weingartner, and B. Messerli (2003), Assessing the hydrological significance of the world's mountains, *Mountain Research and Development*, *23*(1), 32-40.

Viviroli, D., H. H. Durr, B. Messerli, M. Meybeck, and R. Weingartner (2007), Mountains of the world, water towers for humanity: Typology, mapping, and global significance, *Water Resources Research*, *43*(7).

Vonder Muhll, D., C. Hauck, H. Gubler, R. McDonald, and N. Russill (2001), New geophysical methods of investigating the nature and distribution of mountain permafrost with special reference to radiometry techniques, *Permafrost and Periglacial Processes*, *12*(1), 27-38.

Vonder Muhll, D., C. Hauck, and H. Gubler (2002), Mapping of mountain permafrost using geophysical methods, *Progress in Physical Geography*, *26*(4), 643-660.

Williams, M. W., M. Knauf, N. Caine, F. Liu, and P. L. Verplanck (2006), Geochemistry and source waters of rock glacier outflow, Colorado Front Range, *Permafrost and Periglacial Processes*, *17*(1), 13-33.

Winter, T. C. Numerical simulation of steady state three-dimensional groundwater flow near lakes, *Water Resour. Res.*, *14*.

Yilmaz, O. (2001), *Seismic Data Processing*, 2027 pp., Society of Exlporation Geophysics, Tulsa, Oklahoma.

Zlotnik, V. A., F. Olaguera, and J. B. Ong (2009), An approach to assessment of flow regimes of groundwater-dominated lakes in arid environments, *Journal of Hydrology*, *371*(1-4), 22-30.

APPENDIX A: ELECTRICAL RESISTIVITY IMAGING DEPTH OF INVESTIGATION ANALYSES

Introduction

Electrical resistivity surveys have been effectively used in several mountain-permafrost studies. However, difficult mountainous terrain imposes special challenges to the collection of high-quality data. Specifically, the contact resistance between electrodes and the ground surface is often large, which may inhibit current flow into the ground. In some locations it may not be possible to plant an electrode, in which case the electrode must be relocated to the nearest possible location out of line with others in the survey. Furthermore, topographic variations are often dramatic and may introduce errors related to the geometric correction of the data. Finally, the large contrasts between unfrozen and frozen ground can further complicate data interpretation. For example, an extremely resistive layer (e.g. ice) above a low resistivity layer (e.g. water-saturated sediments), can prevent sufficient current from reaching the lower layer to produce accurate data. Consequently, careful analysis of data quality and culling of poor data is necessary to ensure that data is not misinterpreted. In addition to culling highly variable data as described in the Methods section of Chapter 1, the reliability of inverted data may be assessed by depth of investigation (DOI) analysis. This was done as described below to provide an indication of the uncertainty in electrical resistivity values presented by the resistivity models in Chapter 2.

Methods

Depth of investigation analysis involves performing two inversions of the same data using different values of the initial reference resistivity (starting model) [*Marescot et al.*, 2003]. The following equation is used to calculate the DOI value of a model cell *($R_{AB}(x,y)$)*:

$$R_{AB}(x,y) = \frac{q_A(x,y) - q_B(x,y)}{q_A - q_B} \qquad \text{(1-A1)}$$

where q_A is the geometric mean of the apparent resistivity data for the first reference model, q_B is the geometric mean of the apparent resistivity data for the second reference model, $q_A(x,y)$ and $q_B(x,y)$ are the apparent resistivity values for model block x,y of the corresponding inversion models

The value of R approaches zero for model blocks where the two inversions generate the same resistivity value [*Marescot et al.*, 2003]. Regions where the resulting models are similar (R values < 0.1) indicate that this part of the model is well constrained by the data. Regions where the models differ significantly (residuals R > 0.1) suggest a poorly constrain region of the model. Poorly constrained regions must be interpreted with more caution. A detailed description of the method used here can be found in Marescot et al. [2003].

The commercially available inversion software RES2DINV (Geotomo Software) was used to perform the DOI analysis. Marescot et al. [2003] noted that using a robust constraint for the inversion process can cause difficulties in computing DOI values. Consequently, although I used a robust constraint to generate the inversion models interpreted in Chapter 2, a least squares constraint was used to assess the DOI index for

the surveys. This resulted in minor differences in the inverted image, but still provides a reasonable indication of which model regions are well constrained and which are not. Initial reference models were selected as 0.1 and 10 times geometric mean of the observed apparent resistivity data. The data were then inverted using the default parameters provided by RES2DINV, which coincide with the values used by [*Marescot et al.*, 2003]. Contours of the DOI values were then overlain on an inversion model that used a starting reference model equal to the average of the logarithm of the measured resistivity data.

Results and Discussion

The results of the DOI analysis for each of the resistivity lines interpreted in Chapter 2 are shown in Figure A1a to d. Contours represent the DOI values as calculated from Eq. 1 (0.1 intervals). In general the inversion models appear well constrained in the upper portion of the images (i.e. the upper portion of the moraine), but much less well-constrained in the lower regions. Regions of lower resistivity underlying regions high resistivity appear particularly poorly constrained (e.g. the low resistivity layer in Figure A1b beginning at ca. 2260 m.a.s.l.). It is important to note that the poorly constrained aspects of the models are resistivity values, and not the trends in resistivity. For example, although the model of ERI line 2 is poorly constrained below the resistive layer regardless of the starting model used, the resistivity trend (high to low resistivity) remains the same. Thus, despite the actual resistivity values being poorly constrained, the boundary represented by the transition from high to low resistivity (ca. 2260 m.a.s.l.; Figure A1b) is likely data driven, rather than an artifact of the model. Accordingly,

interpretations in Chapter 2 were primarily based on large-scale resistivity boundaries and changes, rather than minor changes in actual resistivity values.

References

Marescot, L., et al. (2003), Assessing reliability of 2D resistivity imaging in mountian permafrost studies using the depth of investigation index method, *Near Surface Geophysics*, *1*, 57-67.

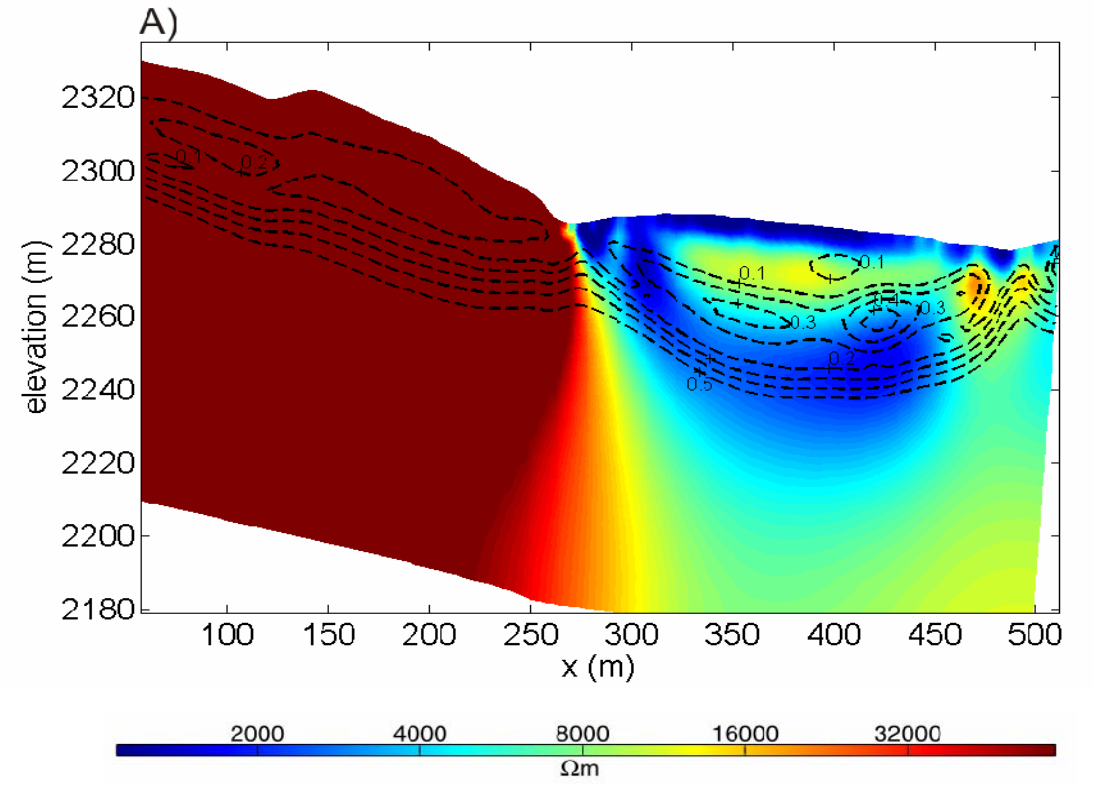
A)
elevation (m)
2320
2300
2280
2260
2240
2220
2200
2180
100
150
200
250
300
350
400
450
500
x (m)
2000
4000
8000
16000
32000
Ωm

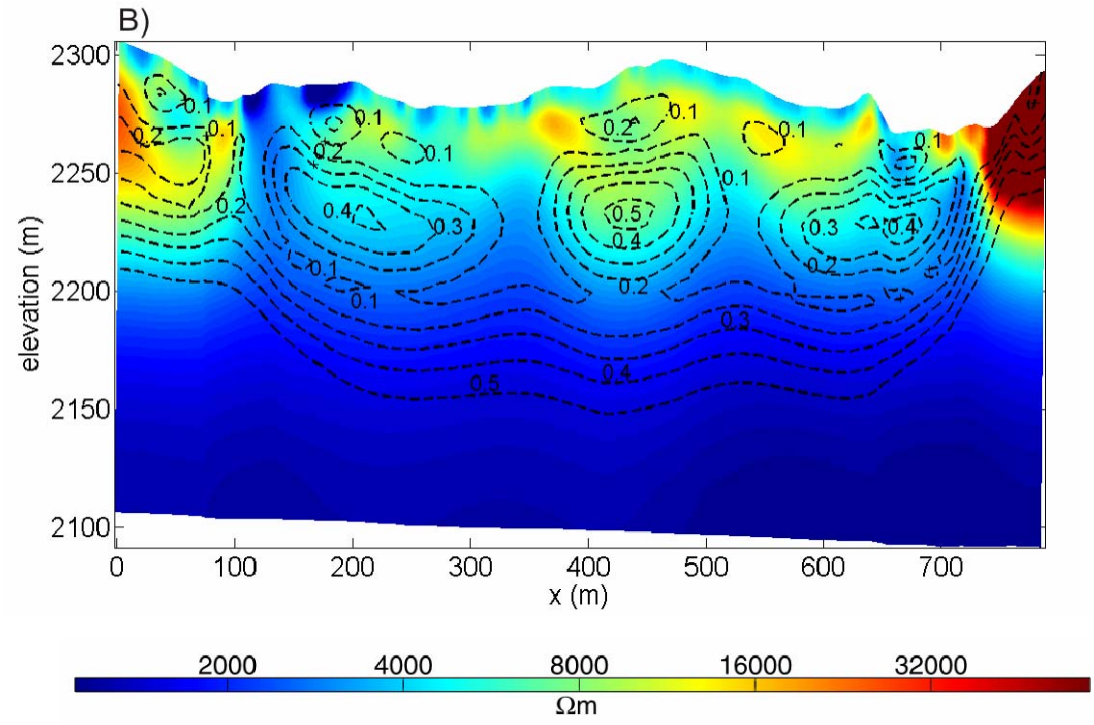
B)
elevation (m)
2300
2250
2200
2150
2100
0
100
200
300
400
500
600
700
x (m)
2000
4000
8000
16000
32000
Ωm

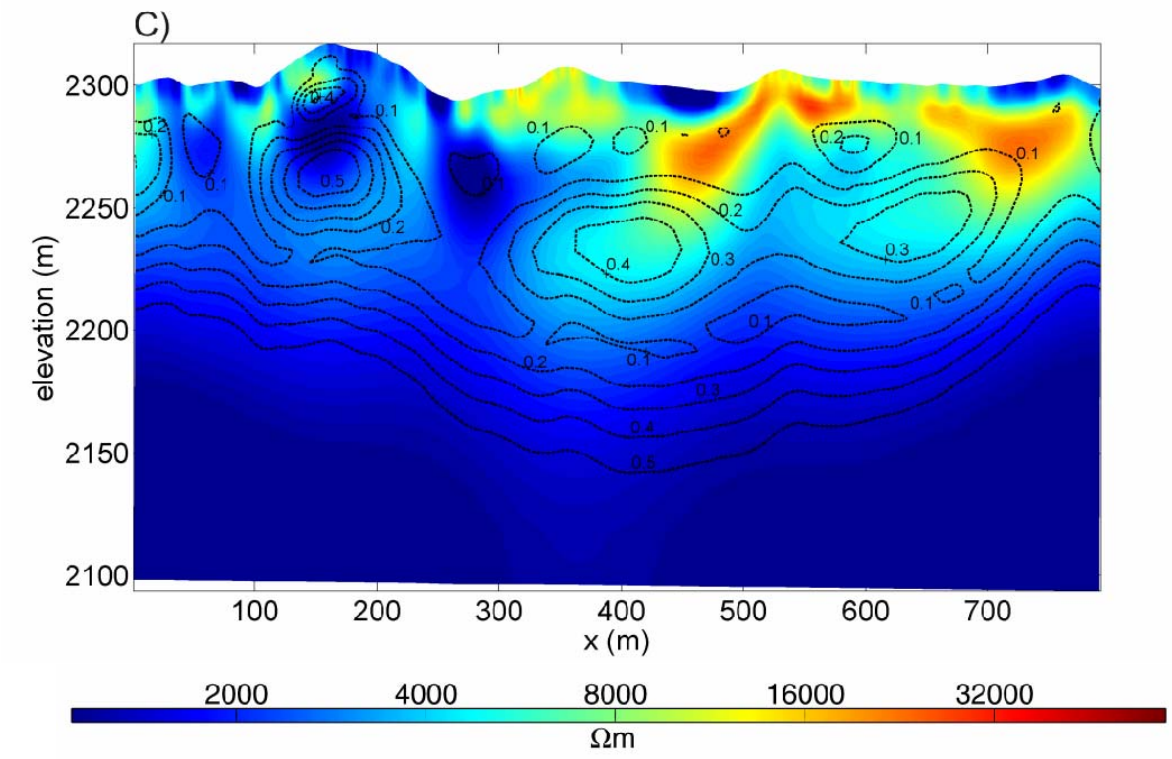
C)
elevation (m)
2300
2250
2200
2150
2100
100
200
300
400
500
600
700
x (m)
2000
4000
8000
16000
32000
Ωm

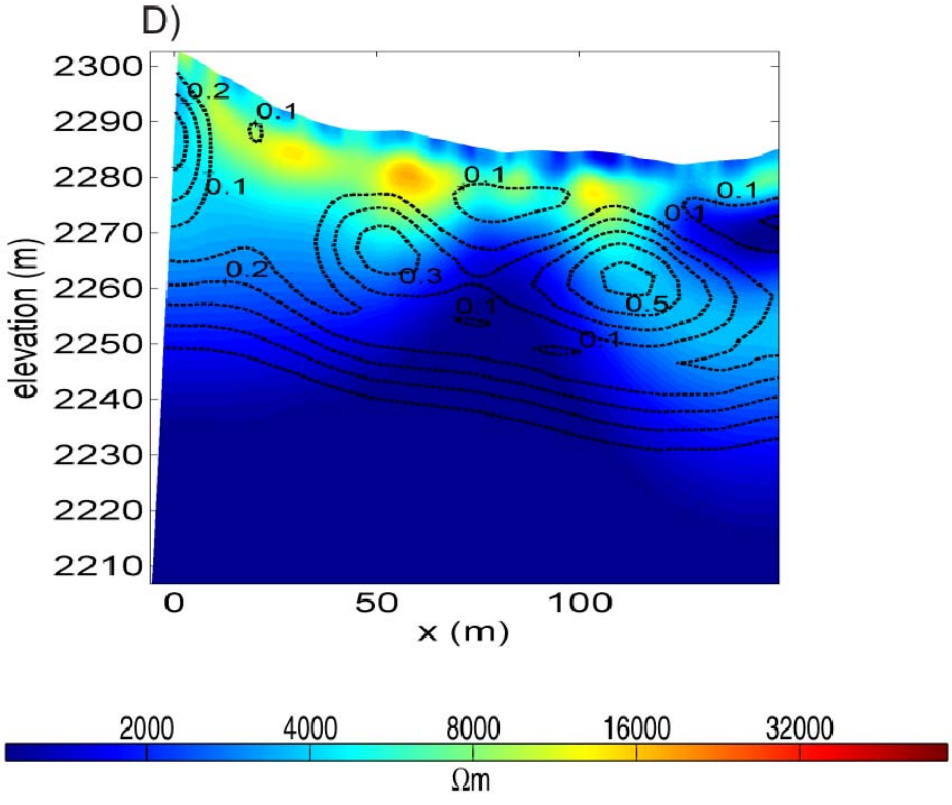
D)
elevation (m)
2300
2290
2280
2270
2260
2250
2240
2230
2220
2210
0
50
100
x (m)
2000
4000
8000
16000
32000
Ωm

Figure A-1) Resistivity models showing the depth of investigation contour intervals for ERI lines 1(A), 2(B), 3(C) and 4(D). Note that individual model blocks are not show here in order to highlight the DOI contours. Also, note that there are slight differences between the inversions presented here and those in Chapter 2. This is the result of having to use slightly different inversion parameters as mentioned in the text of the appendix.

APPENDIX B: : FORWARD MODELLING OF HYPOTHETICAL MORAINE SUBSURFACE RESISTIVITY STRUCTURE

Chapter 2 presented the hypothesis that a low-resistivity layer of saturated sediments and/or saturated fractured bedrock exists above the competent bedrock layer, masking the competent bedrock's high resistivity. To test whether this hypothesis was plausible, I used forward modelling. First, hypothetical subsurface resistivity-distributions of varying complexity were specified to simulate the resistivity structure of the moraine as interpreted from the ERI line 2 survey results. Synthetic resistivity data sets were then generated using an electrical resistivity forward modelling algorithm [open source code FW_2_5D; *Pidlisecky and Knight*, 2008] to calculate the apparent resistivity that would be measured by a survey over the hypothetical subsurfaces. Note that both the topography of the hypothetical resistivity distributions and the survey geometry (electrode location and measurement sequence) specified in the forward modelling algorithm were identical to the actual topography and survey geometry for ERI line 2.

Three hypothetical subsurface resistivity distributions are compared with the inversion models of the corresponding synthetic data sets generated by the forward modelling algorithm (Figures B-1 to B-3). These results clearly show that even a relatively thin conductive layer can mask a thick, highly resistive layer (e.g. bedrock). Thus, the hypothesis that in the resistivity models a relatively thin layer of saturated sediments and/or fractured bedrock is masking the competent bedrock layer is reasonable.

References

Pidlisecky, A., and R. Knight (2008), FW2_5D: A MATLAB 2.5-D electrical resistivity modeling code, *Computers & Geosciences*, *34*(12), 1645-1654.

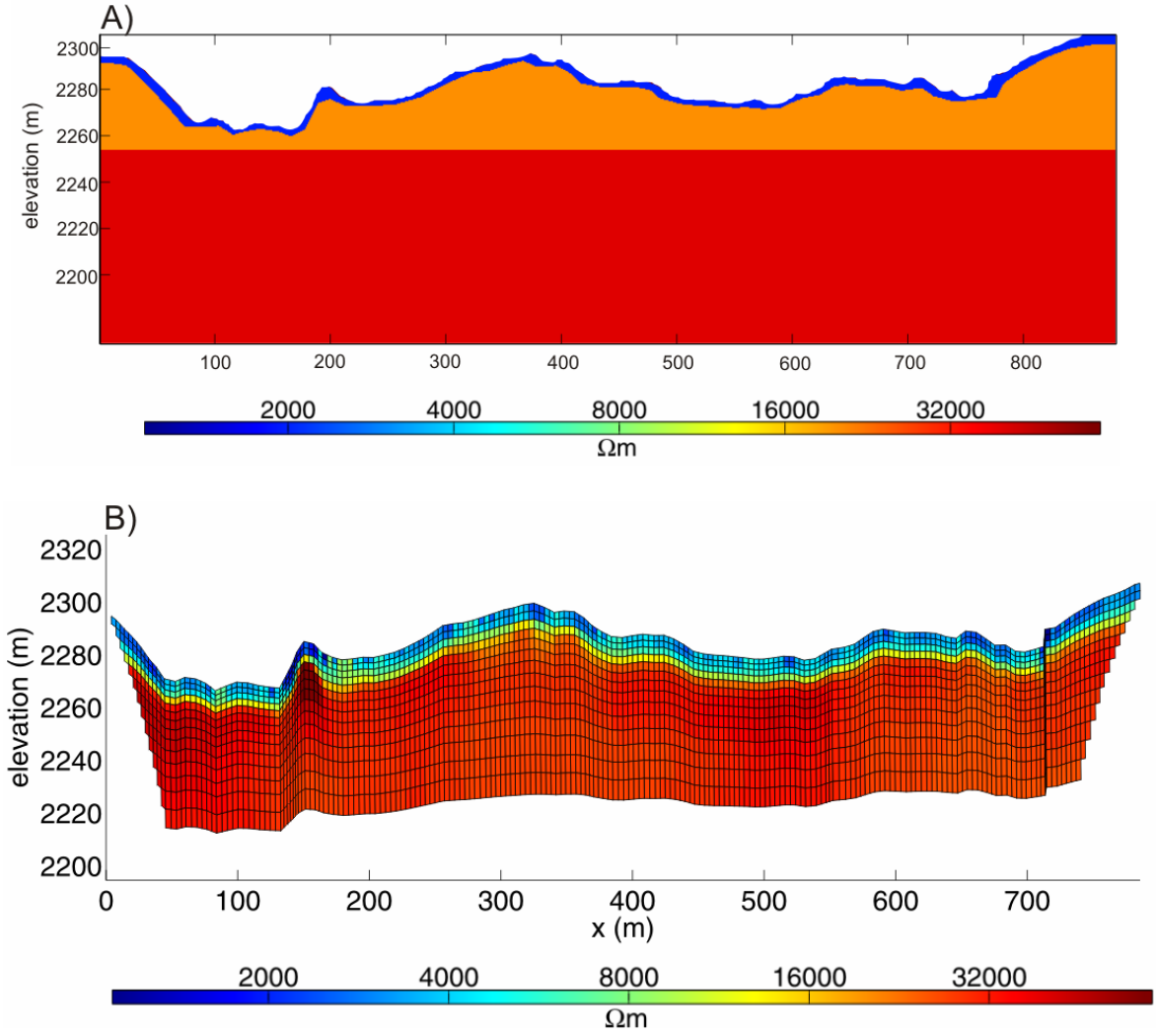

Figure B-1 A) Hypothetical subsurface resistivity distribution for ERI line 2. A resistive moraine layer (20 000 Ωm) is specified overlying the competent bedrock layer (40 000) at an elevation of ca. 2255 m. B) The inversion of the synthetic data set generating using a electrical resistivity forward modelling algorithm. Note that the competent bedrock and the lower resistivity moraine layer are not clearly distinguishable.

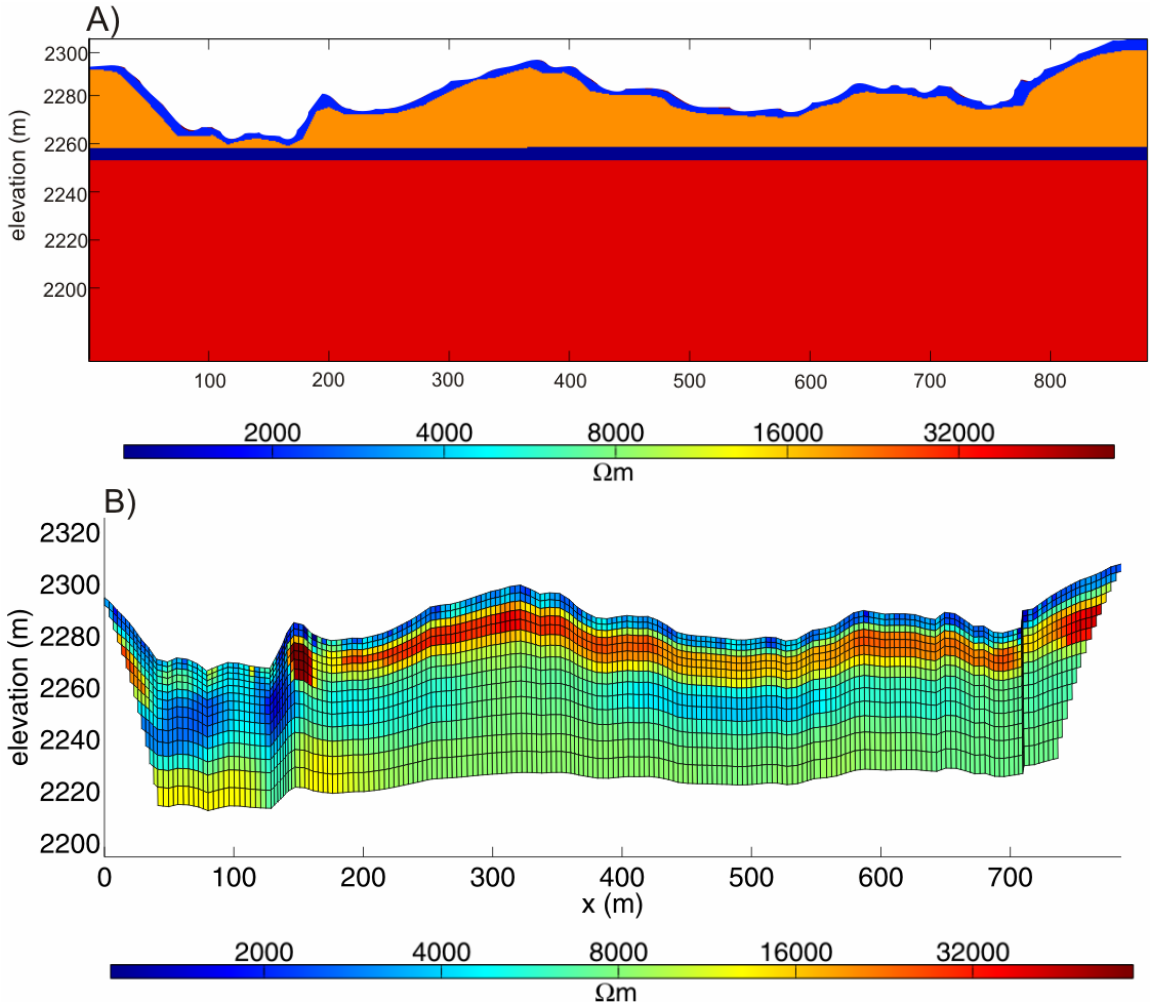

Figure B-2. A) Hypothetical subsurface resistivity distribution for ERI line 2. A ca. 5 m thick low resistivity layer (5000 Ωm) is specified overlying the competent bedrock layer (40 000 Ωm) at and elevation of ca. 2255 m. B) The inversion of the synthetic data set generating using a electrical resistivity forward modelling algorithm. Note that the competent bedrock is not imaged by the inversion.

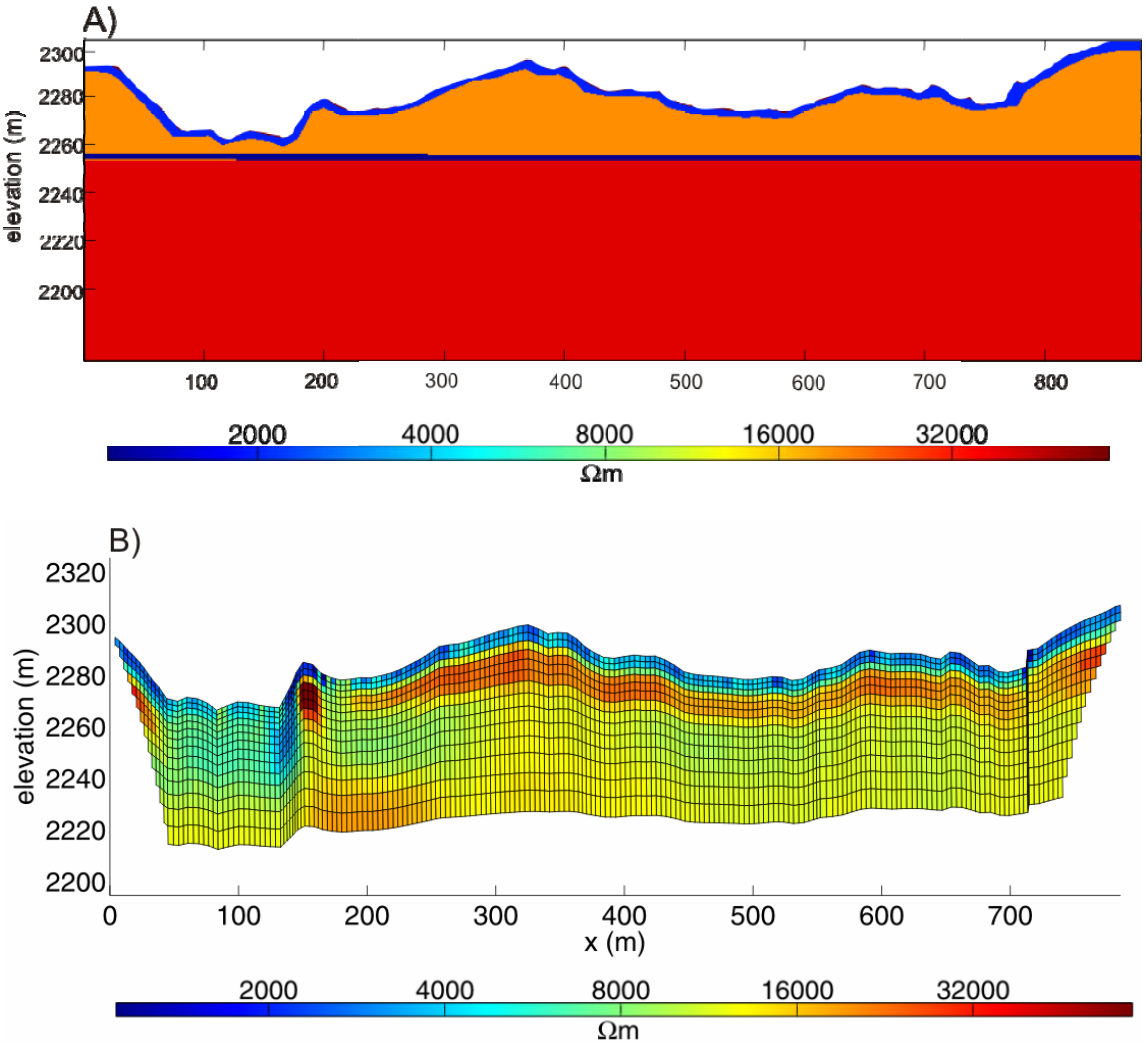

Figure B-3. A) Hypothetical subsurface resistivity distribution for ERI line 2. A ca. 3 m thick low resistivity layer (5000 Ωm) is specified overlying the competent bedrock layer (40 000 Ωm) at and elevation of ca. 2255 m. B) The inversion of the synthetic data set generating using a electrical resistivity forward modelling algorithm. Note that the competent bedrock is not imaged by the inversion however resistivities below 2255 m are higher than for Figure B-2B.

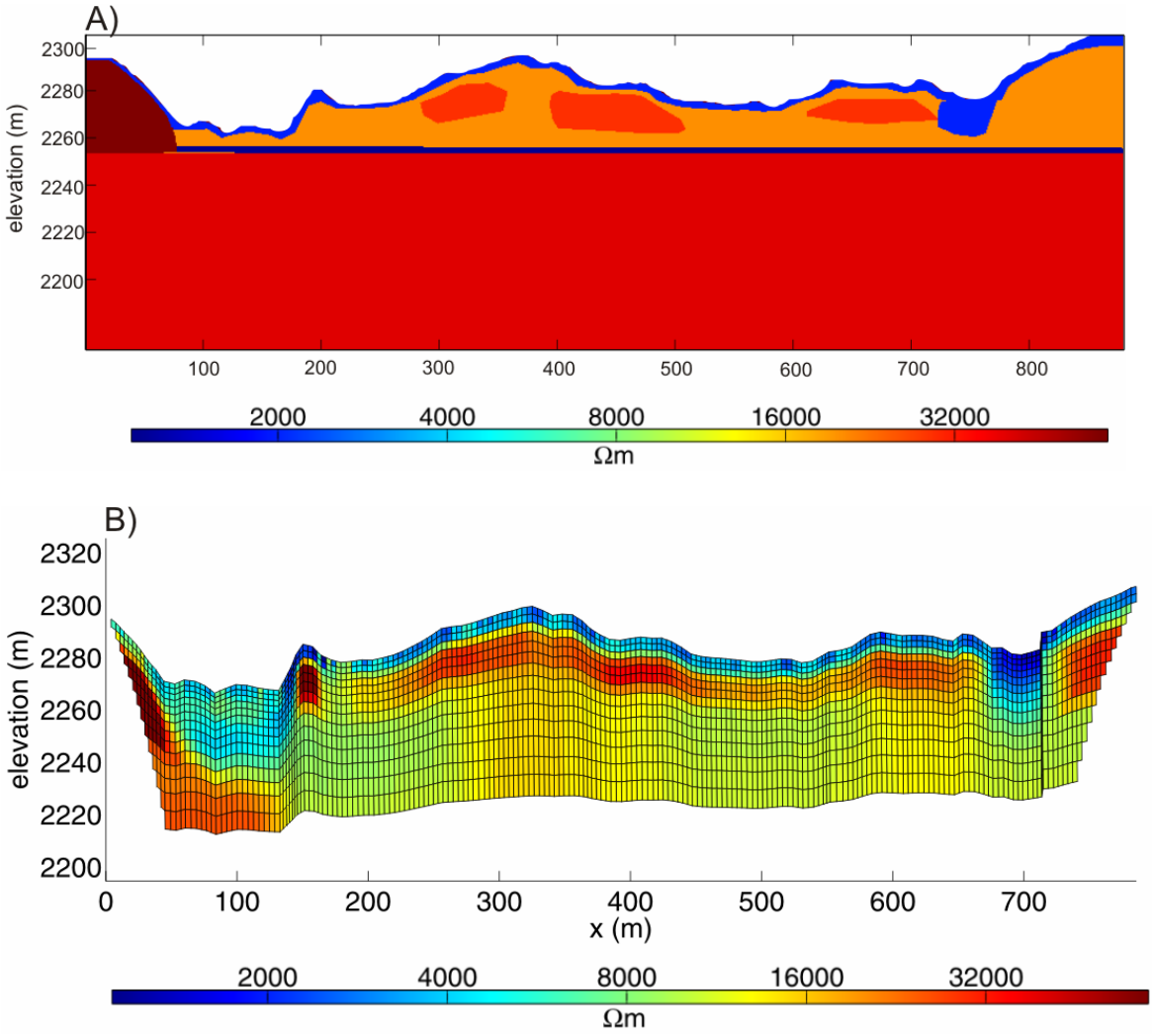

Figure B-4 A) Hypothetical subsurface resistivity distribution for ERI line 2. A ca. 5 m thick low resistivity layer (5000 Ωm) layer is specified overlying the competent bedrock layer with a specified resistivity of 40 000 Ωm at and elevation of ca. 2255 m. A number of structures ranging in resistivity from 30 000 to 200 000 Ωm are specified in the model to simulated degrading permafrost and massive ice. B) The inversion of the synthetic data set generating using a electrical resistivity forward modelling algorithm. Note that the competent bedrock is not imaged by the inversion.

APPENDIX C: A PRELIMINARY ESTIMATION OF THE VOLUME OF BURIED ICE AND ITS HYDROLOGICAL SIGNIFICANCE

Buried ice and permafrost likely play an important role in groundwater storage and shallow subsurface flow within the Opabin Moraine. Although rock glaciers in the Andes have been shown to represent an important source of stored water [*Schrott*, 1996], little work has been conducted to quantify this resource for the Canadian Rockies. This appendix provides a preliminary estimate of the volume of water stored as buried massive ice and the potential contributions of buried-ice melt to the watershed's water balance. The anlyses presented here are base on crude estimates and are meant only to serve as an impetus for further study.

Temperature sensors distributed across the moraine to record the temperature at the snow-moraine interface (as per BTS method described in Chapter 2) were used in addition to the geophysical data presented in chapter 2 to delineate the location of ice and permafrost (Figure C1). To estimate the volume of water stored as buried ice within the moraine, the surface area of the regions interpreted to be buried massive ice (Figure C1) were first estimated from the digital elevation model (DEM) of the moraine using ArcGIS (ESRI). A range of buried ice volumes were then calculated for estimated ice thicknesses of 10, 20 and 30 m, and for ice contents of 50, 60 and 70% (Table 1). Ice contents were based on the range of ice contents for rock glaciers in the Andes and Alps presented by Schrott [1996] and Hausmann et. al. [2007] respectively. Although it is possible that the ice content of rock glaciers differs from the buried-ice content of the Opabin moraine, these values likely represent a reasonable first estimate. The water

equivalent of the buried ice was also calculated using a density of 0.85 g/cm^3 [*Paterson*, 1999] For comparison, the ice volume and water equivalent of the Opabin glacier was estimated using the same method, but for ice contents of 80 and 85% as ice glaciers are expected to contain less debris than rock glaciers (Table 2). According to these estimates, the volume of water stored as buried ice within the Opabin moraine is similar in magnitude to the volume of water stored in the Opabin glacier. Consequently, ice buried within course deposits should be recognized as important stores and sources of water in alpine watersheds, just as glaciers are currently. This may be especially true in the context of climate changes as buried ice will likely melt much more slowly than glaciers and so may play an increasingly important role in late season stream discharge as the glaciers disappear.

Although Østrem [1959] suggests that sufficient debris cover greatly decreases melt rates, few studies have attempted to quantify these rates. Gardner et al. [1991] found that the ablation rate of exposed ice in a valley-side ice-cored moraine in the Canadian Rockies was 7.4 cmd^{-1} over a 20 d period, but the ablation rate of deeply buried ice was not assessed. A study of wastage of the Klutlan ice-cored moraines in Canada's Yukon territory calculated ablation rates to be 0.2 ma^{-1} [*Driscoll*, 1980; 1984], whereas a study of an Antarctic rock glacier found ablation rates to be considerably less [0.05 ma-1; *Pickard*, 1984].

Since much of the Opabin moraine ice-core is well buried, it is likely that the melt rates of the ice-cored regions of the Opabin moraine are more similar to those of the Klutlan ice-cored moraines in Canada's Yukon territory noted by Driscoll [1980; 1984], than the exposed ice melt rates presented by Gardner [1991]. Therefore, the melt rates

presented by Driscoll and the surface area of the regions Opabin Moraine interpreted to be buried massive ice (as determined above) were used to calculate a first approximation of the annual contribution of buried ice melt to the outflow of the watershed. This analysis indicates that melting buried ice would release approximately 70 000 m^3a^{-1} of water from storage. This represents <1% of the annual discharge of the watershed. Comparatively, the Opabin glacier contributes approximately 3% to total watershed discharge (Hood J.L., pers. comm.). Although the contribution of buried ice-melt is apparently minimal, more rigorous scientific study is required to confirm these estimates and to determine whether this source of discharge has any hydrological, biogeochemical and/or eco-hydrological significance.

References

Driscoll, F. G. (1980), Wastage of the Klutlan ice-cored moraines, Yukon Territory, Canada, *Quarernary Research*, *14*, 19.

Driscoll, F. G. (1984), Reply to Comments by John Pickard Regarding "Wastage of the Klutlan Ice-Cored Moraines, Yukon Territory, Canada", *Quarernary Research*, *22*, 260-261.

Gardner, L. E. M. a. J. S. (1991), Mass Wasting on Valley-Side Ice-Cored Moraines, Boundary Glacier, Alberta, Canada, *Geografiska Annaler*, *73*(3/4), 6.

Hausmann, H., et al. (2007), Internal structure and ice content of reichenkar rock glacier (Stubai alps, Austria) assessed by geophysical investigations, *Permafrost and Periglacial Processes*, *18*(4), 351-367.

Østrem, G. (1959), Ice melting under a thin layer of moraine, and the existence of ice cover in moriane covers in moraine ridges, *Geografiska Annaler*, *41*, 228-230.

Paterson, W. S. B. (1999), *The Physics of Glaciers*, Third ed., Butterworth-Heinemann, Oxford.

Pickard, J. (1984), Comment on "Wastage of the Klutlan Ice-Cored Moraines, Yukon Territory, Canada" by Driscoll (1980), *Quaternary Research*, *22*, 1.

Schrott, L. (1996), Some geomorphological-hydrological aspects of rock glaciers in the Andes (San Juan, Argentina), *Zeitschrift fur Geomorphologie*, *Supplementband 104*, 13.

Ice Thickness (m)	Ice Volume for 50% Ice Content (m^3)	Water Equivalent (m^3)	Ice Volume for 60% Ice Content (m^3)	Water Equivalent (m^3)	Ice Volume for 70%Ice Content (m^3)	Water Equivalent (m^3)
10	3470000	1735000	2082000	1769700	2429000	2064650
15	5205000	2602500	3123000	2654550	3643500	3096975
20	6940000	3470000	4165000	3539400	3858000	4129300

Table C-1. Estimated water volumes stored as buried ice for ice thickness estimates of 10, 15 and 20 m.

Ice Thickness (m)	Ice Volume for 80% Ice Content (m^3)	Water Equivalent (m^3)	Ice Volume for 85% Ice Content (m^3)	Water Equivalent (m^3)
20	2644800	2248080	2810100	2388585
30	3967200	3372120	4215150	3582878
40	5289600	4496160	5620200	4777170

Table C-2. Estimated water volumes stored as glacier ice for ice thickness estimates of 20, 30 and 40 m.

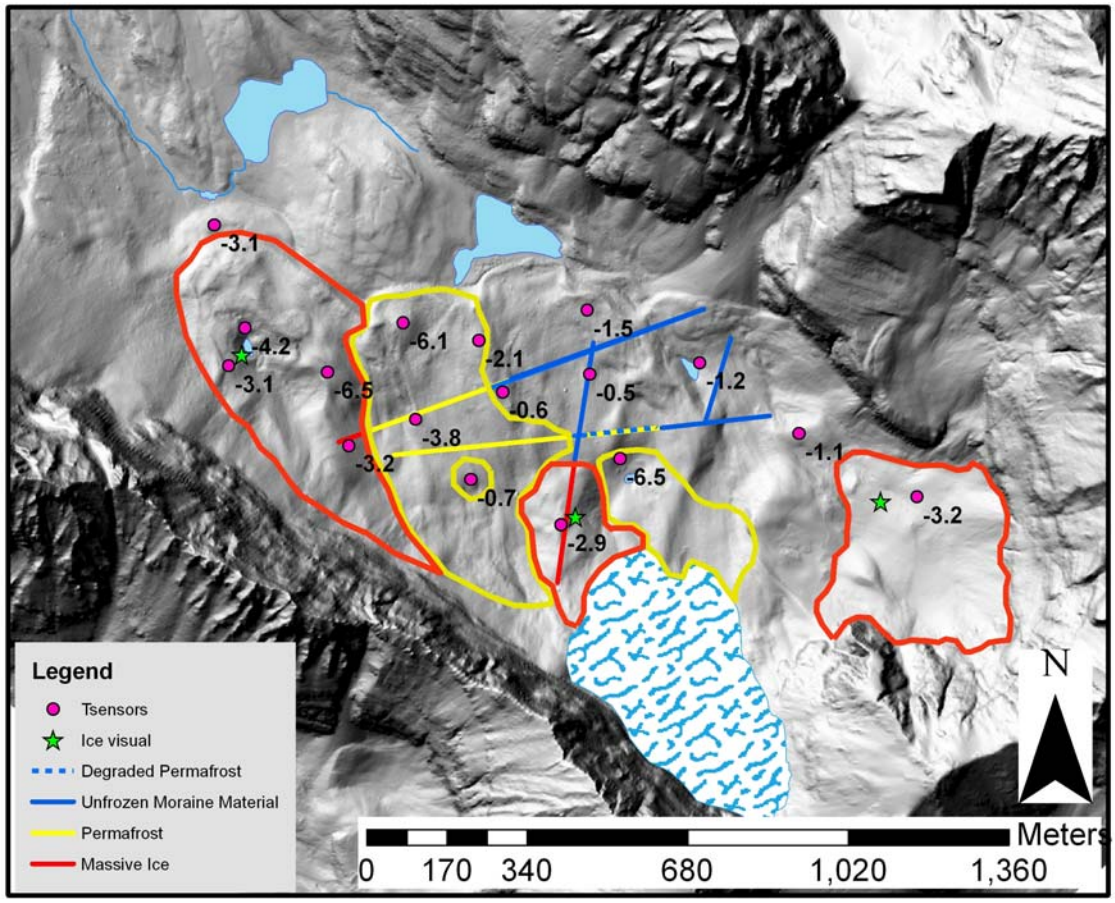

Figure C-1. Temperature sensors distributed across the moraine and the geophysical results discussed in Chapter 2 are used to delineate regions of the moraine thought to be cored by massive ice and permafrost. Average temperatues at the snow-moraine interface below -2 oC, are interpreted to indicate permafrost or buried massive ice (see Chapter 2 methods). Temperatues presented (oC) are the average of temperatures recorded ever 10 min from Jan. 1 to April 1, 2008. Regions of the moraine hypothesized to be cored with massive ice are outlined in red, while regions hypothesized to contain permafrost are outlined in yellow. Regions of the moraine not outlined are interpreted to be ice and permafrost free.